**Title**
Doppler Velocimetry of Current Driven Spin Helices in a Two-Dimensional Electron Gas



**Author**
Yang, Luyi

**Publication Date**
2013

Peer reviewed|Thesis/dissertation

**Doppler Velocimetry of Current Driven Spin Helices in a Two-Dimensional Electron Gas**

by

Luyi Yang

A dissertation submitted in partial satisfaction of the
requirements for the degree of
Doctor of Philosophy

in

Physics

in the

Graduate Division

of the

University of California, Berkeley

Committee in charge:

Professor Joseph Orenstein, Chair
Professor Dung-hai Lee
Professor Oscar Dubon

Spring 2013

**Doppler Velocimetry of Current Driven Spin Helices in a Two-Dimensional Electron Gas**

## Abstract

Doppler Velocimetry of Current Driven Spin Helices in a Two-Dimensional Electron Gas

by

Luyi Yang

Doctor of Philosophy in Physics

University of California, Berkeley

Professor Joseph Orenstein, Chair

Spins in semiconductors provide a pathway towards the development of spin-based electronics. The appeal of spin logic devices lies in the fact that the spin current is even under time reversal symmetry, yielding non-dissipative coupling to the electric field. To exploit the energy-saving potential of spin current it is essential to be able to control it. While recent demonstrations of electrical-gate control in spin-transistor configurations show great promise, operation at room temperature remains elusive. Further progress requires a deeper understanding of the propagation of spin polarization, particularly in the high mobility semiconductors used for devices.

This thesis presents the demonstration and application of a powerful new optical technique, Doppler spin velocimetry, for probing the motion of spin polarization at the level of 1 nm on a picosecond time scale. We discuss experiments in which this technique is used to measure the motion of spin helices in high mobility $n$-GaAs quantum wells as a function of temperature, in-plane electric field, and photoinduced spin polarization amplitude. We find that the spin helix velocity changes sign as a function of wave vector and is zero at the wave vector that yields the largest spin lifetime. This observation is quite striking, but can be explained by the random walk model that we have developed. We discover that coherent spin precession within a propagating spin density wave is lost at temperatures near 150 K. This finding is critical to understanding why room temperature operation of devices based on electrical gate control of spin current has so far remained elusive. We report that, at all temperatures, electron spin polarization co-propagates with the high-mobility electron sea, even when this requires an unusual form of separation of spin density from photoinjected electron density. Furthermore, although the spin packet co-propagates with the two-dimensional electron gas, spin diffusion is strongly suppressed by electron-electron interactions, leading to remarkable resistance to diffusive spreading of the drifting pulse of spin polarization. Finally, we show that spin helices continue propagate at the same speed as the Fermi sea even when the electron drift velocity exceeds the Fermi velocity of $10^7$ cm s$^{-1}$.

We also use this phase-resolved Doppler velocimetry technique to perform the first simultaneous measurements of drift and diffusion of electron-hole packets in the same two-

dimensional electron gas. The results that we obtain strongly violate the picture of electron-hole transport that is presented in the classic textbook treatments of ambipolar dynamics. We find that the rates of transport are controlled almost entirely by the intrinsic frictional force exerted between electrons and holes, rather than the interaction of carriers with phonons or impurities. From the experimental data we obtain the first measurement of the "Coulomb drag" friction between electrons and holes coexisting in the same two-dimensional layer. Moreover, we show that the frictional force thus obtained is in quantitative agreement with theoretically predicted values, which follow entirely from electron density, temperature and fundamental constants, i.e. no adjustable parameters. The understanding of ambipolar transport that we have achieved is an essential prerequisite to the design of those spintronic devices in which spin current is carried by the drift of polarized electrons and holes.

To my parents and Wenbin.

# Contents

# List of Abbreviations

| | |
|---|---|
| 2DEG | Two-Dimensional Electron Gas |
| CINT | Center for Integration and Nanotechnologies |
| CISP | Current-Induced Spin Polarization |
| DI | Deionized |
| DP | D'yakonov-Perel' |
| EBASE | Epoxy Bond And Stop-Etch |
| *e-e* | electron-electron |
| *e-h* | electron-hole |
| HF | Hydrofluoric |
| HH | Heavy-Hole |
| KB | Kleinert and Bryksin |
| LH | Light-Hole |
| LO | Local Oscillator |
| MBE | Molecular Beam Epitaxy |
| PSH | Persistent Spin Helix |
| PPE | Personal Protective Equipments |
| QW | Quantum Well |
| RPA | Random Phase Approximation |
| RTA | Rapid Thermal Annealing |
| RW | Random Walk |
| SCD | Spin Coulomb Drag |
| SDW | Spin Density Wave |
| SO | Spin-Orbit |
| SOC | Spin-Orbit Coupling |
| TGS | Transient Grating Spectroscopy |
| UV | Ultraviolet |

# Acknowledgments

First and foremost, it is with immense gratitude and respect that I acknowledge the support and help of my advisor Prof. Joseph Orenstein. It has been an edifying experience which I cherish forever to work with Joe, who is a great experimentalist with deep physical insights and has written many impressive theory papers. He is strongly dedicated to the research projects and spends many hours with us almost everyday. My doctoral endeavor would not have been possible without his constant help and guidance. I treasure the time with him discussing physics and deriving formulas on the board, as well as troubleshooting technical problems in the lab. Even in my dreams, I have been auguring the data with him many times. I am very lucky to have such an inspiring and creative advisor, who has made my Ph.D. very fruitful.

It gives me great pleasure in acknowledging Dr. Jake Koralek, from whom I learnt numerous experimental skills. I appreciate all the time and effort that he has put into tutoring me. I would also like to place on record my deep appreciation for the valuable co-operation and enormous goodwill shown by my other colleagues Daniel Golubchik, Matt Langner, Colleen Kantner, James Hinton, Chris Weber, etc. I have enjoyed every bit of my interaction with them.

I am highly indebted to Dr. Michael Lilly at Center for Integration and Nanotechnologies (CINT). Throughout my Ph.D., I have been to Sandia Laboratories in Albuquerque four times and learnt a lot of sample design, microfabrication and transport techniques from Mike. He is a very nice person to work with. I thank the friendly and helpful people at CINT: Denise Tibbetts, John Reno, Catherine Mombourquette, John Nogan, Nathan Bishop and Dominique Laroche.

I consider it an honor to work with Prof. Dung-hai Lee, a luminary among the condensed matter theorists. I wish to express my gratitude and appreciation to Prof. Giovanni Vignale, interaction with whom has been academically highly rewarding and personally very delightful. I also thank Prof. David Goldhaber-Gordon and Adam Sciambi for useful discussions. I am beholden to Prof. Bang-fen Zhu, Prof. Feng Wang, Prof. Oscar Dubon, Prof. Frances Hellman, Prof. Irfan Siddiqi, Prof. James Analytis, and Prof. Y. Ron Shen for their guidance, patience and encouragement. I am obliged to all my teachers at Berkeley: Prof. Robert Littlejohn, Prof. Steven Louie, Prof. Joel Moore, Prof. Ashvin Vishwanath, etc., whose pedagogical excellence ensured that I grasped the grammar of physics.

I appreciate deeply all the help rendered by the student office staff Anne Takizawa, who is very approachable and knows every student very well. It is always a pleasure stopping by her office and chatting with her.

I wish to say a heartfelt thank you to my friends at Berkeley and from high school and college for being there for me. My interaction with them has always been very pleasant. I fondly mention the names of Shuyun, Pu, Xiaowei, Lingkai, Chenggang, Ellen, Yimin, Anlie, Ai, Liwen, Mengjie, Yiming, Yike, Shaola, Na, and Zhe.

I am sincerely grateful for my Italian instructor Mara, Portuguese instructor Catarina, and Cal Volleyball Team for making my life outside the lab more enjoyable.

I am thankful to University of California at Berkeley, Lawrence Berkeley National Laboratory and Sandia National Laboratories for providing all facilities for research, congenial ambience and exciting environment.

Throughout my stay at Cal, I have enjoyed the emotional support provided by my parents back home in China and my boyfriend Wenbin, who was a graduate student at Stony Brook and now a postdoc at Caltech. I would not have made it this far without their full-hearted support.

Last but not least, as a die-hard fan of volleyball for 20 years, I would love to thank my favorite volleyball teams (China, Brazil, Italy and USA Women's National Teams) and players for their inspiration and kindness.

# Chapter 1

# Introduction

The properties of materials in which the electron's spin is strongly coupled to its motion are receiving increasing attention in a variety of contexts. From an applications point of view, spin-orbit coupling (SOC) provides a mechanism by which spin polarization lifetime and mobility can be controlled by applied electric fields. From a basic science perspective, SOC introduces many of the phenomena usually associated with time-reversal breaking, such as spin precession [1], nonuniversal [2, 3], and quantum Hall effects [4, 5], without the need for large externally applied magnetic fields.

Spin-orbit (SO) coupled two-dimensional electron systems are of great interest, both as model systems and as the active component of devices that control electron spin with electric fields [6]. Unfortunately, the potential of the SO interaction to control electron spin comes with a price - the SO terms in the Hamiltonian break SU(2) spin symmetry. The violation of SU(2) means that electron spin polarization is not conserved, decaying instead with a characteristic spin memory time $\tau_s$. The mechanism by which SO coupling leads to spin memory loss has been intensively investigated in two-dimensional electron gases (2DEGs) in semiconductor quantum wells (QWs), as described in recent reviews [7, 8]. In GaAs QWs and related systems, breaking of inversion symmetry allows SO coupling that is linear in the electron wave vector $\boldsymbol{k}$ [1, 9, 10]. The SO terms in the Hamiltonian can be viewed as effective magnetic fields that act only on the electron spin, with magnitude and direction that vary with $\boldsymbol{k}$. The loss of spin memory in the effective magnetic field, $\boldsymbol{b}(\boldsymbol{k})$, takes place through the D'yakonov-Perel' (DP) mechanism [11–14]. In this process the electron spin precesses during its ballistic motion between collisions; each time it is scattered $\boldsymbol{b}(\boldsymbol{k})$ and consequently the precession vector, $\boldsymbol{\Omega}(\boldsymbol{k})$, change. The net result is exponential decay of spin polarization at a rate approximately equal to $\Omega^2\tau$, where $\tau$ is the mean time between collisions.

There exist two distinct contributions to $\boldsymbol{b}(\boldsymbol{k})$, the Rashba term [1, 10] arising from asymmetry of the confining potential and the Dresselhaus term [15] originating in the intrinsic inversion asymmetry of the GaAs crystal structure. A prescription for lengthening spin lifetime in QWs of III-V semiconductors by tuning the Rashba coupling strength ($\alpha$) to equal the linear Dresselhaus coupling ($\beta_1$) was proposed by Schliemann *et al.* [16]. Recently it was recognized that this mechanism amounts to a restoration of SU(2) symmetry even in

the presence of anisotropic SO interactions [17].

The potential to extend the spin propagation length despite DP spin memory decay is based on the strong correlation between the electron's displacement in space and the rotation of its spin on the Bloch sphere. An important step toward a quantitative theory of such correlations was made by Burkov *et al.* [18] and Mishchenko *et al.* [19]. who derived equations of motion that describe the coupling of spin and charge current degrees of freedom in (001) GaAs QWs. Initially only the linear Rashba SO coupling was examined, subsequently Bernevig *et al.* [17] and Stanescu and Galitski [20] extended the theory to include the linear and cubic Dresselhaus terms, respectively.

The equations of motion can be solved to obtain the normal modes of the coupled system, which are waves of mixed electrical current and spin polarization. There exist four such modes, reflecting three spin degrees of freedom ($S_x, S_y$, and $S_z$) and the charge density, $n$. For wave vectors, $\boldsymbol{q}$, parallel to the directions [110] and [1$\bar{1}$0], the four modes decouple into two pairs; in one the spin precesses in a plane containing $\boldsymbol{q}$ and the normal direction $\hat{\boldsymbol{z}}$, in the other the current is coupled to the component of in-plane spin polarization perpendicular to $\boldsymbol{q}$.

The spin precession mode is the one relevant to spin polarization memory. For example, the decay rate of this mode at $\boldsymbol{q} = 0$ is precisely the DP decay rate, $1/\tau_s$. In the absence of spin-space correlation, the decay rate, $\gamma_q$, of a spin polarization wave would increase monotonically with $q$, *i.e.*, $\gamma_q = 1/\tau_s + D_s q^2$, where $D_s$ is the spin diffusion coefficient. Instead, it was predicted [18] that for Rashba SO coupling the minimum decay rate occurs at nonzero wave vector, at which point $\gamma_q$ is approximately half the DP rate. Bernevig *et al.* [17] showed theoretically that the minimum $\gamma_q$ is further reduced when both Rashba and linear Dresselhaus interactions are nonzero and vanishes when the strength of the two couplings is equal. The resulting "persistent spin helix" (PSH) was shown to be a conserved quantity of a newly found SU(2) symmetry that arises when $\alpha = \beta_1$ and the cubic Dresselhaus term ($\beta_3$) is zero [17]. However, Stanescu and Galitski [20] showed that perfect SU(2) is broken when $\beta_3 \neq 0$, leading to large, but not infinite, PSH lifetime. Spin helices with strongly enhanced lifetimes have been observed by transient grating spectroscopy [21] and subsequently imaged by Kerr microscopy [22].

The question that arises is whether the PSH effect can be exploited to lengthen the distance that a packet of spin polarization can propagate in an applied electric field. In this paper we address this question both theoretically and experimentally by studying the effects of an in-plane electric ($E$) field on the spin-precession modes. We focus on $\boldsymbol{E} \parallel \boldsymbol{q}$, which is the orientation relevant to the drift of spin polarization.

Theoretically, we derive and solve equations of motion to quadratic order in $E$ using a random walk (RW) approach that is different from previous treatments of this problem [23]. The advantages of our approach are physical transparency and mathematical simplicity. This model interprets the experimental measurements of spin helix dynamics under the influence of applied electric fields very well.

Experimentally, we present direct observation of the translational motion of spin helices in high mobility $n$-GaAs quantum wells under the influence of applied electric fields. The

spin lifetimes in high mobility systems are about $10-100$ ps, during which spin may only propagate $10-100$ nm. To resolve spin propagation on picosecond timescales and nanometer length scales, we report the development of an optical technique to measure velocity through the Doppler shift of light scattered from propagating waves of spin density [24, 25]. This technique has also enabled us to fully characterize the coupled motion of the electron-hole ($e$-$h$) packets [26].

GaAs quantum wells are ideal model systems in which to detect coherently propagating spin helices, for several reasons. First, the optical orientation effect in III-V semiconductors enables photoexcitation of nonequilibrium waves of spin density by interfering two orthogonally polarized beams at the sample surface - yielding a so-called transient spin grating [27]. Second, the strength of the SO coupling in GaAs is such that the micron-scale pitch of helices with enhanced lifetime is well matched to the wavelength of the 1.5 eV photons that are needed to generate the nonequilibrium spin density. As a result of this matching, the amplitude of the spin polarization can be measured by diffracting a probe beam from the transient grating. We use optical heterodyne detection to measure the phase as well as the amplitude of the diffracted probe [28–30], as the former is sensitive to the translational motion of the spin helix [24]. Finally, the combination of low carrier density and high mobility below 70 K enable the generation of large drift velocities with minimal Joule heating.

The measurements reported in this thesis were performed on a 9 nm wide n-doped GaAs/AlGaAs quantum well, grown by molecular beam epitaxy (MBE) on a semi-insulating GaAs (001) substrate (VB0355). The carrier density and mobility of the 2DEG are $1.9\times10^{11}$ cm$^{-2}$ and $5.5\times10^{5}$ cm$^2$V$^{-1}$s$^{-1}$ at 5 K, respectively. The silicon donors were symmetrically doped in the center of each barrier. The Dresselhaus SO coupling dominates and Rashba SO interaction is negligible. The samples were prepared using standard photolithography processes. The 2DEG channel was defined by a mesa etching, and Ohmic contact was made by annealing NiGeAu to the sample. After patterning the top side, the samples were mounted top side down on c-axis cut Sapphire discs, and the GaAs substrate was mechanically lapped and chemically etched to allow for optical measurement in transmission geometry. Several samples were prepared with semitransparent front and back gate electrodes to allow for continuous variation of the equilibrium electron density. Details of the sample structure and preparation can be found in Appendix A.

The rest of the thesis is organized as follows. Chapter 2 is an introduction to the band structure, optical selection rules, SOC, and spin orientation of GaAs QWs and related materials. We also review the new found SU(2) symmetry [17] that motivates the study of the propagation of electron-spin polarization.

In Chapter 3, we introduce and solve a semiclassical RW model that describes the dynamics of spin polarization waves in zinc-blende semiconductor quantum wells [23]. We derive the dispersion relations for these waves, including the Rashba, linear and cubic Dresselhaus spin-orbit interactions, as well as the effects of an electric field applied parallel to the spin polarization wave vector. In agreement with calculations based on quantum kinetic theory [31], the RW approach predicts that spin waves acquire a phase velocity in the presence of the field that crosses zero at a nonzero wave vector, $q_0$, which has been verified experimentally

in the transient spin grating experiments [24].

In Chapter 4, we describe the transient grating spectroscopy and the new experimental technique, Doppler velocimetry, capable of resolving displacements of charge/spin density at the level of 1 nm on a picosecond time scale.

In Chapter 5, we measure the drift and diffusion of electron-hole ($e$-$h$) density waves in an $n$-GaAs QW via the Doppler velocimetry technique [26]. We observe that the motion of $e$-$h$ packets in the high-mobility electron gases violates the predictions of the standard theory, which state that in an $n$-type semiconductor, for example, an $e$-$h$ packet drifts in the direction of the force on the holes, opposite to the motion of the Fermi sea of electrons. Instead, our measurements reveal that the $e$-$h$ packet drifts in the same direction of the Fermi sea of electrons as a result of the momentum exchange between electrons and holes. From the ambipolar diffusion and mobility, we obtain the transresistivity of electrons and holes in the same layer, which is much stronger than is typically seen in the conventional Coulomb drag experiments on coupled quantum wells, but can be understood using the same random-phase approximation (RPA) model that describes coupled wells.

In Chapter 6, we present the application of Doppler velocimetry to resolve the motion of spin-polarized electrons in GaAs quantum wells driven by a drifting Fermi sea [24]. We find that spin diffusion is suppressed as a result of spin-Coulomb drag, while the spin mobility is precisely equal to the electron mobility. This leads to an anomalous rigidity of spin packets, implying an increased distance over which spin information may be transmitted. However, we also observe that the coherent precession of spins driven by spin-orbit interaction, which is essential for the operation of a broad class of spin logic devices, breaks down at temperatures above 150 K, for reasons that are not yet understood theoretically.

In Chapter 7, we discuss experiments in which the same technique is applied to measure the motion of spin helices as a function of the applied in-plane field [25]. At relatively low fields helical modes crossover from overdamped excitations where the spin-precession period exceeds the spin lifetime, to a regime of coherent propagation where several spin-precession periods can be observed. We demonstrate that the envelope of a spin polarization packet reaches a current-driven velocity of $10^7$ cm s$^{-1}$ in an applied field of 70 V cm$^{-1}$.

In the appendices, we discuss the sample processing and the formalism for the $e$-$h$ and spin transresistivity.

# Chapter 2

# Background

## 2.1 Band structure and optical orientation of GaAs

Gallium arsenide crystallizes in what is known as the zinc-blende structure. Figure 2.1a shows the primitive cell of the zinc-blende structure, in which the two face-centered cubic lattices of the diamond structure are occupied by two different atoms, for instance Ga and As, respectively. It does not possess a center of inversion. The point group symmetry is $T_d$ (tetrahedral).

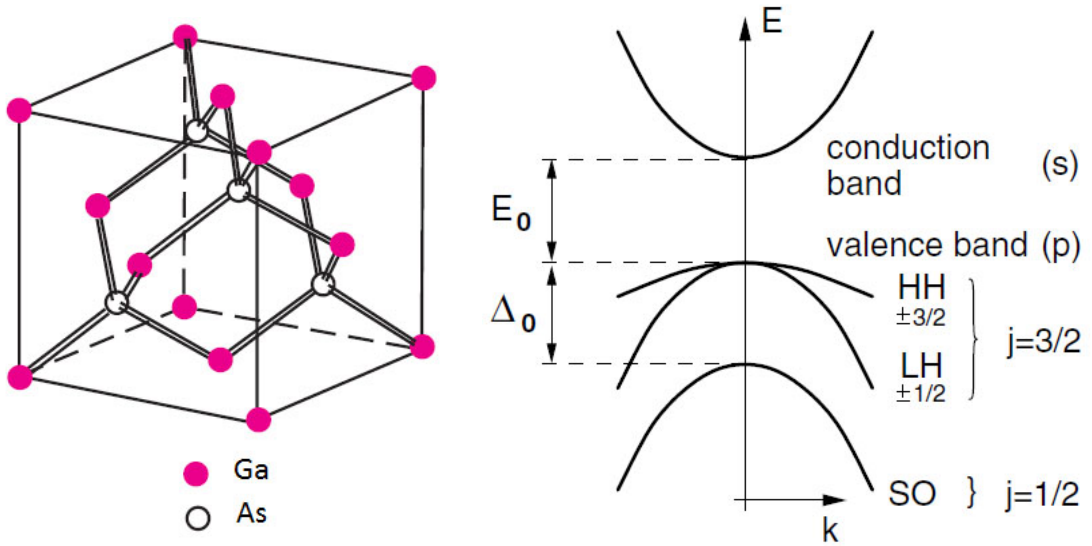


(a) (b)

Figure 2.1: Crystal structure (a) and band dispersion (b) of GaAs. Fig. (b) is taken from Ref. [32].

The important bands of GaAs are shown in Fig. 2.1b. The bottom of the conduction band and the top of the valence band are located at the Γ-point of the Brillouin Zone. The conduction band is $s-$type (orbital angular momentum $l = 0$) belonging to the representation $\Gamma_6$, while the $p-$type valence band is split to a total angular momentum $j = 3/2-$band ($\Gamma_8$) and a $j = 1/2-$band ($\Gamma_7$) known as split-off band by SOC. The $\Gamma_8$ band consists of magnetic quantum number $m_z = \pm 3/2$ heavy-hole (HH) band and $m_z = \pm 1/2$ light-hole (LH) band. The degeneracy of HH and LH at the $\Gamma-$point is lifted in the QW structure due to the quantum confinement. The band gap between the conduction band and the valence band is $E_0 = 1.5$ eV, which is comparable to the most efficient operation wavelength ($\sim 800$ nm) of the Ti:sapphire laser, and the SO splitting $\Delta_0 = 0.34$ eV. Near the Γ-point, the bands can be approximated as

$$E_\nu(\boldsymbol{k}) = \frac{\hbar^2 k^2}{2m_\nu^*}, \tag{2.1}$$

where $m_\nu^*$ is the effective mass and $\nu = c, hh, lh$.

Optical orientation of electrons allows creation of spin-polarized electrons inside direct-gap semiconductors like GaAs [13]. Near-bandgap illumination of a GaAs excites electrons whose initial spin is determined by the helicity of the light due to the fact that left/right circularly polarized photons carry a $z$ component of angular momentum of $-1/+1$. The optical transitions demonstrated in Fig. 2.2 is a consequence of the conservation of angular momentum. A detailed calculation of the dipole transition matrices shows that the probabilities for transitions from the HH and LH states to the conduction band states are in a $3:1$ ratio, as a result the maximum attainable degree of spin polarization is 50%. Confinement in a quantum well lifts the degeneracy of the HH and LH states, with the heavy hole at higher energy, which allows one to selectively photoexcite electrons from the HH band, but not from the LH band, resulting in 100% of spin polarization.

## 2.2 Spin-orbit coupling in GaAs quantum wells

SOC originates from the relativistic effect. If an electron moves with a velocity $\boldsymbol{v}$ in an external electric field $\boldsymbol{E}$, it will see a magnetic field $\boldsymbol{B} = (1/c)\boldsymbol{E} \times \boldsymbol{v}$, where $c$ is the velocity of light. This magnetic field acts on the electron magnetic moment. In vacuum, the SOC can be written as

$$H_{SO} = \lambda_0 \boldsymbol{\sigma} \cdot (\boldsymbol{k} \times \boldsymbol{E}), \tag{2.2}$$

where $m_0$ is vacuum electron mass, $\boldsymbol{\sigma}$ is the Pauli matrix, $\boldsymbol{k} = \boldsymbol{p}/\hbar$, and $\lambda_0 = (\hbar/2m_0c)^2 = 3.7 \times 10^{-6}\text{Å}^2$.

In solids, SOC depends not only on the velocity of the electron, but also on the structure of the Bloch functions defining the motion on the atomic scale. The lack of bulk inversion symmetry leads to the appearance of terms cubic in $k$ in the Hamiltonian for the conduction band, which is known as Dresselhaus SOC [15],

$$H_{D,3d} = \mathfrak{B}\left[\sigma_x k_x(k_y^2 - k_z^2) + \sigma_y k_y(k_z^2 - k_x^2) + \sigma_z k_z(k_x^2 - k_y^2)\right], \tag{2.3}$$

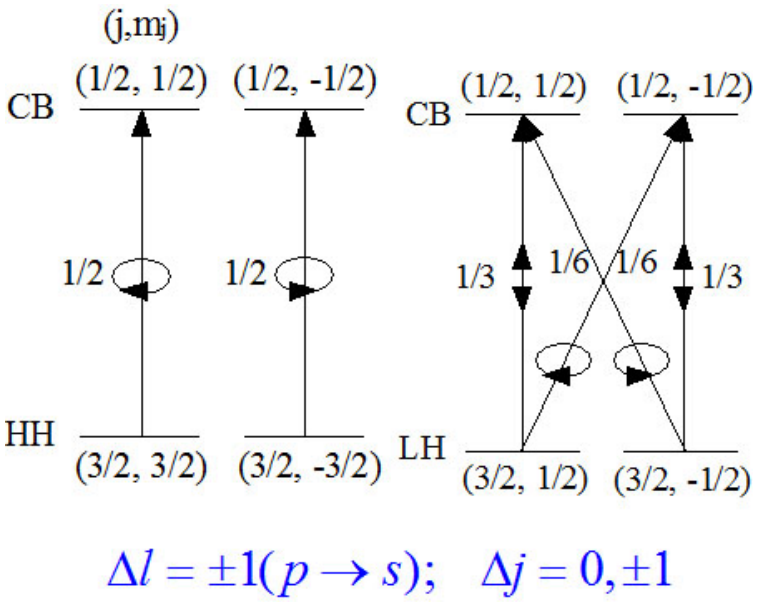


Figure 2.2: Selection rules and relative transition rates for optical transitions between valence band states and conduction band states.

where $k_i$ are along the principle axes, and $\mathfrak{B}$ is the coupling strength, which can be expressed by the band parameters in the $14 \times 14$ Kane model. It varies in a wide range in literatures and was reported to be 5 eV Å$^3$ in our previous studies on a set of QWs with different well widths [21].

When electrons are confined in a QW grown in the [001] direction, $k_z \rightarrow \langle k_z \rangle = 0$ and $k_z^2 \rightarrow \langle k_z^2 \rangle \approx (\pi^2/d^2)$, where $d$ is the width of the QW. The Dresselhaus SO Hamiltonian becomes

$$\begin{aligned} H_{D,2d} =& -\mathfrak{B}[\langle k_z^2 \rangle (\sigma_x k_x - \sigma_y k_y) - (\sigma_x k_x k_y^2 - \sigma_y k_y k_x^2)] \\ \equiv& \beta_1 (\sigma_x k_x - \sigma_y k_y) - \frac{4\beta_3}{k_F^2} (\sigma_x k_x k_y^2 - \sigma_y k_y k_x^2) \\ \equiv& H_{D1} + H_{D3}, \end{aligned} \tag{2.4}$$

where $k_F = \sqrt{2\pi n}$ is the Fermi wave vector, and $n$ is the electron density, $\beta_1$ and $\beta_3$ are the strength of the linear and cubic Dresselhaus spin-orbit couplings, respectively. $\beta_1 = -\mathfrak{B}\langle k_z^2 \rangle \approx -\mathfrak{B}(\pi^2/d^2)$, and $\beta_3 = -\mathfrak{B}(k_F^2/4) = -\mathfrak{B}(\pi n/2)$. The cubic Dresselhaus term is small compared to the linear Dresselhaus term in the strong confinement and low density limit, i.e., $nd^2 \ll 1$.

If the confinement potential $V(z)$ is not symmetric, then the structure inversion asymmetry leads to the Rashba SOC [1, 9, 10]

$$H_R = \alpha(\sigma_x k_y - \sigma_y k_x), \tag{2.5}$$

where the strength of the Rashba SO coupling is proportional to the electric field along $z-$axis $\alpha = -\lambda \partial V/\partial z$. The proportional factor $\lambda$ depends on the band parameters and is typically a few orders of magnitude larger than the vacuum value $\lambda_0 = (\hbar/2mc)^2 = 3.7\times10^{-6}$ Å$^2$. The $\boldsymbol{k}\cdot\boldsymbol{p}$ perturbation theory predicts $\lambda = 5.2$ Å$^2$. Koralek *et al.* find this factor to be 6.7 Å$^2$ on a set of QWs with different doping asymmetry [21].

The total SO Hamiltonian is the summation of the individual contributions

$$H_{\rm SO} = H_R + H_{D1} + H_{D3}. \tag{2.6}$$

## Effective magnetic field

SOC is equivalent to the presence of an effective magnetic field with magnitude and orientation dependent on the momentum $\boldsymbol{k}$. The SO Hamiltonian Eq. 2.6 can be rewritten as

$$H_{\rm SO} = \gamma \boldsymbol{b}\cdot\boldsymbol{s} = \boldsymbol{\Omega}\cdot\boldsymbol{s}, \tag{2.7}$$

where $\boldsymbol{s} = \hbar\boldsymbol{\sigma}/2$ is the electron spin, $\gamma = g_e e/2m_e$ is the gyromagnetic constant, $\boldsymbol{b}(\boldsymbol{k})$ is the effective magnetic field, and $\boldsymbol{\Omega}(\boldsymbol{k}) = \gamma\boldsymbol{b}(\boldsymbol{k})$ is the resulting Larmor precession vector. The Kramers degeneracy requires that $\boldsymbol{b}(\boldsymbol{k}) = -\boldsymbol{b}(-\boldsymbol{k})$.

In the $k_\pm$ coordinates, $\boldsymbol{\Omega}$ is given by

$$\boldsymbol{\Omega}(\boldsymbol{k}) = 2\left\{\hat{\boldsymbol{x}}_+\left[\alpha-\beta_1-\frac{2\beta_3(k_+^2-k_-^2)}{k_F^2}\right]k_- - \hat{\boldsymbol{x}}_-\left[\alpha+\beta_1-\frac{2\beta_3(k_+^2-k_-^2)}{k_F^2}\right]k_+\right\}. \tag{2.8}$$

In Fig. 2.3, we plot the effective magnetic field (Lamor precession vector) in momentum space. The Rashba field ($\alpha\neq0, \beta_1=\beta_3=0$) is like vortex; the linear Dresselhaus field ($\beta_1\neq0, \alpha=\beta_3=0$) is like anti-vortex. The SU(2) ($\alpha=\beta_1\neq0, \beta_3=0$, see Sec. 2.3) precession vector is given by $\boldsymbol{\Omega}(\boldsymbol{k}) = -4\beta_1 k_+\hat{\boldsymbol{x}}_-$.

## Spin orientation

Combining Eq. (2.6) with the kinetic energy $\frac{1}{2}k^2$ (let $\hbar = m_c^* = 1$), we obtain the spin-split subband dispersion

$$E_\pm(\boldsymbol{k}) = \frac{k^2}{2} \pm \sqrt{(\alpha^2+\beta_1^2)k^2 + 4\alpha\beta_1 k_x k_y + \frac{16\beta_3^2}{k_F^4}k_x^2k_y^2k^2 - \frac{8\alpha\beta_3}{k_F^2}k_xk_yk^2 - \frac{16\beta_1\beta_3}{k_F^2}k_x^2k_y^2}, \tag{2.9}$$

and the eigenstates are

$$|\Psi_\pm(\boldsymbol{k})\rangle = |\boldsymbol{k}\rangle \otimes \frac{1}{\sqrt{2}}\begin{pmatrix} 1 \\ \pm e^{i\chi(\boldsymbol{k})}\end{pmatrix}, \tag{2.10}$$

where $\left|\boldsymbol{k}\right\rangle$ is the plane wave and

$$\chi(\boldsymbol{k}) = \arg[(\alpha k_y + \beta_1 k_x - \frac{4\beta_3}{k_F^2}k_xk_y^2) - i(\alpha k_x + \beta_1 k_y - \frac{4\beta_3}{k_F^2}k_yk_x^2)]. \tag{2.11}$$

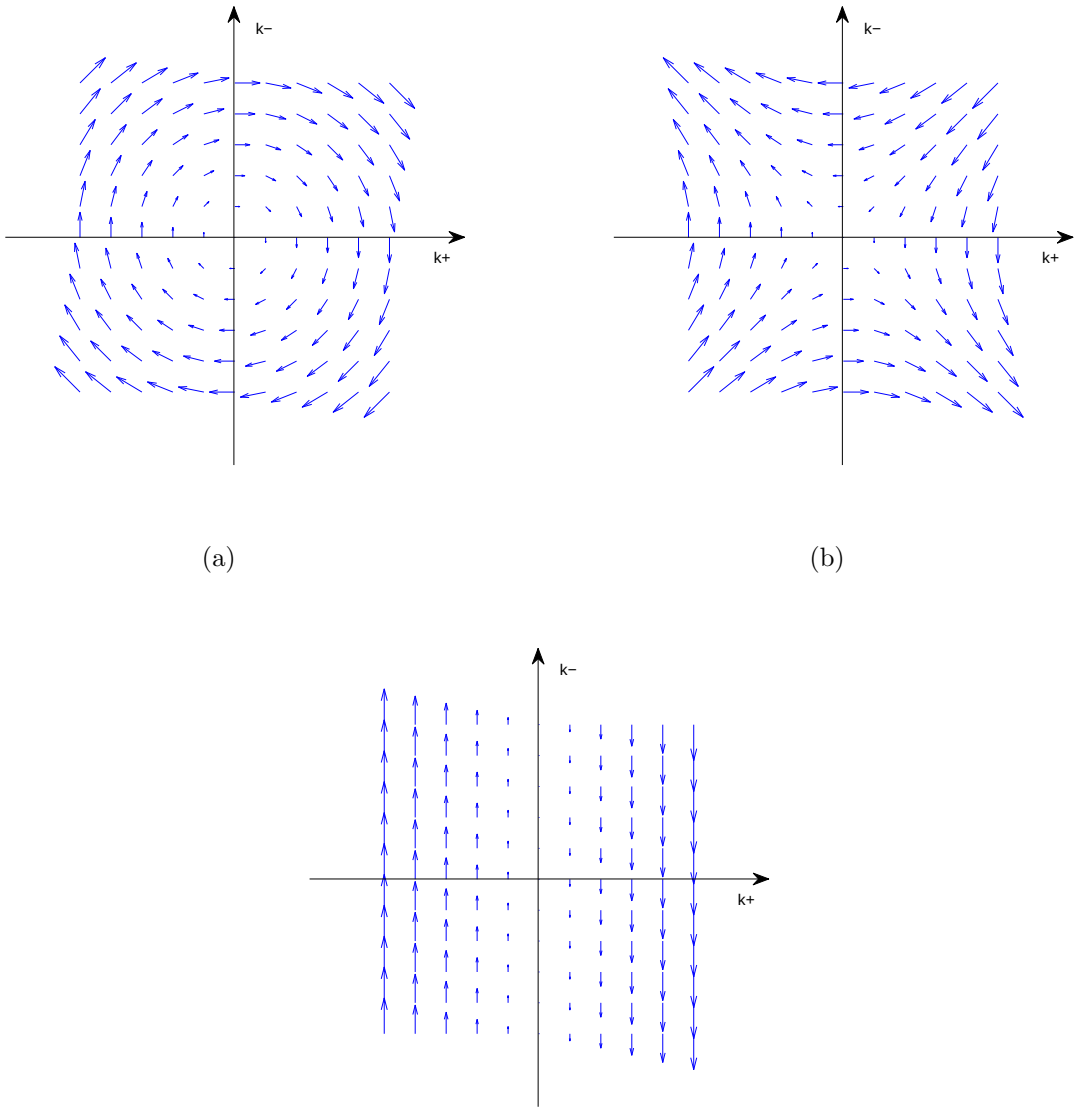


(a) (b)

(c)

Figure 2.3: Effective SO magnetic fields in the momentum space. (a) Rashba only; (b) linear Dresselhaus only; (c) SU(2).

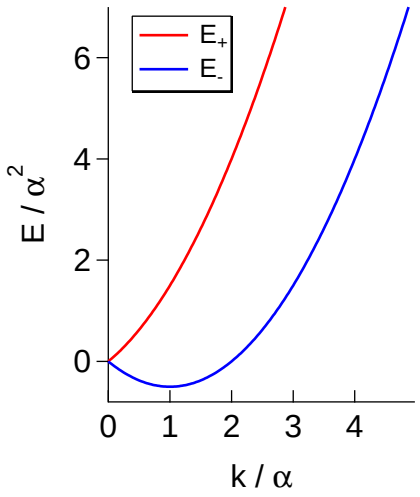


Figure 2.4: Spin-split dispersion of $E_{\pm}(\boldsymbol{k})$. The 2D bands are obtained by rotating the two branches around the energy axis.

The spin orientation of the spin eigenstates is given by

$$\langle \boldsymbol{\sigma}(\boldsymbol{k}) \rangle_{\pm} = \langle \Psi_{\pm}(\boldsymbol{k}) | \boldsymbol{\sigma} | \Psi_{\pm}(\boldsymbol{k}) \rangle = \pm \begin{pmatrix} \cos\chi \\ \sin\chi \\ 0 \end{pmatrix} \tag{2.12}$$

In the following, we discuss three special cases: Rashba only, linear Dresselhaus only and SU(2).

**i. Rashba only case**

$$E_{\pm}(\boldsymbol{k}) = \frac{k^2}{2} \pm \alpha k, \tag{2.13}$$

and $\chi(\boldsymbol{k}) = \arg(k_y - ik_x)$. Figure 2.4 shows the energy dispersion of the conduction band in the presence of Rashba SOC. The degeneracy is completely lifted for $\boldsymbol{k} \neq 0$. We obtain a ring of minima for $E_{-}(\boldsymbol{k})$ at finite wave vector $|\boldsymbol{k}_m| = \alpha$. The spin orientation of the eigenstates is plotted in Fig. 2.5a. Typically, $\alpha \sim 10^4$ cm$^{-1}$ and $k_F \sim 10^6$ cm$^{-1}$, for $n = 2 \times 10^{11}$ cm$^{-2}$, so the SO splitting $2\alpha k_F$ is much smaller than the Fermi energy $k_F^2/2$.

**ii. Linear Dresselhaus only case**

$$E_{\pm}(\boldsymbol{k}) = \frac{k^2}{2} \pm \beta_1 k, \tag{2.14}$$

and $\chi(\boldsymbol{k}) = \arg(k_x - ik_y)$. The spin orientation of the eigenstates is shown in Fig. 2.5b. Note that both the Rashba term and linear Dresselhaus term yield apparently the same spin splitting (Eqs. 2.13 and 2.14). Nevertheless the corresponding spin orientations are different due to the distinct symmetries of the the Rashba and Dresselhaus terms.

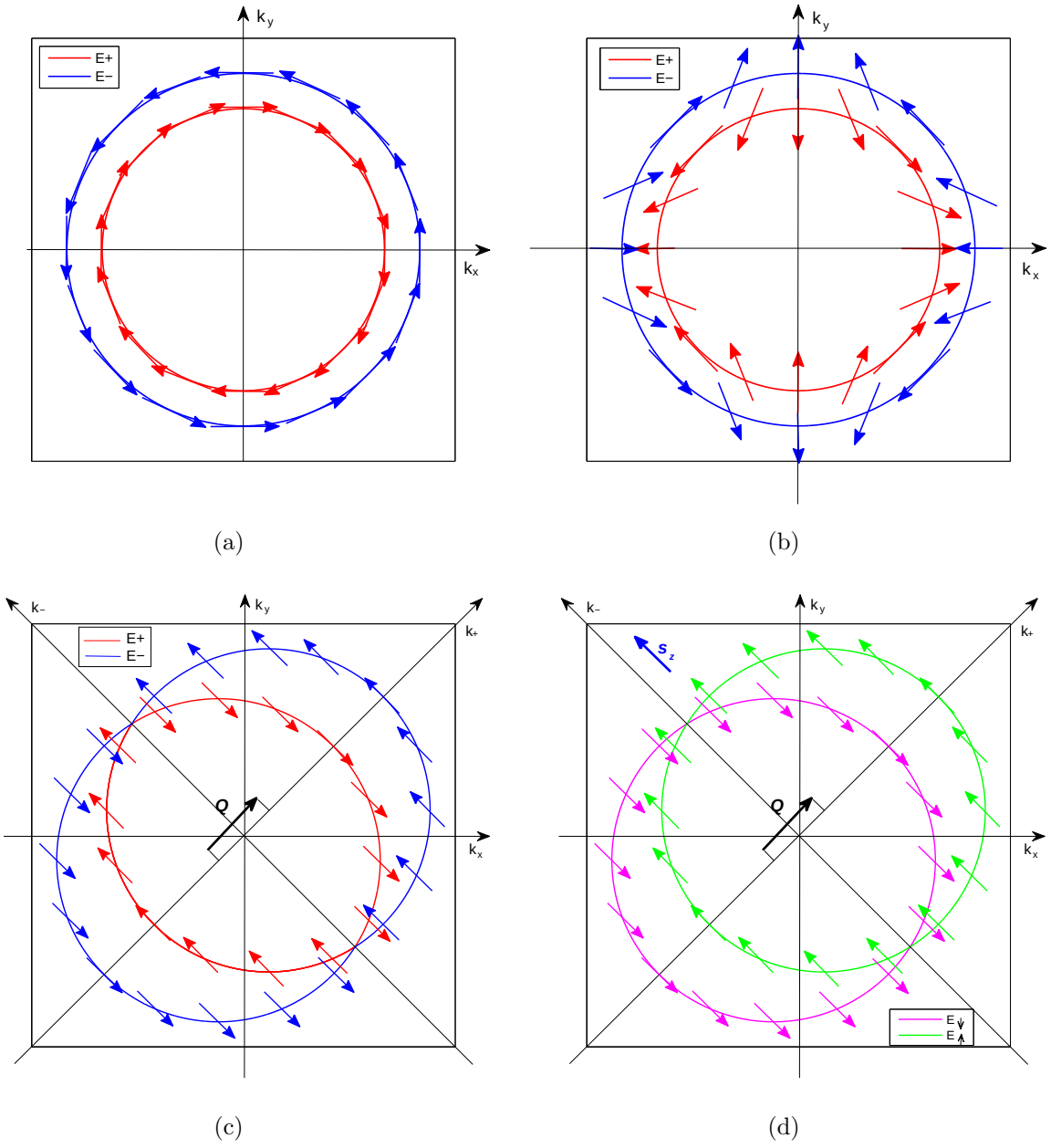


Figure 2.5: Spin orientation $\langle \boldsymbol{\sigma} \rangle$ of the eigenstates in the presence of SOC. (a) Rashba only; (b) linear Dresselhaus only; (c) SU(2); (d) SU(2) in the transformed spin basis.

**iii. SU(2) case**

$$\begin{aligned} E_{\pm}(\boldsymbol{k}) =& \frac{k^2}{2} \pm \sqrt{2}\beta_1|k_x + k_y| \\ \equiv& \frac{1}{2}(k_+^2 + k_-^2) \pm 2\beta_1|k_+|, \end{aligned} \tag{2.15}$$

where $k_\pm \equiv \frac{1}{\sqrt{2}}(k_x \pm k_y)$ and $\chi(\boldsymbol{k}) = \arg[(1-i)k_+]$. The spin eigenstates are shown in Fig. 2.5c. Notice that in all cases the Kramers degeneracy holds $E_\uparrow(\boldsymbol{k}) = E_\downarrow(-\boldsymbol{k})$ for any $\boldsymbol{k}$.

## 2.3 SU(2) symmetry and persistent spin helix

Usually, the SO interaction breaks the SU(2) spin symmetry, because the spin operator $\boldsymbol{S}$ does not commute with the Hamiltonian of the system. Spin memory is lost through the DP mechanism [11–14], in which spins precess around the instantaneous effective magnetic field originating from the SOC. However, it has been theoretically predicted [17] and experimentally observed [21] that SU(2) symmetry is recovered when the strengths of the two linear SOC are equal. The resulting conserved quantity is the so called persistent spin helix (PSH). We follow the arguments of Ref. [17] to discuss the new found SU(2) symmetry and PSH.

When $\alpha = \beta_1 \neq 0, \beta_3 = 0$, the Hamiltonian in the $k_\pm$ coordinates simplifies to

$$H = \frac{k^2}{2} + \sqrt{2}\beta_1 k_+(\sigma_x - \sigma_y). \tag{2.16}$$

Performing the global spin rotation generated by $U(\hat{\boldsymbol{n}}, \theta) = \exp(-\frac{i}{2}\theta\hat{\boldsymbol{n}} \cdot \boldsymbol{\sigma})$, where $\hat{\boldsymbol{n}} = \left(-\frac{1}{\sqrt{2}}, -\frac{1}{\sqrt{2}}, 0\right)$ and $\theta = \frac{\pi}{2}$, brings the Hamiltonian to the diagonal form

$$H \to H_{ReD} = U^\dagger H U = \frac{k^2}{2} - 2\beta_1 k_+ \sigma_z \tag{2.17}$$

$\sigma_z$ in the transformed spin basis corresponds to $\frac{1}{\sqrt{2}}(\sigma_y - \sigma_x)$ in the original spin basis. The energy bands are given by $E_{\downarrow,\uparrow} = \frac{1}{2}k^2 \pm 2\beta_1 k_+$. The bands have an important shifting property:

$$E_\downarrow(\boldsymbol{k}) = E_\uparrow(\boldsymbol{k} + \boldsymbol{Q}), \tag{2.18}$$

where $\boldsymbol{Q} = (Q_+, Q_-) = (4\beta_1, 0)$ and spin-up is along the $[1\bar{1}0]$ direction as shown in Fig. 2.5d.

The SU(2) symmetry is generated by the following operators

$$\begin{aligned} S_Q^- &= \sum_{\boldsymbol{k}} c_{\boldsymbol{k}\downarrow}^\dagger c_{\boldsymbol{k}+\boldsymbol{Q}\uparrow} \\ S_Q^+ &= \sum_{\boldsymbol{k}} c_{\boldsymbol{k}+\boldsymbol{Q}\uparrow}^\dagger c_{\boldsymbol{k}\downarrow} \\ S_0^z &= \sum_{\boldsymbol{k}} c_{\boldsymbol{k}\uparrow}^\dagger c_{\boldsymbol{k}\uparrow} - c_{\boldsymbol{k}\downarrow}^\dagger c_{\boldsymbol{k}\downarrow} \end{aligned} \tag{2.19}$$

where $c_{\boldsymbol{k}\uparrow,\downarrow}$ is the annihilation operators of spin-up and -down particles. Using the anti-commutation relations of the fermion operators $\{c_{\boldsymbol{k}\sigma}, c_{\boldsymbol{k}'\sigma'}^\dagger\} = \delta_{\boldsymbol{k}\boldsymbol{k}'}\delta_{\sigma\sigma'}$, $\{c_{\boldsymbol{k}\sigma}, c_{\boldsymbol{k}'\sigma'}\} = 0$, and $\{c_{\boldsymbol{k}\sigma}^\dagger, c_{\boldsymbol{k}'\sigma'}^\dagger\} = 0$, it is easy to show that $S_Q^-$, $S_Q^+$ and $S_0^z$ obey the commutation relations for angular momentum

$$\begin{aligned} [S_0^z, S_Q^\pm] &= \pm\, 2S_Q^\pm, \\ [S_Q^+, S_Q^-] &= S_0^z. \end{aligned} \tag{2.20}$$

The shifting property Eq. 2.18 ensures that these operators defined in Eq. 2.19 commute with the Hamiltonian

$$[H_{ReD}, c_{\boldsymbol{k}+\boldsymbol{Q}\uparrow}^\dagger c_{\boldsymbol{k}\downarrow}] = [E_\uparrow(\boldsymbol{k}+\boldsymbol{Q}) - E_\downarrow(\boldsymbol{k})] c_{\boldsymbol{k}+\boldsymbol{Q}\uparrow}^\dagger c_{\boldsymbol{k}\downarrow} = 0 \tag{2.21}$$

and similar for $c_{\boldsymbol{k}\downarrow}^\dagger c_{\boldsymbol{k}+\boldsymbol{Q}\uparrow}$, thus unveiling the SU(2) symmetry. This symmetry is immune to spin-independent perturbations as the spin operators commute with the finite-wave-vector particle density $\rho_{\boldsymbol{q}} = \sum_{\boldsymbol{k}} c_{\boldsymbol{k}+\boldsymbol{q}}^\dagger c_{\boldsymbol{k}}$. The corresponding conserved quantity of the symmetry, PSH, is generated by the operators $S_x(Q) = \frac{1}{2}(S_Q^+ + S_Q^-)$ and $S_y(Q) = \frac{1}{2i}(S_Q^+ - S_Q^-)$. The PSH is a helical spin density wave with wave vector $\boldsymbol{Q}$ parallel to [110] crystal direction in which the direction of the the spin polarization rotates in the $x, y$ plane of the transformed spin basis, i.e., the $(1\bar{1}0)$ plane of the crystal. Using the transient spin grating technique, Koralek et al. [21] observed the PSH mode experimentally by independently tuning the Rashba and linear Dresselhaus couplings.

# Chapter 3

# Random walk approach to spin dynamics

The main purpose of this chapter is to assess theoretically to what extent tuning SO interactions can be expected to increase the distance over which electron-spin polarization can propagate without decay. To predict the spin memory length it is necessary to determine how the applied field modifies both the real ($\Re$) and imaginary ($\Im$) parts of the normal-mode frequency, $\omega(q)$ of spin-polarization modes. The real part is related to the drift velocity whereas the imaginary part is related to the lifetime. The modification of $\Re\{\omega(q)\}$ is linear in $E$ (to lowest order), whereas the affect of $E$ on $\Im\{\omega(q)\}$ is quadratic. Kleinert and Bryksin [31, 33] recently have treated this to problem to linear order in $E$, using quantum kinetic theory, and obtained results for $\Re\{\omega(q)\}$.

We construct a semiclassical random walk model that tracks the electron's motion in real space and the propagation of its spin on the Bloch sphere. In Sec. 3.1, we introduce the random walk model, derive the equations of motion in the absence of an $E$ field, and solve for the spin-wave dispersion relations. We compare the results thus obtained with the earlier quantum kinetic theory approaches [17, 20]. In Sec. 3.2, we include an in-plane $E$ field, obtaining the equations of motion and the dispersion relations to quadratic order. We use the dispersion relations to analyze the motion of a spin-polarization packet in the presence of the in-plane field, for different regimes of field strength. We illustrate the results by focusing on representative SO couplings: linear Dresselhaus coupling only, the SU(2) case where Rashba and Dresselhaus terms are equal, and the case of SU(2) broken by a small cubic Dresselhaus term. A brief summary is given in Sec. 3.3.

## 3.1 Random walk model

As mentioned in Chapter 1, as an electron propagates between scattering events, SO coupling causes its spin to precess. Thus, as the electron performs an RW in real space, its spin performs an RW on the Bloch sphere. We consider a 2D electron gas with both structure

and bulk inversion asymmetry. The SO Hamiltonian for conduction band electrons in a III-V semiconductor QW grown in the [001] direction (taken as $\hat{\boldsymbol{z}}$-direction) is given by,

$$H_{SO} = \boldsymbol{\Omega} \cdot \boldsymbol{s}, \tag{3.1}$$

where,

$$\boldsymbol{\Omega} = 2k_F \left\{ \hat{\boldsymbol{x}} \left[ \alpha - \beta_1 - \frac{2\beta_3(v_x^2 - v_y^2)}{v_F^2} \right] v_y - \hat{\boldsymbol{y}} \left[ \alpha + \beta_1 - \frac{2\beta_3(v_x^2 - v_y^2)}{v_F^2} \right] v_x \right\}, \tag{3.2}$$

$\boldsymbol{s} = \hbar\boldsymbol{\sigma}/2$ is the electron spin, $v_x$ and $v_y$ are the components of velocity in the [110] and [1$\bar{1}$0] directions, $\alpha$, $\beta_1$, and $\beta_3$ are dimensionless quantities describing the strength of the Rashba, linear, and cubic Dresselhaus spin-orbit couplings, respectively, and $k_F$ is the Fermi wave vector. Spins precess about the effective SO field according to

$$\frac{d\boldsymbol{s}}{dt} = \boldsymbol{\Omega} \times \boldsymbol{s}. \tag{3.3}$$

We assume that the impurity potential is short range so that there is no correlation between the scattering events. In the absence of the $E$ field, electrons perform an isotropic 2D random walk with $\boldsymbol{v}_n$ (velocity between the $n$th and $(n+1)$th scattering events) given by $v_F\hat{\boldsymbol{t}}_n$, where $\hat{\boldsymbol{t}}_n = (\cos\theta, \sin\theta)$ is a random two-dimensional unit vector with a uniform probability density $p_n(\theta) = 1/2\pi$. The displacement from $n$th to $(n+1)$th step is given by

$$\boldsymbol{r}_{n+1} - \boldsymbol{r}_n = \boldsymbol{v}_n\tau, \tag{3.4}$$

where $\tau$ is the electron scattering time. In the following we consider $\Omega\tau$, the change in angle of the electron's spin between scattering events, as a small parameter. In this case we can obtain from Eq. (3.3) the change in the spin direction during the mean-free time as a series expansion in $\Omega\tau$,

$$\Delta\boldsymbol{s}_n \equiv \boldsymbol{s}_{n+1} - \boldsymbol{s}_n = \boldsymbol{\Omega}_n\tau \times \boldsymbol{s}_n + \frac{1}{2}\boldsymbol{\Omega}_n\tau \times (\boldsymbol{\Omega}_n\tau \times \boldsymbol{s}_n), \tag{3.5}$$

where we retain terms to second order.

Let $P_n(\boldsymbol{r})$ be the probability that after $n$ steps of random walk the electron arrives at position $\boldsymbol{r}$ and $D_n(\boldsymbol{r};\boldsymbol{s})$ be the conditional probability that given the electron is at $\boldsymbol{r}$, its spin is $\boldsymbol{s}$. The joint probability $P_n(\boldsymbol{r})D_n(\boldsymbol{r};\boldsymbol{s})$ satisfies the following recursion relation:

$$P_{n+1}(\boldsymbol{r})D_{n+1}(\boldsymbol{r};\boldsymbol{s}) = \langle P_n(\boldsymbol{r} - \boldsymbol{v}_n\tau)D_n(\boldsymbol{r} - \boldsymbol{v}_n\tau; \boldsymbol{s} - \Delta\boldsymbol{s}_n)\rangle, \tag{3.6}$$

where $\langle\rangle$ denotes average over $\hat{\boldsymbol{t}}_n$, i.e., $\langle A_n\rangle = \int_0^{2\pi} A_n(\theta)p_n(\theta)d\theta$. Once $P_n(\boldsymbol{r})D_n(\boldsymbol{r};\boldsymbol{s})$ is determined, the magnetization can be obtained from the following integral on the Bloch sphere:

$$\boldsymbol{m}_n(\boldsymbol{r}) = \int_{S^2} \boldsymbol{s}P_n(\boldsymbol{r})D_n(\boldsymbol{r};\boldsymbol{s})d\Sigma. \tag{3.7}$$

By substituting Eq. (3.6) into Eq. (3.7), we obtain,

$$\boldsymbol{m}_{n+1}(\boldsymbol{r}) = \langle \int_{S^2} \boldsymbol{s} P_n(\boldsymbol{r} - \boldsymbol{v}_n\tau) D_n(\boldsymbol{r} - \boldsymbol{v}_n\tau; \boldsymbol{s} - \Delta\boldsymbol{s}_n) d\Sigma \rangle. \tag{3.8}$$

Taylor series expansion on the right hand side of Eq. (3.8) yields,

$$\begin{aligned} \boldsymbol{m}_{n+1}(\boldsymbol{r}) =& \langle \int_{S^2} [\boldsymbol{s} + \boldsymbol{\Omega}_n\tau \times \boldsymbol{s} + \frac{1}{2}\boldsymbol{\Omega}_n\tau \times (\boldsymbol{\Omega}_n\tau \times \boldsymbol{s})] \{P_n(\boldsymbol{r}) D_n(\boldsymbol{r}; \boldsymbol{s}) \\ & - \boldsymbol{v}_n\tau \cdot \nabla [P_n(\boldsymbol{r}) D_n(\boldsymbol{r}; \boldsymbol{s})] + \frac{1}{2}\boldsymbol{v}_n\tau \cdot \nabla\nabla [P_n(\boldsymbol{r}) D_n(\boldsymbol{r}; \boldsymbol{s})] \cdot \boldsymbol{v}_n\tau \} d\Sigma \rangle. \end{aligned} \tag{3.9}$$

Again retaining terms to second order, we can write,

$$\boldsymbol{m}_{n+1} = \boldsymbol{I}_1 + \boldsymbol{I}_2 + \boldsymbol{I}_3, \tag{3.10}$$

where,

$$\begin{aligned} \boldsymbol{I}_1 =& \langle \int_{S^2} \boldsymbol{s} \{P_n(\boldsymbol{r}) D_n(\boldsymbol{r}; \boldsymbol{s}) - \boldsymbol{v}_n\tau \cdot \nabla [P_n(\boldsymbol{r}) D_n(\boldsymbol{r}; \boldsymbol{s})] \\ & + \frac{1}{2}\boldsymbol{v}_n\tau \cdot \nabla\nabla [P_n(\boldsymbol{r}) D_n(\boldsymbol{r}; \boldsymbol{s})] \cdot \boldsymbol{v}_n\tau \} d\Sigma \rangle, \end{aligned} \tag{3.11}$$

$$\boldsymbol{I}_2 = \langle \int_{S^2} [\boldsymbol{\Omega}_n\tau \times \boldsymbol{s}] \{P_n(\boldsymbol{r}) D_n(\boldsymbol{r}; \boldsymbol{s}) - \boldsymbol{v}_n\tau \cdot \nabla [P_n(\boldsymbol{r}) D_n(\boldsymbol{r}; \boldsymbol{s})] \} d\Sigma \rangle, \tag{3.12}$$

and

$$\boldsymbol{I}_3(\boldsymbol{r}) = \langle \int_{S^2} [\frac{1}{2}\boldsymbol{\Omega}_n\tau \times (\boldsymbol{\Omega}_n\tau \times \boldsymbol{s})] \{P_n(\boldsymbol{r}) D_n(\boldsymbol{r}; \boldsymbol{s})\} d\Sigma \rangle. \tag{3.13}$$

Upon performing the average over $\hat{\boldsymbol{t}}_n$, all terms that linear in $\boldsymbol{v}_n$ or $\boldsymbol{\Omega}_n$ vanish by symmetry, leading to,

$$\boldsymbol{I}_1 = \boldsymbol{m}_n + \Pi_{op}\tau^2 \boldsymbol{m}_n, \tag{3.14}$$

$$\begin{aligned} \boldsymbol{I}_2 =& -\hat{\boldsymbol{x}} \langle \Omega_{ny} v_{nx} \rangle \tau^2 \frac{\partial m_{nz}}{\partial x} + \hat{\boldsymbol{y}} \langle \Omega_{nx} v_{ny} \rangle \tau^2 \frac{\partial m_{nz}}{\partial y} \\ & + \hat{\boldsymbol{z}} \left( \langle \Omega_{ny} v_{nx} \rangle \frac{\partial m_{nx}}{\partial x} - \langle \Omega_{nx} v_{ny} \rangle \frac{\partial m_{ny}}{\partial y} \right) \tau^2, \end{aligned} \tag{3.15}$$

$$\boldsymbol{I}_3 = -\frac{\tau^2}{2} \left( \hat{\boldsymbol{x}} \langle \Omega_{yn}^2 \rangle m_{nx} + \hat{\boldsymbol{y}} \langle \Omega_{xn}^2 \rangle m_{ny} + \hat{\boldsymbol{z}} \langle \Omega_n^2 \rangle m_{nz} \right), \tag{3.16}$$

where

$$\Pi_{op} \equiv \frac{1}{2} \left( \langle v_x^2 \rangle \frac{\partial^2}{\partial x^2} + \langle v_y^2 \rangle \frac{\partial^2}{\partial y^2} \right). \tag{3.17}$$

Taking the continuum limit $\boldsymbol{m}_n \to \boldsymbol{m}(t)$, $(\boldsymbol{m}_{n+1} - \boldsymbol{m}_n)/\tau \to d\boldsymbol{m}/dt$, and substituting into Eq. (3.10), we obtain the equation of motion for the magnetization vector. Resolving the vector equation into components yields three scalar equations,

$$\frac{1}{\tau}\frac{\partial m_x}{\partial t} = \Pi_{op} m_x - \frac{1}{2}\langle \Omega_y^2 \rangle m_x - \langle \Omega_y v_x \rangle \frac{\partial m_z}{\partial x}, \tag{3.18}$$

$$\frac{1}{\tau}\frac{\partial m_y}{\partial t} = \Pi_{op} m_y - \frac{1}{2}\langle\Omega_x^2\rangle m_y + \langle\Omega_x v_y\rangle\frac{\partial m_z}{\partial y}, \tag{3.19}$$

$$\frac{1}{\tau}\frac{\partial m_z}{\partial t} = \Pi_{op} m_z - \frac{1}{2}\langle\Omega^2\rangle m_z + \langle\Omega_y v_x\rangle\frac{\partial m_x}{\partial x} - \langle\Omega_x v_y\rangle\frac{\partial m_y}{\partial y}. \tag{3.20}$$

Solving the equations of motion for eigenmodes with wave vector parallel to $\hat{\boldsymbol{x}}$ yields the dispersion relation,

$$\frac{i\omega_\pm(q)}{\tau} = \frac{1}{4}\left(2\langle\Omega^2\rangle - \langle\Omega_x^2\rangle\right) + \frac{1}{2}\langle v_x^2\rangle q^2 \pm \sqrt{\frac{\langle\Omega_x^2\rangle^2}{16} + q^2\langle\Omega_y v_x\rangle^2}. \tag{3.21}$$

This dispersion relation corresponds to modes in which the spin polarization spirals in the $x$-$z$ plane. Note that $\omega(q)$ is purely imaginary so that for all wave vectors the spin-polarization wave decays exponentially with time. However, the dispersion relation differs from ordinary diffusion, where $i\omega \propto 1/\tau + Dq^2$. The difference can be traced to the terms in Eq. (3.15) that are proportional to the first derivative of spin density with respect to position - these terms are absent in the usual diffusion equation. The coefficients of these additional terms are the cross-correlation functions, $\langle\Omega_x v_y\rangle$ and $\langle\Omega_y v_x\rangle$, which shows explicitly that the anomalous diffusion is a consequence of the correlation between the electron's motion in real space and the propagation of its spin on the Bloch sphere.

In the SU(2) case ($\alpha = \beta_1$ and $\beta_3 = 0$), Eq. (3.21) simplifies to,

$$i\omega_\pm(q) = \frac{1}{4}v_F^2\tau\left(q \pm q_0\right)^2 \equiv D(q \pm q_0)^2, \tag{3.22}$$

where $D \equiv v_F^2\tau/4$ and $q_0 \equiv 4k_F\beta_1$. The vanishing decay rate of the $\omega_-$ mode at $q = q_0$ indicates the appearance of a conserved quantity - a helical spin-polarization wave or "persistent spin helix" [17].

The dispersion relations obtained above for the spiral polarization waves are the same as those obtained previously, including the cubic Dresselhaus term [17, 20]. We note, however, that while the RW approach accurately describes the spiral coupling of $x$-$z$ components of spin, it does not capture the coupling between charge current and the $y$ component of spin that appears in the quantum kinetic formulation. This is because the RW approach does not include relaxation to the equilibrium state. In other words, between consecutive scattering events the electron's spin precesses about $\boldsymbol{b}(\boldsymbol{k})$ but has no tendency to spiral in toward it. Thus the well-known current-induced spin polarization (CISP) effect [19] is not predicted. To recover CISP requires adding to Eq. (3.3) a phenomenological Gilbert damping term,

$$\frac{d\boldsymbol{s}}{dt} = \lambda_G \boldsymbol{s} \times (\boldsymbol{\Omega} \times \boldsymbol{s}), \tag{3.23}$$

where $\lambda_G$ is the damping parameter.

## 3.2 Spin helix dynamics in the presence of an electric field

In this section, we explore how the spin dynamics change in the presence of an $E$ field parallel to the wave vector of the spin spiral. To include the effect of $E$ we add a drift term to the velocity at each random walk step,

$$\boldsymbol{v}_n = v_F \hat{\boldsymbol{t}}_n + v_d \hat{\boldsymbol{x}}, \tag{3.24}$$

where $v_d$ is the drift velocity assumed to be a linear function of $E$. We assume further that the electric field does not change the shape of the impurity potential and therefore the scattering probability density is still uniform.

The drift velocity modifies the precession vector, adding a fixed precession

$$\boldsymbol{\Omega}_d \equiv -2\hat{\boldsymbol{y}} k_F \left[\alpha + \beta_1 - \frac{2\beta_3(v_x^2 - v_y^2)}{v_F^2}\right] v_d, \tag{3.25}$$

to $\boldsymbol{\Omega}_n$ at each step of the random walk. Substituting and following the same strategy as before, we obtain,

$$\boldsymbol{I}_1(\boldsymbol{E}) = \boldsymbol{I}_1 - v_d \tau \frac{\partial \boldsymbol{m}}{\partial x}, \tag{3.26}$$

$$\boldsymbol{I}_2(\boldsymbol{E}) = \boldsymbol{I}_2 + \boldsymbol{\Omega}_d \tau \times \boldsymbol{m}, \tag{3.27}$$

$$\boldsymbol{I}_3(\boldsymbol{E}) = \boldsymbol{I}_3, \tag{3.28}$$

where the $\boldsymbol{I}_{1,2,3}(\boldsymbol{E})$ are the quantities $\boldsymbol{I}_{1,2,3}$ evaluated in the presence of the electric field. The field alters the equations of motion in two ways. First, new terms appear that are linear in $E$. The new term added to $\boldsymbol{I}_1$ converts the time derivative of $\boldsymbol{m}$ to the convective derivative, that is the time derivative in a frame moving with the drifting electrons. The term added to $\boldsymbol{I}_2$ indicates that the $E$ field introduces uniform precession about the $\hat{\boldsymbol{y}}$ axis, when viewed in the frame co-moving with $\boldsymbol{v}_d$. The second type of modification is quadratic in $E$; the field increases $\langle \Omega_y^2 \rangle$ by the additive factor $\Omega_d^2$ and the mean-square velocity $\langle v_x^2 \rangle$ by the factor $\langle v_d^2 \rangle$.

Solving for normal modes with wave vector parallel to $\hat{\boldsymbol{x}}$, we obtain

$$i\omega_\pm(q) = \frac{1}{4}\left(2\langle \Omega^2 \rangle - \langle \Omega_x^2 \rangle\right)\tau + \frac{1}{2}\langle v_x^2 \rangle \tau q^2 + i v_d q \pm \sqrt{\frac{\langle \Omega_x^2 \rangle^2 \tau^2}{16} + \left(q\langle \Omega_y v_x \rangle \tau + i\Omega_d\right)^2}. \tag{3.29}$$

To linear order in $E$, this dispersion relation is the same as that obtained by Kleinert and Bryksin [31, 33]. In the presence of the electric field $\omega(q)$ acquires a real part, which describes the propagation of spin polarization. Equation (3.29) also describes the modifications of the spin polarization lifetime that appear at second order in $E$. In the following we discuss the spin dynamics that emerge from this dispersion relation for representative SO Hamiltonians.

## SU(2) case

For the case of $\alpha = \beta_1, \beta_3 = 0$, the dispersion relation simplifies to,

$$i\omega_{\pm}(q) = D\left(1 + 2\lambda^2\right)(q \pm q_0)^2 + iv_d\,(q \pm q_0)\,, \tag{3.30}$$

where $\lambda \equiv v_d/v_F$. To distinguish the lifetime and propagation effects we write the dispersion relation in the form,

$$i\omega(q) = \gamma(q) + i\dot{\phi}(q), \tag{3.31}$$

where $\gamma(q)$ is the decay rate and $\dot{\phi}(q)$ is the rate of phase advance. The real and imaginary parts of $i\omega_-(q)$, corresponding to the longer lived of the two modes, are plotted in Fig. 3.1. As is apparent from Fig. 3.1a, the spin polarization lifetime, $1/\gamma_-(q)$ remains infinite at the PSH wave vector, despite the presence of the electric field. This result is consistent with the theoretical prediction that at the SU(2) point the spin helix generation operators commute with all perturbation terms that are not explicitly spin dependent [17]. However, the field increases the effective diffusion constant by the factor $\lambda^2$ so that the decay rate for $q \neq q_0$ increases rapidly when the drift velocity approaches the thermal velocity of the electrons. The spin helix generation operators won't commute with the Hamiltonion if there exists a spatial disorder of SO interactions [34, 35].

The rate of phase advance [plotted in Fig. 3.1b] vanishes at $q = q_0$, i.e., the PSH is stationary, despite the fact that the Fermi sea of electrons is moving by with average velocity $\boldsymbol{v}_d$. Moreover, spin spirals with $q < q_0$ will appear to move backward, that is, opposite to the direction of electron flow. Although unusual, this property can be understood by considering the spin dynamics in a frame moving with velocity $\boldsymbol{v}_d$. In this frame $\boldsymbol{E}$ parallel to $\hat{\boldsymbol{x}}$ is perceived as a precession vector $\boldsymbol{\Omega}_d = -4\beta_1 v_d \hat{\boldsymbol{y}} = -v_d q_0 \hat{\boldsymbol{y}}$. Therefore in the moving frame $\phi_{\pm}(x', t') = \pm qx' - v_d q_0 t$. Transforming back to the laboratory frame then yields $\dot{\phi}_{\pm}(q) = v_d(q \pm q_0)$.

The nature of spin propagation at the SU(2) symmetry point can be made more clear if we Fourier transform from the wave vector to spatial domain. If we inject a $\delta-$function stripe of $z$ polarized spins at $x = 0$, the space-time evolution of $S_z$ is proportional to the propagator, $G_z(x, t)$, where

$$G_z(x,t) \propto \int dq e^{iqx}\left(A_+ e^{-i\omega_+ t} + A_- e^{-i\omega_- t}\right), \tag{3.32}$$

where $A_+$ and $A_-$ are the weighting factors for the passive and active modes, respectively and $A_+ = A_- = 1/2$ in the SU(2) case. Upon substituting the dispersion relations $\omega_{\pm}(q)$, we obtain,

$$G_z(x,t) \propto \frac{1}{\sqrt{Dt}} \cos(q_0 x) \exp\left[-\frac{(x - v_d t)^2}{4Dt}\right]. \tag{3.33}$$

The spin propagator is the product of a Gaussian envelope function and a static spin wave with wave vector $q_0$. The envelope function is the one-dimensional diffusion propagator with width proportional to $\sqrt{Dt}$ and drift velocity $v_d$. An illustration of the space-time evolution

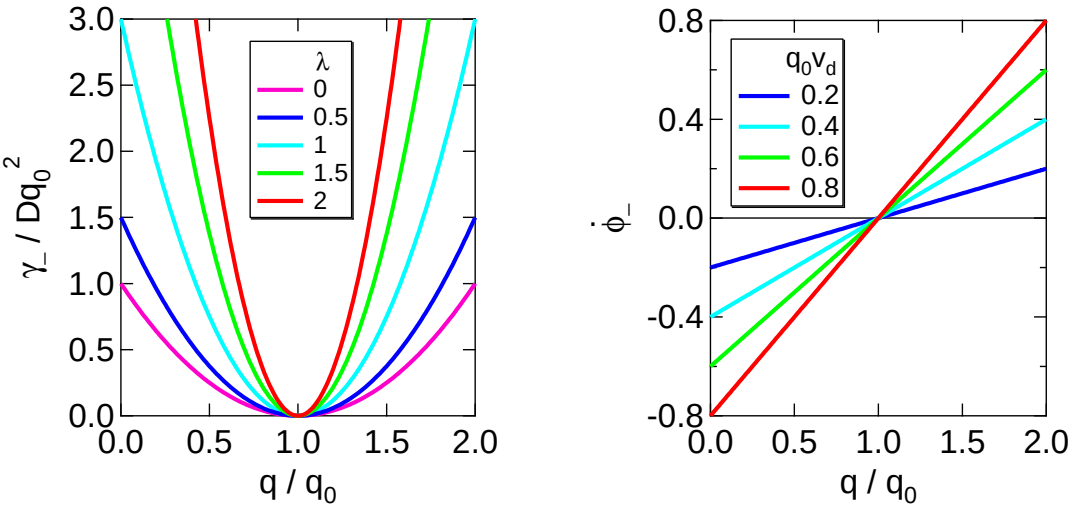


(a) (b)

Figure 3.1: The dispersion relations for (a) the decay rate and (b) the rate of phase change of the SO enhanced mode in the SU(2) case. (a) The decay rate $\gamma_-(q)$ increases with the drift velocity ($\lambda \equiv v_d/v_F$) but always vanishes at the resonant wave vector $q_0$. (b) The rate of phase change $\dot{\phi}_-(q)$ is proportional to the drift velocity $v_d$ and it crosses zero at the resonant wave vector $q_0$.

described by this propagator is provided Fig. 3.2, for a drift velocity $v_d = 2Dq_0$. Note that the phase of the spin wave modulated by the Gaussian envelope remains stationary as the packet drifts and diffuses. This contrasts with the more familiar wave packet, where the modulated wave and envelope functions both propagate, albeit with velocities that may differ.

## SU(2) broken by cubic Dresselhaus term

When SU(2) is exact, the integral of the Gaussian envelope function is conserved, even in the presence of an $E$ field. However, Stanescu and Galitski [20] have shown theoretically that $\beta_3$, which is nonzero in real systems, breaks SU(2). Koralek *et al.* [21] verified experimentally that $\beta_3$ is indeed the factor that limits PSH lifetime in experiments on (001) GaAs quantum wells. In this section we calculate the dispersion relation and spin packet time evolution in the presence of a small cubic Dresselhaus term.

It was shown previously that when $\beta_3$ is small, the maximum lifetime occurs when the Rashba interaction $\alpha = \beta_1 - \beta_3$ (Ref. [20]). We consider a QW with Rashba coupling tuned to this value and assume that $\beta_3 \ll \beta_1$. This condition is met in QWs in the 2D limit, where $k_F d \ll 1$ ($d$ is the well width). In this case the dispersion relation in the presence of the

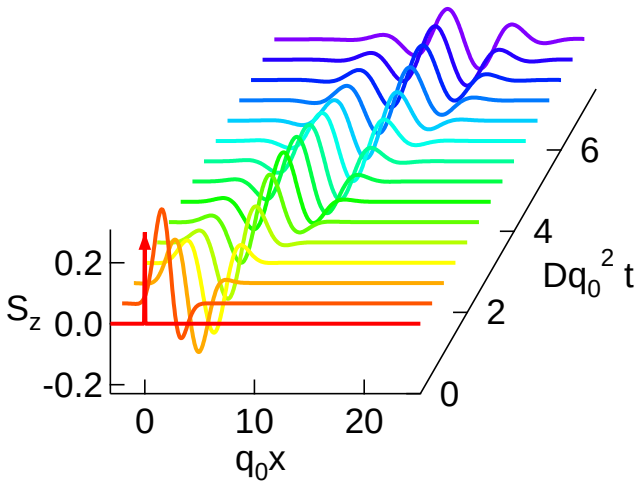


Figure 3.2: The space-time evolution of $S_z$ with a normalized $\delta$-function injection at $x = 0, t = 0$, and drift velocity $v_d = 2Dq_0$ in the SU(2) case. The spin polarization develops into a conserved stationary wave with a Gaussian wave packet.

electric field can be written as

$$i\omega_{\pm}(q) \cong 6Dk_F^2\beta_3^2 + D\left(q \pm q_0\right)^2 + iv_d\left(q \pm q_0\right) \mp iv_d\Delta q, \tag{3.34}$$

where $q_0 \equiv 4k_F(\beta_1 - \beta_3)$ and $\Delta q = 2k_F\beta_3$. Performing the Fourier transform to obtain the space-time evolution of a spin packet, we obtain,

$$G_z(x,t) \propto \frac{1}{\sqrt{Dt}} e^{-6Dk_F^2\beta_3^2 t} \cos(q_0 x - v_d\Delta q t) \exp\left[-\frac{(x - v_d t)^2}{4Dt}\right]. \tag{3.35}$$

In the presence of the cubic Dresselhaus interaction the integral of the Gaussian envelope is no longer conserved. The decay rate can be written in the form,

$$\gamma = \frac{3}{8} D q_0^2 \left(\frac{\beta_3}{\beta_1}\right)^2, \tag{3.36}$$

illustrating that although the decay rate is nonzero, it is reduced relative to the DP relaxation rate by a factor $\approx (\beta_3/\beta_1)^2$. This ratio is expected theoretically,[32] and has been verified experimentally,[21] to be determined by the relation,

$$\frac{\beta_3}{\beta_1} = \frac{k_F^2 d^2}{4\pi^2}. \tag{3.37}$$

For quite reasonable QW parameters a $\beta_3$ to $\beta_1$ ratio of 1:100 can be achieved, equivalent to a lifetime enhancement relative to the DP spin memory time on the order of $10^4$.

### Linear Dresselhaus coupling

Finally, we consider a fully symmetric well in which only the linear Dresselhaus coupling exists. To make comparison with the SU(2) situation, we set the strength of the linear Dresselhaus coupling be $2\beta_1$, so that the resonant wave vector is at $q \simeq q_0 = 4k_F\beta_1$. The dispersion relations $\gamma_-(q)$ and $\dot{\phi}_-(q)$ obtained by substituting $\alpha = \beta_3 = 0$ and replacing $\beta_1$ by $2\beta_1$ in Eq. (3.29) are plotted in Fig. 3.3. Some qualitative features of the dispersion relations are similar to the SU(2) case, in that $\gamma_-(q)$ has a global minimum and $\dot{\phi}_-(q)$ crosses zero at $q \simeq q_0$. The most important difference is that the minimum $\gamma_-(q)$ does not reach zero, and therefore the spin spiral does decay. In the limit of low electric field, the lifetime of the spin spiral is only about a factor of 2 longer than the $q = 0$ (DP) lifetime.

The propagation of a spin packet in the linear-Dresselhaus-only case is illustrated in Fig. 3.4, using the same initial condition and drift velocity as in SU(2) case. We performed numerical integration of Eq. (3.32) to obtain the propagator. As we have seen previously, a drifting and diffusing envelope function modulates a spiral spin wave. However, now the spiral spin fades very quickly. The contrast between linear Dresselhaus only and SU(2) is illustrated in Fig. 3.5, which is a plot of the integral of the envelope as a function of time. After a rapid initial decay, the integral is constant in the SU(2) case, whereas with only the linear Dresselhaus interaction the integrated amplitude decays exponentially with rate $\simeq Dq_0^2$.

Figure 3.6 presents another way of visualizing the difference in propagation for the SU(2) [Fig. 3.6a] and linear-Dresselhaus-only [Fig. 3.6b] Hamiltonians. The $z$ component of spin polarization is shown (with color coded amplitude) as a function of time on the vertical axis and position on the horizontal axis. It is clear, from the vertical orientation of the contours that the positions of the nodes and antinodes of $S_z$ are fixed in space.

## 3.3 Summary and conclusion

We have developed a random walk model to describe the time evolution of electron spin in two dimensions in the presence of Rashba and Dresselhaus interactions. From the random walk model we derived equations of motion for spin polarization and obtained dispersion relations for $\boldsymbol{q}$ parallel to one of the symmetry directions of the Rashba/Dresselhaus Hamiltonian. In Sec. 3.1, we showed that the dispersion relations for spin-polarization waves that spiral in the plane containing the surface normal and the wave vector are identical to those obtained from previous analyses [17, 20]. The random walk approach is instructive in showing, in a simple but explicit way, how anomalous spin diffusion and the persistent spin helix arise from nonvanishing correlations between the velocity and spin precession vectors.

In Sec. 3.2, we obtained dispersion relations for spin-polarization waves that include the effects of an electric field parallel to $\boldsymbol{q}$, to second order in $E$. The terms linear in $E$ are equivalent to those obtained from the quantum kinetic approach.[31, 33] To first order in $E$, the field introduces a precession vector in the plane of the 2DEG and perpendicular to

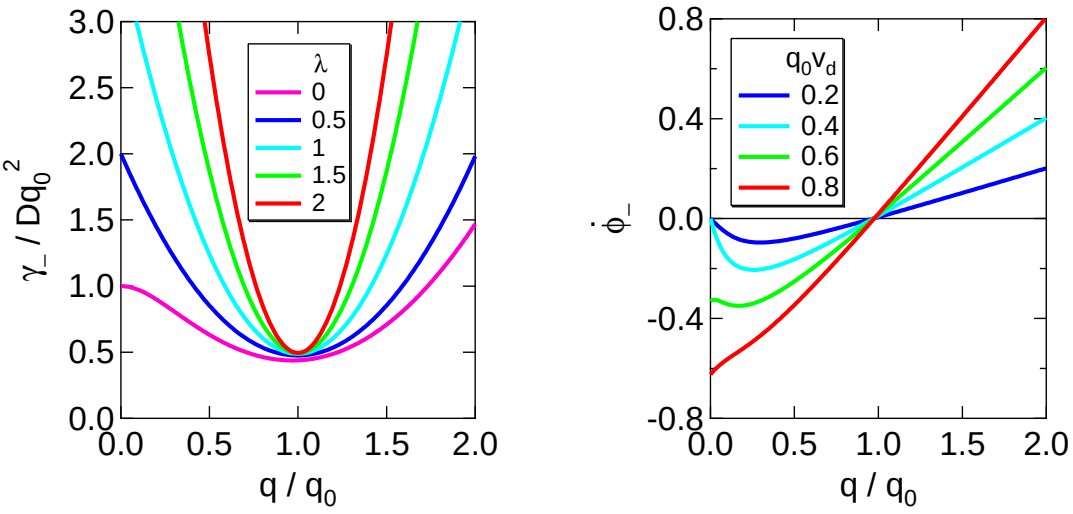


(a) (b)

Figure 3.3: The dispersion relations for (a) the decay rate and (b) the rate of phase change of the SO enhanced mode in the linear-Dresselhaus-only case. The main features resemble those in the SU(2) case, both $\gamma_-(q)$ show a minimum and $\dot{\phi}_-(q)$ vanishes at $q_0$, but the lifetime is finite in this case.

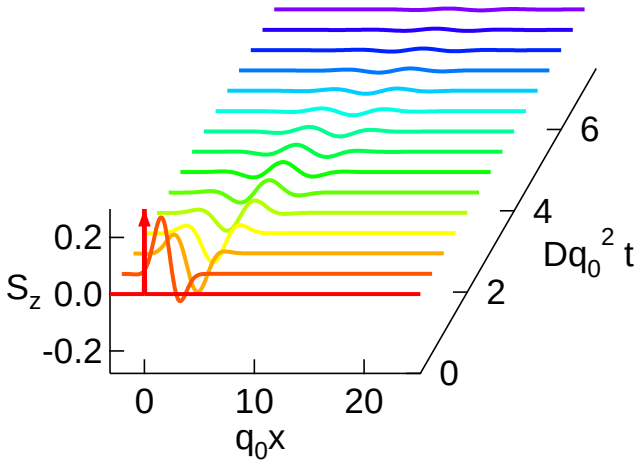


Figure 3.4: The space-time evolution of $S_z$ in the linear-Dresselhaus-only case with the same initial condition and applied $E$ field as in the SU(2) case. The features are similar to those in the SU(2) case, except the envelope function decays exponentially.

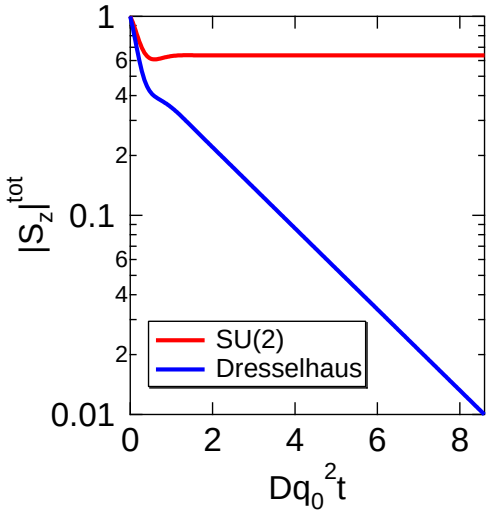


Figure 3.5: The the absolute value of the spin polarization integrated over position as a function of time. In the SU(2) case, $|S_z|^{tot}$ is conserved after an initial decay; while in the linear-Dresselhaus-only case, $|S_z|^{tot}$ decays exponentially.

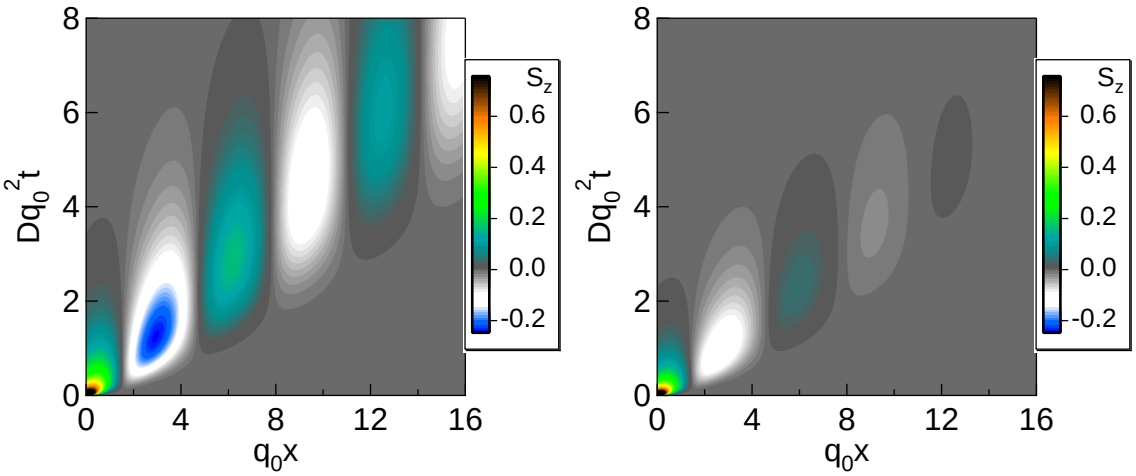


Figure 3.6: The space-time images of the spin polarization in the (a) SU(2) and (b) linear-Dresselhaus-only cases, respectively.

$\boldsymbol{E}$. The precession about the $y$ axis gives rise to an unusual behavior in that the spiral with wave vector $q_0$ is stationary in space despite the motion of electrons in the field; waves with $q > q_0$ propagate in the same direction as the drifting electrons while those with $q < q_0$ propagate "backward." The terms that are second order in $E$ affect the decay rate of spin polarization without changing the velocity. The solutions obtained when these terms are included point to the special properties of waves with wave vector $q_0$, whose lifetime turns out to be unchanged by the field. However, the decay rate of the all other waves increases, in proportion to $(q - q_0)^2$.

We illustrated these results by considering three representative spin-orbit Hamiltonians: SU(2) symmetric or $\alpha = \beta_1$ and $\beta_3 = 0$; SU(2) broken by a small but nonzero $\beta_3$; and linear Dresselhaus coupling only or $\alpha = \beta_3 = 0$. In order to show the nature of spin propagation more clearly, we Fourier transformed the solutions from wave vector to real space and obtained the dynamics of spin-polarization packets. In all cases the spin packets move at the electron drift velocity. In the SU(2) case the integrated amplitude of the spin spiral is conserved, while in the linear-Dresselhaus-only case the amplitude decays with a rate $\sim Dq_0^2$. When SU(2) is weakly broken by small, but nonzero $\beta_3$, the integrated amplitude decays at a rate $\sim (\beta_3/\beta_1)^2 Dq_0^2$.

The conclusions reached by our analysis of the RW model are consistent with a recent Monte Carlo study of a specific 2DEG system, a (001) $In_{1-x}Ga_xAs$ quantum well with carrier density $\sim 10^{12}$ cm$^{-2}$ (Ref. [36]). In this study spin polarization dynamics were calculated under conditions of steady state injection from a ferromagnetic contact. For $\alpha/\beta_1$ ratios that are close to unity, the spin polarization is conserved over several wavelengths of the PSH, despite the fact that transport takes place in the diffusive regime. Moreover, the polarization is not diminished with increasing electric field. The authors point out that the PSH effect can be used to achieve a novel variation of the Datta-Das spin-field-effect transistor [37] in which a gate electrode modulates the $\alpha$ to $\beta_1$ ratio only slightly away from unity. This has the effect of varying the wavelength of the PSH without significantly reducing its lifetime. Thus small changes in gate voltage can in principle lead to large changes in source to drain conductance. Whether such a device can actually be realized depends on two factors: fabricating ferromagnetic injectors and analyzers with high figures of merit, and demonstrating that the PSH effects that have been observed at temperatures below $\sim 100$ K [21] can be realized at room temperature.

# Chapter 4

# Transient grating and Doppler velocimetry

Transient grating spectroscopy (TGS) [38] is a powerful time-resolved optical tool to study a broad range of phenomena, such as quasiparticle propagation in high $T_c$ superconductors [39] and spin dynamics in semiconductors [21, 27, 40]. In this technique, a pair of coherent pulses excite the media to create a transient charge/spin density wave on the surface of the sample by inference. The laser induced dynamic grating acts as an optical diffraction grating for time-delayed probe pulses. Its temporal evolution provides the information of the relaxation and transport processes of the excitations created by the laser beams. Previously, only diffusion and lifetime were observed by time-resolving the amplitude of light diffracted from the periodic charge/spin density wave. This technique cannot be applied to tracking the motion of current-driven charge/spin packet because diffraction amplitude is insensitive to translation of the center of mass of a periodic structure. Here we describe a new experimental technique, Doppler spin velocimetry, capable of resolving displacements of charge/spin density at the level of 1 nm on a picosecond time scale. This is accomplished through the use of heterodyne detection [28–30, 41, 42] to measure the optical phase of the diffracted light.

## 4.1 Transient grating setup

The pulsed (100 fs) laser beam from a modelocked Ti:Sapphire oscillator (KM lab) is first split into pump and probe arms by a beam splitter. The intensity of the pump beam is modulated at 100 kHz by a photoelastic modulator combined with a polarizer. The probe beam bounds off a stepper motor, which can change the optical path in steps of one micro. Both beams are then focused onto a diffraction grating in transmission, the "phase mask", which is designed to have maximum intensity at $\pm 1$ orders, so after the phase mask, both pump and probe beams are split into two identical replicas to form the "boxcar" geometry [30] as shown in Fig. 4.1. The resulting four beams then focus on the same spot of the sample

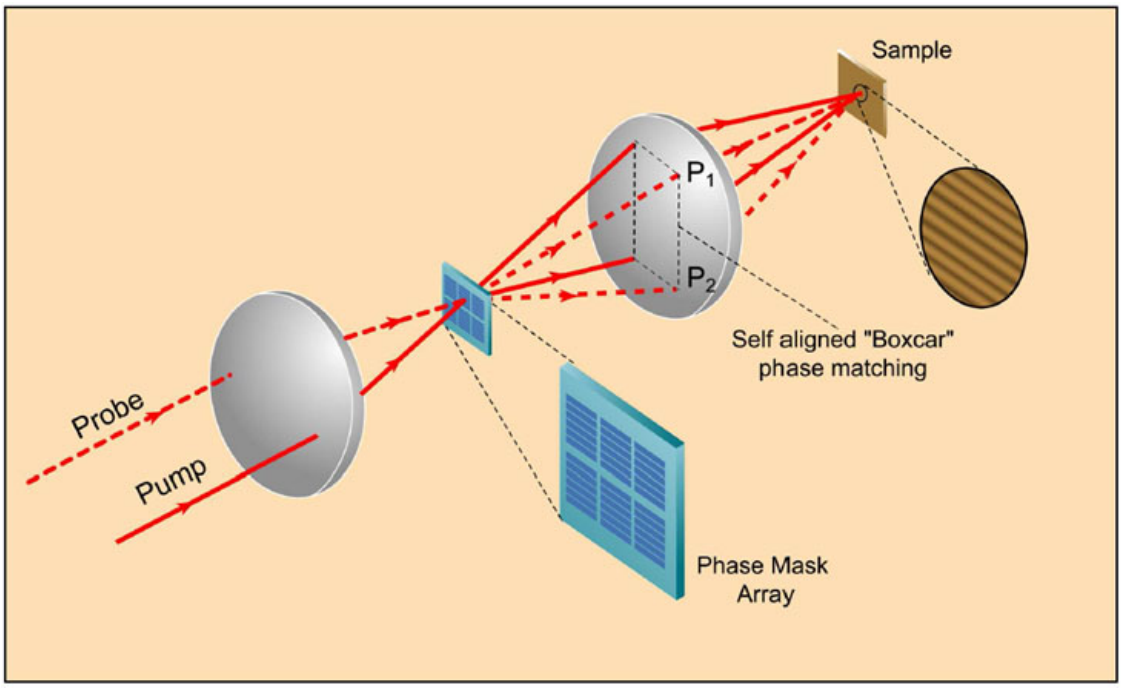


Figure 4.1: Transient grating setup. The picture is taken from [43].

by a large spherical mirror (shown as the second lens in Fig. 4.1). We have an array of phase masks with different periods. It is mounted on an $x - y - z$ translation stage, which allows us to change the $q$ of the grating by translating the mask. To create a spin grating, we have a half-wave plate inset into the beam path of the lower pump and probe beams to flip the polarization by 90°, and therefore the polarization of the two pump beams are perpendicular to each other and the polarization of the two probe beams are also perpendicular to each other as shown in Fig. 4.5a.

## 4.2 Generate the transient gratings

Excitation of a semiconductor with a single beam of above band-gap energy photons injects an equal population of electrons and holes, whose spatial distribution follows the intensity of the laser spot. In TGS two non-collinear beams of light pulses interfere at the sample surface, creating a pattern of intensity and photon helicity that depends on the relative angle and polarization state of the two beams. When the two beams are polarized parallel to each

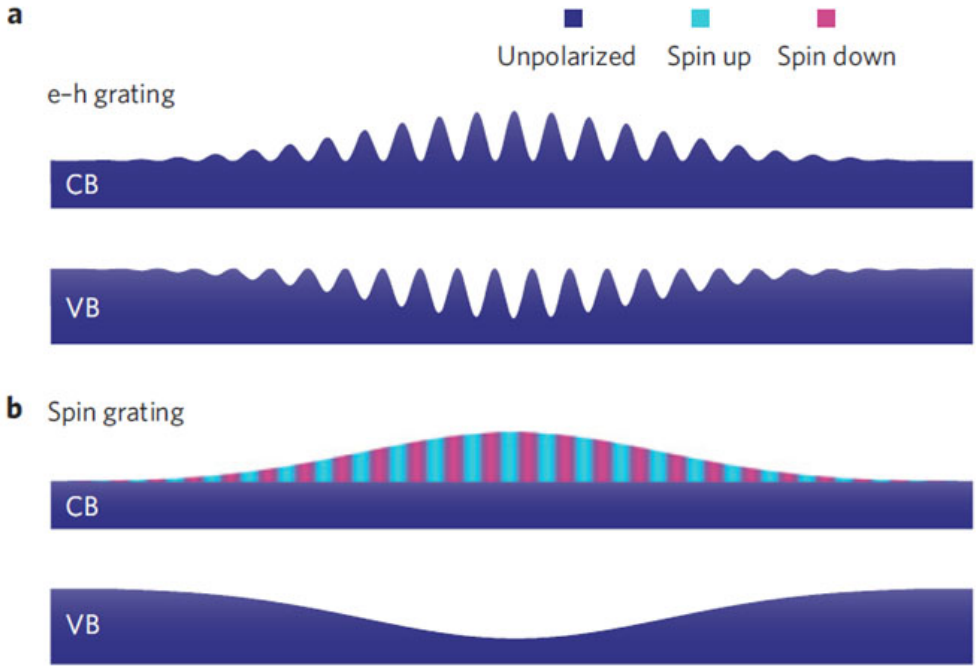


Figure 4.2: Illustration of photoinduced transient gratings in a doped quantum well. (a) The photoinduced e-h grating consists of a sinusoidal variation of the e-h density modulated by the Gaussian envelope of the laser spot. In the presence of an applied E field, the e-h grating moves at the ambipolar velocity. (b) The photoinduced spin grating consists of a sinusoidal modulation of the out-of-plane component of spin density coexisting with the Gaussian distribution of electrons and holes. The hole spins randomize on the sub-picosecond timescale and so are shown as unpolarized. CB: conduction band; VB: valence band.

other, the electric field at the surface is given by

$$\begin{aligned}\boldsymbol{E} =& E_0[\hat{\boldsymbol{y}}\exp(i\boldsymbol{k_1}\cdot\boldsymbol{r}) + \hat{\boldsymbol{y}}\exp(i\boldsymbol{k_2}\cdot\boldsymbol{r})] \\ =& E_0\hat{\boldsymbol{y}}\left[\exp\left(i\frac{qx}{2}\right) + \exp\left(-i\frac{qx}{2}\right)\right] \text{ (up to an overall phase factor)} \\ =& 2E_0\hat{\boldsymbol{y}}\cos\frac{qx}{2},\end{aligned} \tag{4.1}$$

where $\boldsymbol{q} = \boldsymbol{k_2} - \boldsymbol{k_1}$ and $|\boldsymbol{k_1}| = |\boldsymbol{k_2}| = k$ is the wave vector of the light. Interference creates a standing wave of laser intensity given by $I(x) = E_0^2(1 + \cos qx)$ generating the sinusoidal pattern of photoinduced electron-hole ($e$-$h$) density with wave vector $q$ shown in Fig. 4.2a.

On the other hand, orthogonal polarization generates a standing wave of photon helicity, while maintaining spatially uniform intensity (on the scale of the laser spot) and therefore

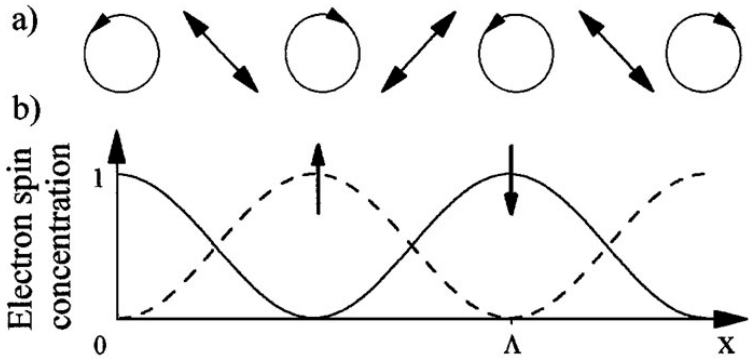


Figure 4.3: (a) The photon helicity wave induced by the interference of two orthogonally polarized light beams. (b) Concentration of spin-up and spin-down electrons generated by the photon helicity grating. The figure is taken from Ref. [27].

the *e-h* density [27]. The electric field is given by

$$\begin{aligned} \boldsymbol{E} =& E_0[\hat{\boldsymbol{x}} \exp(i\boldsymbol{k_1}\cdot\boldsymbol{r}) + \hat{\boldsymbol{y}} \exp(i\boldsymbol{k_2}\cdot\boldsymbol{r})] \\ =& E_0 \left[ -\hat{\boldsymbol{e}}_L \left( \cos\frac{qx}{2} - \sin\frac{qx}{2} \right) e^{-i\pi/4} + \hat{\boldsymbol{e}}_R \left( \cos\frac{qx}{2} + \sin\frac{qx}{2} \right) e^{i\pi/4} \right], \end{aligned} \tag{4.2}$$

where $\hat{\boldsymbol{e}}_{L/R} = -\dfrac{i\hat{\boldsymbol{y}} \pm \hat{\boldsymbol{x}}}{\sqrt{2}}$ is the basis for the left/right circularly polarized light. The intensity $I(x) = I_L(1-\sin qx) + I_R(1+\sin qx)$ can be viewed as the sum of standing wave of left and right polarized intensity that are shifted relative to each other by a half wavelength illustrated in Fig. 4.3a. Optical selection rules in GaAs cause photon helicity to be imprinted in the out of plane $z$ component of the angular momentum of the photoinduced *e-h* gas (Ref. [27] and c.f. Sec. 2.1). Because hole spins depolarize on a sub-picosecond time scale, the excited state for $t > 1$ ps comprises an electron spin density wave (SDW) accompanied by a charge compensating gas of unpolarized holes, as illustrated in Fig. 4.2b.

## 4.3 Doppler velocimetry

To measure the drift of a charge/spin density wave, we photo-inject the charge/spin grating into a high mobility $n$-doped GaAs/AlGaAs quantum wells (EF23 from wafer VB0355) subjected to an in-plane electric field $\boldsymbol{E}$ parallel to its wave vector $\boldsymbol{q}$ as displayed in figure 4.4. After the injection, the density wave drifts with the Fermi sea of electrons. The phase of the diffracted probe beam carries information about the position of the grating in space, which is decoded through the use of heterodyne detection to measure the optical phase of the diffracted light.

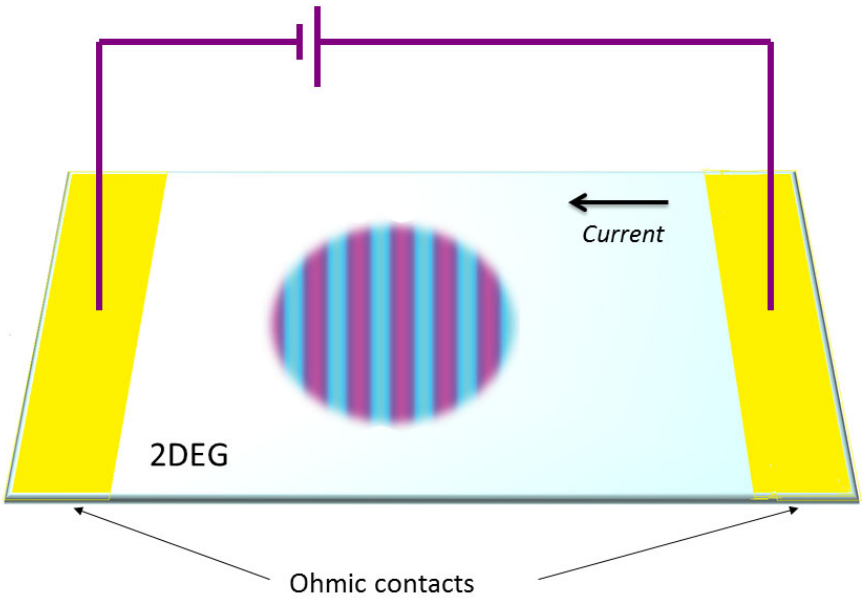


Figure 4.4: A top view of the sample: the 2DEG, ohmic contacts, applied voltage and photo-injected SDW. The blue and purple represent alternating spin up and spin down polarization.

## Probe the grating

The imprinted charge/spin density wave induces variation in the local index of refraction $\delta n$ and therefore acts as a transient optical grating, whose subsequent dynamics can be monitored via the diffraction of a time-delayed probe pulse. To detect the diffracted light, we use a heterodyne technique, in which one of the probe beams, acting as a local oscillator (LO), transmits though the grating and is mixed with the diffracted beam of the other probe pulses in a Si photodiode as illustrated in Fig. 4.5b. The "boxcar" geometry guarantees that the $m = 1$ order of the diffract beam of one probe is colinear with the transmitted beam of the other probe. For charge grating, the polarization of the diffracted beam remains unchange. However, for spin grating, the polarization rotates by 90°, because a linear polarization is equivalent to a superposition of the left and right circularly polarized components, which will be diffracted by the spin-up and spin-down sub-gratings shown in Fig. 4.3b, respectively. After diffracting, the relative phase shift between the left and right handed waves is $\pi$, reflecting the half wavelength spatial shift between the two spin sub-gratings. The $\pi$ phase shift between left and right circular components leads to a 90° polarization rotation when reexpressed in the linear polarization basis.

## Phase modulation

The output voltage of the Si detector is proportional to the total intensity

$$|E_t + E_d(q,t)|^2 = |E_t|^2 + 2\Re\left\{E_t E_d^*(q,t)\exp[-i\phi(q,t)]\right\} + |E_d(q,t)|^2, \tag{4.3}$$

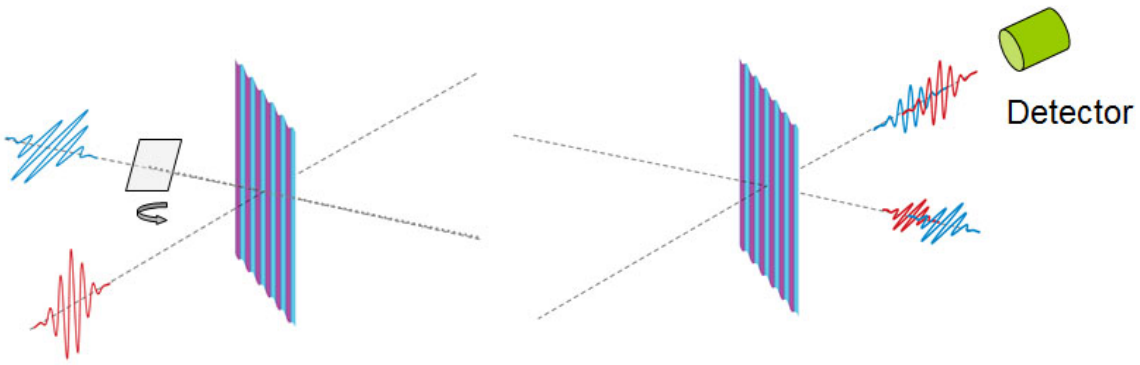


(a) (b)

Figure 4.5: (a) Two orthogonally polarized probe beams in the transient spin grating measurement. (b) After incidence on the grating, some of the probe is transmitted, some is diffracted. The diffracted beam from one probe propagates colinearly with the transmitted beam from the other probe. The polarization of the diffracted beam also rotates by 90°.

where $E_{t/d}$ is the electric field of the transmitted/diffracted light, $|E_d|$ is proportional to the amplitude of the transient grating, $A(q,t)$, and $\phi = \phi_{pld} + \phi_E$, where $\phi_{pld} = kd$ reflects the path length difference $d$ between the LO and diffracted beams, and $\phi_E = \boldsymbol{q} \cdot \delta\boldsymbol{r}$, where $\boldsymbol{q}$ and $\delta\boldsymbol{r}$ are the grating wave vector and position, respectively. For uniform motion with velocity $\boldsymbol{v}$ parallel to $\boldsymbol{q}$, $\phi_E = qv(E)t$. The linear advance of phase with time is equivalent to a Doppler shift of frequency, $\Delta\omega = qv$, as illustrated in Fig. 4.6.

To measure $A(q,t)$ and $\phi_E(q,t)$ separately, we combine heterodyne detection with two phase-modulation schemes. To obtain $A(q,t)$ we modulate $\phi_{pld}$ by oscillating the angle of a coverslip placed in the LO beam path shown in Fig. 4.5a. The coverslip is mounted on a torsional oscillator. To obtain $\phi_E(q,t)$ we oscillate the in-plane $E$ field. In both cases, the phase can be written as

$$\phi = \phi_0 - \frac{\pi}{2} + \phi_1 \cos(\omega_m t_m), \tag{4.4}$$

where $\omega_m$ is the oscillation frequency, and $t_m$ is the time (different from the time delay $t$), the offset $\phi_0$ is tunable by changing the angle of the coverslip, $-\frac{\pi}{2}$ is added here for convenience, and $\phi_1$ is proportional to the amplitude of the driving voltage.

We measure the photocurrent with two lock-in amplifiers: the first one is synchronized to the frequency of the pump intensity modulation at 100 kHz; the second is synchronized to the frequency of the diffracted probe phase modulation at 210 Hz. The first term in Eq. 4.3 is removed by the lock-in amplifier and the last term is too small ($|E_d| \sim 10^{-4}|E_t|$) to detect. Using the identity

$$\exp(iz\cos\theta) = J_0(z) + 2\sum_{n=1}^{\infty} i^n J_n(z)\cos(n\theta), \tag{4.5}$$

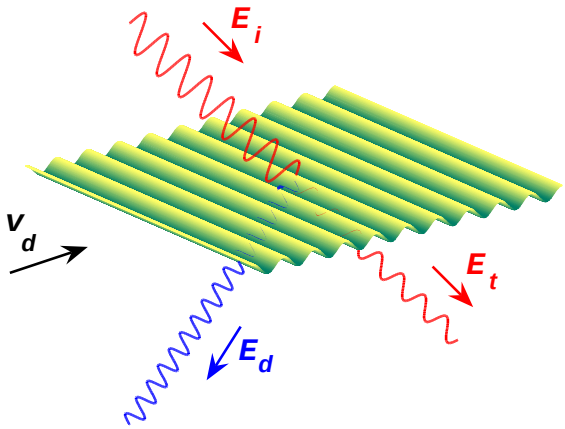


Figure 4.6: Doppler velocimetry. The illustration depicts a transient grating moving with velocity $\boldsymbol{v}_d$ parallel to its wavevector $\boldsymbol{q}$. A probing light field $E_i(\omega)$ is incident on the grating. Upon interaction with the moving grating the probe is divided between a transmitted beam at the same optical frequency $E_t(\omega)$, and a Doppler shifted diffracted beam, $E_i(\omega + \boldsymbol{q} \cdot \boldsymbol{v}_d t)$. From measurements of the Doppler shift we obtain the grating drift velocity $v_d$.

we obtain the first harmonic of $\cos[\phi_0 - \frac{\pi}{2} + \phi_1 \cos(\omega_m t_m)]$, which is given by $2J_1(\phi_1)\cos\phi_0$. The signal at fixed time delay is a Bessel function as we vary the oscillation amplitude $\phi_1$. When $\phi_1 \ll 1$, $J_1(\phi_1) = \phi_1/2$. We tune $\phi_0$ to be 0 to get the maximum signal.

## Phase calibration

It is very tricky to get the absolute value of the phase change due to the drift of the grating. We need to calibrate the $E$ field phase with respect to the coverslip phase as follows. First, in the coverslip phase-modulation scheme, at a fixed time delay ($\sim 10$ ps after $t_0$), measure the TG signal as a function of the driving voltage $V_p$ of the torsional oscillator. Figure 4.7a demonstrates that the signal can be well described by $J_1(V_p/0.108)$.

The coverslip phase can also be calibrated in the following way. Take the signal from the first lock-in amplifier into an oscilloscope. The signal on the oscilloscope is described by

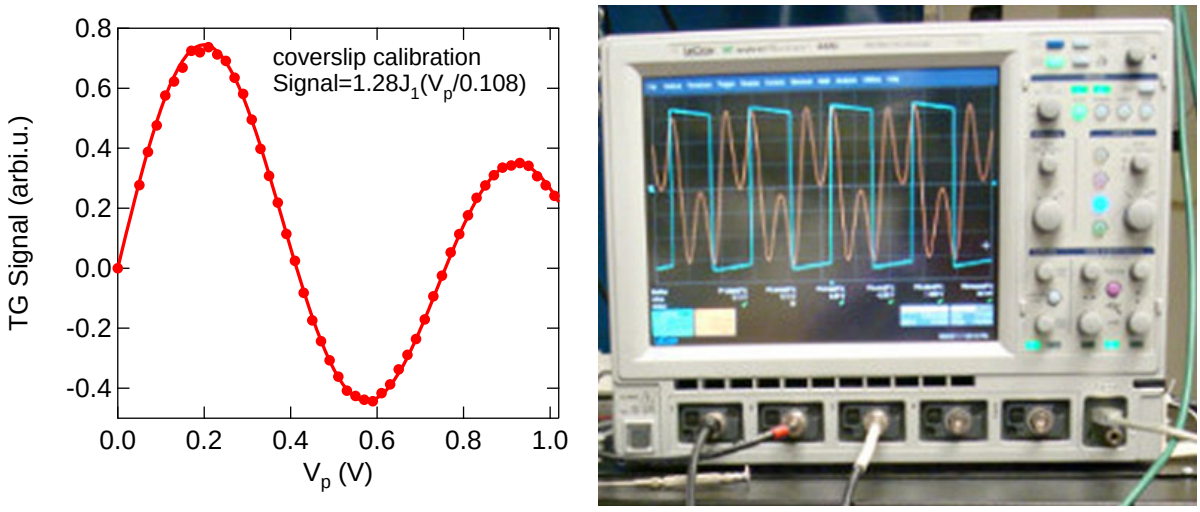


(a) (b)

Figure 4.7: Coverslip phase calibration. (a) TG signal as a function of the driving voltage $V_p$ of the torsional oscillator. (b) TG signal on the oscilloscope, the orange line is the signal, and the blue line is the trigger synchronized to the frequency of the torsional oscillator.

$\cos[\phi_0 - \frac{\pi}{2} + \phi_1 \cos(\omega_m t_m)]$. Tune $\phi_0 = 0$. Vary $V_p$ until the signal looks like what is shown in Fig. 4.7b, corresponding to $\phi_1 = \pi$. In our system, we find $V_p = 0.34$ V, which agrees with the relation $\phi_1 = V_p/0.108$. In these two ways, we calibrate the reference phase.

Then tune $V_p \sim 0.2$ V so that $J_1(V_p/0.108)$ is close to the first maximum and measure the grating signal as a function of the time delay $t$. The signal

$$S_C \propto |E_t| A(q,t) J_1(V_p/0.108), \tag{4.6}$$

In Fig. 4.8a, the red curve shows the amplitude decay of an $e$-$h$ grating.

After that scan, turn off the coverslip oscillation and turn on the in-plane $E$ field. For the in-plane $E$ field modulation, there is an undesired signal due the electro-optic effect. To get rid of this background, we take two scans with the same $E$ field modulation: one scan with 4 laser beams as usual; the other with 3 beams by blocking the diffracted probe. Then subtract the two scans to get the grating shifting signal

$$S_E \propto |E_t| A(q,t) \frac{qv(E)t}{2}. \tag{4.7}$$

We expected to see the signal rises first and then decays as we did shown as the blue curve in Fig. 4.8a. The ratio of Eqs. 4.7 and 4.8 gives $\frac{S_E}{S_C} = \frac{qv(E)t}{2J_1(V_p/0.108)} = \frac{\phi_E}{2J_1(V_p/0.108)}$ without any unknown proportional factor. To get the correct $\phi_E$, we need to carefully record the settings of all the devices, such as lock-in sensitivity and phase. From these two schemes

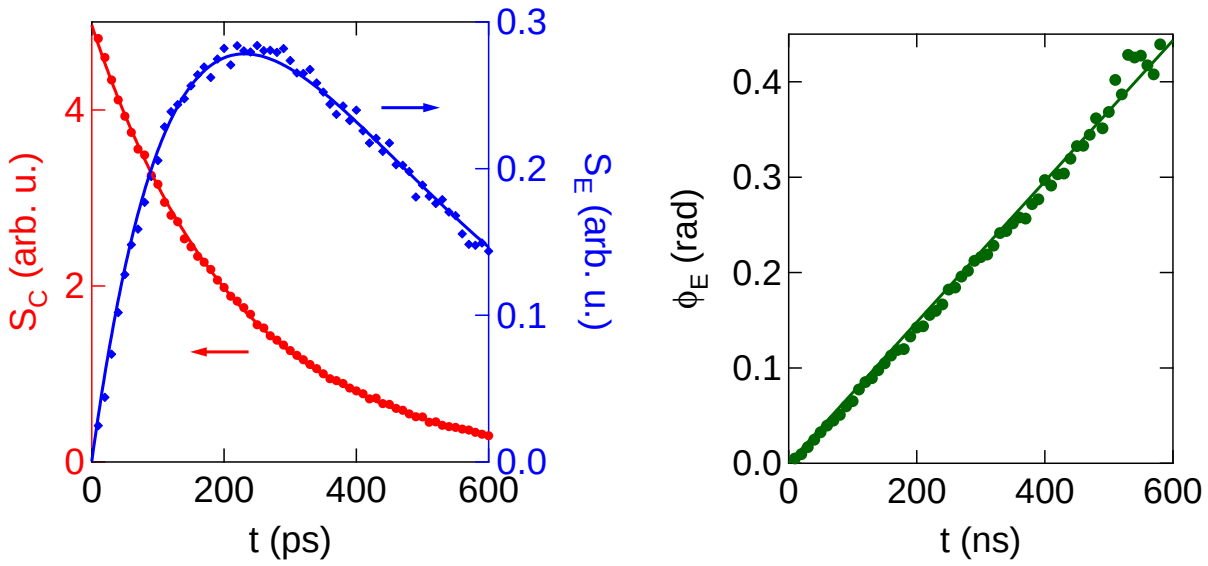


(a) (b)

Figure 4.8: (a) The raw data for the two phase modulation schemes in the case of an $e$-$h$ grating. (b) The ratio of the two measurements gives the phase of the density wave subjected to an applied $E$ field.

we extract $A(q,t)$ (Fig. 4.8a) and $\phi_E = qv(E)t$ (Fig. 4.8b) independently. The phase noise level of 0.01 rad in our detection system corresponds to an uncertainty in velocity of $\sim 10$ m/s, which is approximately 4 orders of magnitude smaller than the Fermi velocity $v_F$.

In Chapter 5 and 6, we describe our measurements of the propagation of charge/spin density in the low field regime, where the grating only moves a small friction of its wavelength during the time of the experiment, i.e., $qv(E)t \ll 1$. In Chapter 7, we study the coherent propagation of spin helices in the high field regime. The in-plane fields are $10-100$ times larger so that the transient grating moves several fringes before it decays away. In that case, $\phi_E$ is large enough to detect without the in-plane $E$ field modulation. Instead, we apply a DC field and modulate the coverslip phase. Then the phase $\phi = \phi_0 - \frac{\pi}{2} + qv(E)t + \phi_1 \cos(\omega_m t_m)$. Following the same analysis, the output of the lock-in amplifier is given by

$$S_{CE} \propto |E_1| A(q,t) J_1(V_p/0.108) \cos[\phi_0 + qv(E)t]. \tag{4.8}$$

The experiment is easier as there is no electro-optical effect.

# Chapter 5

# Measurement of ambipolar dynamics and electron-hole friction

## 5.1 Introduction

The motion of electrons and holes is crucial to the operation of virtually all semiconductor devices and is a central topic of the classic semiconductor texts [44, 45]. In particular, the coupled motion of electron-hole ($e$-$h$) packets in applied electric fields, known as ambipolar transport, is discussed in depth. However, it has been known for some time, although not perhaps widely appreciated, that the motion of $e$-$h$ packets in the high-mobility electron gases found in semiconductor quantum wells and heterojunctions violates the predictions of the standard theory. Insufficient understanding of ambipolar dynamics poses a problem for the development of a spin-based electronics, as many prospective devices are based on spin currents carried by spin polarized $e$-$h$ packets subjected to electric fields [7, 46, 47].

In the standard textbook description of ambipolar transport in a doped semiconductor, electrons and holes interact only through the long-range Coulomb interaction. Momentum relaxation occurs by scattering on impurities and phonons and there is no exchange of momentum between electrons and holes. On the basis of these assumptions it is predicted that in an n-type semiconductor, for example, an $e$-$h$ packet drifts in the direction of the force on the holes, opposite to the motion of the Fermi sea of electrons. However, by photoluminescence imaging, Höpfel *et al.* discovered that in GaAs quantum wells a drifting $e$-$h$ packet moves in the direction of the majority, rather than minority carrier, an effect they termed "negative ambipolar mobility" [48]. They recognized that this effect originates from the scattering between electrons and holes, neglected in the standard versions of ambipolar transport.

The scattering that dominates ambipolar transport in a single quantum well is precisely analogous to the Coulomb drag effect that has been studied intensively in systems in which layers of electron gases are in close proximity [49–51]. In such systems, the strength of the Coulomb interaction between layers can be determined with precision via the transresis-

tance, which is the ratio of the voltage induced in one layer to a current in the other. The transresistance is a direct measure of the rate of momentum exchange (or frictional force) between the two coupled electronic systems. Unfortunately, this technique cannot be used to probe the much stronger frictional force between electrons and holes in the same layer, which plays a crucial role in ambipolar dynamics.

In the experiments reported here we perform the first complete characterization of coupled *e-h* transport in a two-dimensional electron gas (2DEG) by measuring simultaneously the ambipolar diffusion coefficient $D_a$ and the ambipolar mobility $\mu_a$. From these measured coefficients, and a simple model of momentum exchange between the Fermi sea and the packet, we obtain the effective drag resistance $\rho_{eh}$ between electrons and holes in a single quantum well. We show that the value of $\rho_{eh}$ for a single layer, although orders of magnitude larger the transresistance of bilayers, can be quantitatively understood using the same random-phase approximation (RPA) model that describes coupled quantum wells. Based on these findings, it becomes possible to predict the ambipolar transport coefficients for high-mobility semiconductors as a function of carrier density and temperature.

## 5.2 Amplitude and phase revolution of *e-h* grating

Our measurements of *e-h* transport are performed using transient grating spectroscopy [38], which is a contact-free technique based on time-resolved optics. The ambipolar diffusion coefficient can be readily determined by measuring the rate at which the grating amplitude decays as a function of its wavelength. However, as we discuss below, characterization of $\rho_{eh}$ requires that $\mu_a$ must also be measured under the same experimental conditions. The latter is the coefficient that relates the drift velocity of the *e-h* density wave to the magnitude of an electric field $E$ applied in the plane of the 2DEG. Measurement of $\mu_a$ clearly requires sensitivity to the position of the *e-h* density wave - information that is contained in the *phase shift* of the diffracted light. On the other hand, conventional scattering experiments measure light intensity, and thus phase information is lost. In the experiments reported here, we demonstrate that time-resolved detection of both *amplitude and phase* of light diffracted from a drifting *e-h* density wave allows simultaneous determination $\mu_a$ and $D_a$, which together yield the transresistance of the coupled *e-h* system.

In Fig. 5.1a we show the grating amplitude at a representative temperature of 50 K as a function of time after photogeneration, plotted on semilog axes, for several values of the grating wave vector. The decay of $A(q,t)$ is a single exponential with a rate constant, $\gamma$, that increases with increasing wave vector. As shown in the inset, $\gamma$ varies with $q$ as expected for the combined effects of diffusion and electron-hole recombination, $\gamma(q) = 1/\tau_{rec} + D_a q^2$, where $\tau_{rec}$ is the electron-hole recombination time.

In Fig. 5.1b we plot the phase of the *e-h* density wave, $\phi_E(q,t)$ versus $t$ for different values of $q$ at 50 K at full laser intensity $I_0 \simeq 0.25\mu\text{J}-\text{cm}^{-2}$ per pulse. The linear dependence of $\phi_E(q,t)$ on both $t$ and $q$ (see inset) is consistent with the Doppler shift $\phi_E(q,t) = v(E)qt$. The sign of the phase shift gives the direction of motion under the influence of the electric

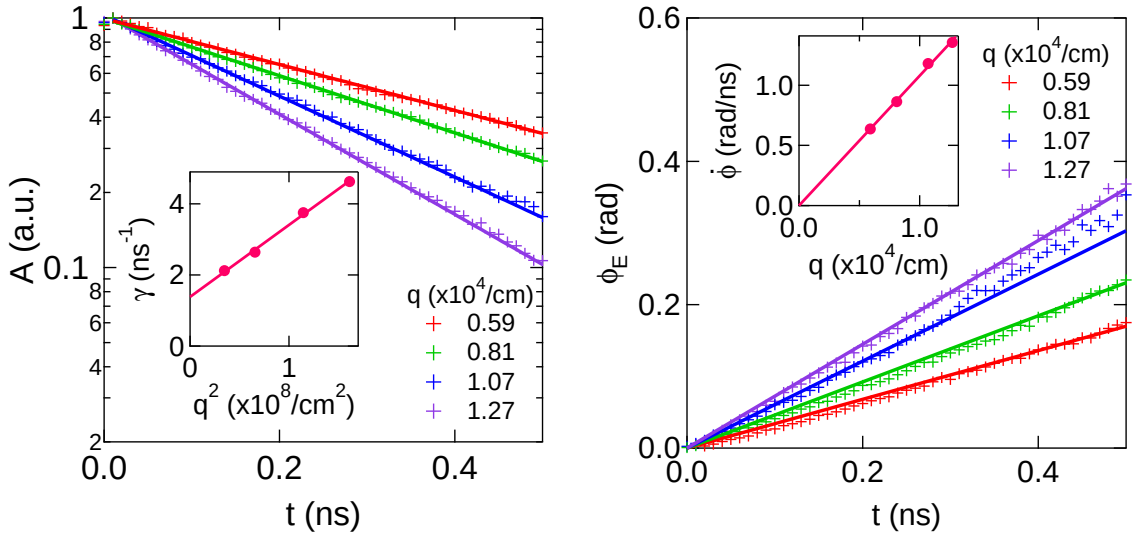


(a) (b)

Figure 5.1: (a) Relative amplitude of $e$-$h$ density wave as function of time for several values of the wave vector $q$ measured at 50 K. Inset: The decay rate $\gamma$ of the amplitude, plotted as a function of $q^2$; the slope of the solid line through the data points is the ambipolar diffusion coefficient $D_a$, and the intercept is the inverse of the $e$-$h$ recombination time $\tau_{rec}$. (b) Linear advance of the phase of the $e$-$h$ density wave with time for several values of $q$, at 50 K. The applied electric field is $E \approx 2$V/cm. Inset: The rate of phase change $\dot{\phi}$ as a function of $q$.

field, which we determine to be the same as that of the electron Fermi sea. From $\partial\phi_E(q,t)/\partial q$ at fixed time delay we obtain the drift velocity of the $e$-$h$ density wave. Normalizing by the applied electric field yields the ambipolar mobility $\mu_a$.

## 5.3 Density dependence of the ambipolar transport

In the course of the measurements we discovered that $\mu_a$ depends strongly on $I$, in addition to the expected dependence on temperature $T$. Figure 5.2a shows $\mu_a$ determined using the analysis outlined above as a function of $T$, for three different values $I$. For comparison, we also plot the electron mobility $\mu_e$, as determined from standard four-contact dc transport measurement. As is clear from Fig. 5.2a, $\mu_a$ decreases when either $T$ or $I$ increases. When nonequilibrium laser experiments show such dependencies, there can be ambiguity as to whether the dependence on $I$ reflects an intrinsic dependence on the photogenerated carrier density, $\Delta n$, or the effect of transient local heating of the electron gas. To determine whether the $I$ dependence is intrinsic, we performed TGS measurements on a device with semitransparent gate electrodes, which allowed us to vary the equilibrium electron density $n_0$ at fixed $\Delta n$.

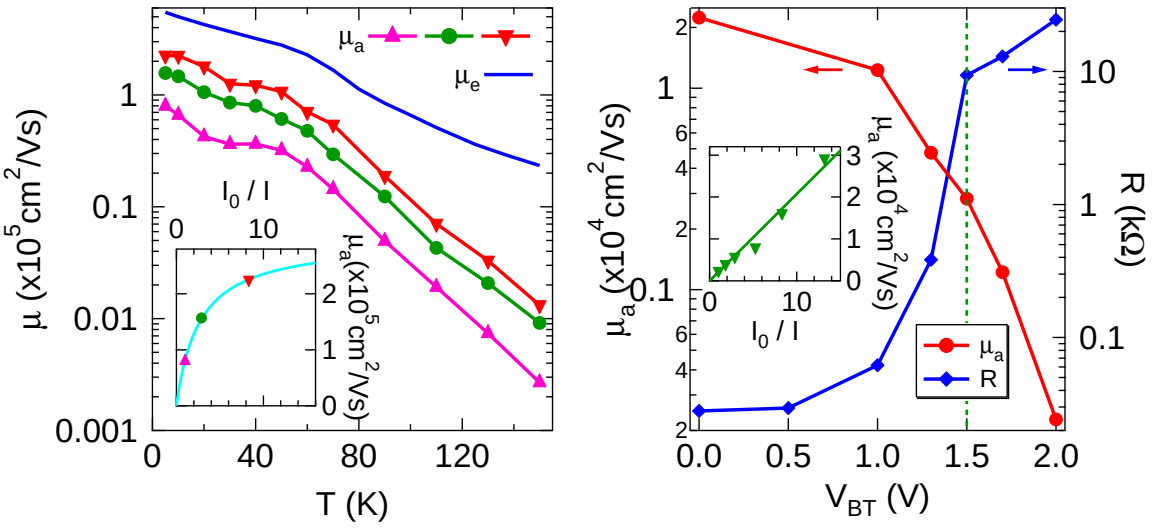


(a) (b)

Figure 5.2: (a) Ambipolar mobility $\mu_a$ at three different pump intensities compared with electron mobility $\mu_e$, as a function of $T$. Inset: $\mu_a$ as a function of laser intensity at 5 K, the solid line is a fit (see text). (b) Ambipolar mobility $\mu_a$ and sample resistance $R$ as a function of gate voltage $V_{BT}$ at 50 K. Inset: $\mu_a$ as a function of laser intensity at fixed gate bias $V_{BT}$=1.5V at 50 K; solid line is a linear fit showing that $\mu_a \propto 1/I$.

In Fig. 5.2b we plot $\mu_a$ and the 2DEG resistance $R$ at 50 K, as a function of the voltage between the two gates, $V_{BT}$. Clearly $\mu_a$ decreases rapidly as $n_0$ is driven to zero (and $R \to \infty$) by increasingly positive $V_{BT}$. As these measurements are performed at constant $I$, it is evident that the intensity dependence shown in Fig. 5.2a reflects an intrinsic dependence of $\mu_a$ on the ratio $\Delta n/n_0$, rather than laser-induced heating. The inset of Fig. 5.2b illustrates that $\mu_a$ scales as $1/I$ (equivalent to $1/\Delta n$) in the regime where $n_0$ is small, while the Fig. 5.2a inset shows that $\mu_a$ approaches an asymptotic value $\mu_{a0}$ in the limit that $I$ (and $\Delta n$) $\to 0$. The overall dependence of variation of $\mu_a$ can be summarized by the simple formula

$$\mu_a(I) = \frac{\mu_{a0}}{1 + \alpha(\Delta n/n_0)}, \tag{5.1}$$

where $\alpha$ is a $T$-dependent parameter.

At this point, we can summarize our experimental findings as follows: (1) The photogenerated $e$-$h$ packet drifts under the influence of an $E$ field in the same direction as the Fermi sea of electrons, (2) the velocity of the packet goes to zero as $\Delta n/n_0 \to \infty$ and approaches a constant in the limit that $\Delta n/n_0 \to 0$, (3) the asymptotic value, $\mu_{a0}(T)$ [Fig. 5.3a], is proportional to, but slightly smaller than, the electron mobility for $T < 80$ K, but becomes much smaller than $\mu_e$ for $T > 80$ K. We show below that each of these observations can

be understood with a relatively simple model that treats the *e-h* packet as a neutral gas of particles that can exchange momentum with the Fermi sea.

## 5.4 Model and *e-h* transresistance

The stationary transport equations for free electrons and the packet can be written as

$$\begin{aligned} \frac{n_0 m_e v_e}{\tau_e} + n_0 \Delta n \gamma (v_e - v_p) &= -n_0 e E, \\ \frac{\Delta n m_p v_p}{\tau_p} + n_0 \Delta n \gamma (v_p - v_e) + k_B T \nabla(\Delta n) &= 0, \end{aligned} \tag{5.2}$$

where $1/\tau_{e(p)}$ is the rate at which electrons(packet) lose momentum to the lattice, $m_e$ and $m_p$ are respective masses, and $\gamma$ is a parameter describing the rate of momentum exchange. By solving these equations we obtain precisely the form of Eq. 5.1, where

$$\mu_{a0} = -\frac{\mu_e}{1 + \frac{\mu_e}{\mu_p}\frac{\rho_e}{\rho_{eh}}}, \tag{5.3}$$

and $\alpha = \mu_{a0}/\mu_p$. In Eq. 5.3 we have made use of the definitions, $\mu_p \equiv e\tau_p/m_p$, $\rho_e \equiv (n_0 e \mu_e)^{-1}$, and $\gamma \equiv e^2 \rho_{eh}$. The negative sign of $\mu_a$ corresponds to the *e-h* packet drifting in the same direction as the Fermi sea of electrons. In addition, we find that solving for the ambipolar diffusion coefficient yields

$$D_a = \frac{k_B T \mu_{a0}}{e}\frac{\rho_e}{\rho_{eh}}. \tag{5.4}$$

From Eq. 5.4 we see that independent measurement of $\mu_{a0}$, $D_a$, and $\rho_e$ directly yields the electron-hole transresistance, $\rho_{eh}$. The values of $\rho_{eh}$ thus determined are plotted versus $T$ in Fig. 5.3b, together with $\rho_e$ for comparison. We see that in the low $T$ regime, $\rho_e \ll \rho_{eh}$, which translates to an ambipolar mobility that is not too different from the electron mobility. As $T$ increases and $\rho_e$ approaches $\rho_{eh}$, $\mu_{a0}$ tends towards the much smaller $\mu_p$. While the values of ambipolar mobility are controlled by $\rho_e/\rho_{eh}$, $D_a$ itself is fairly insensitive to Coulomb drag because diffusive spreading of the packet takes place with parallel transport of electrons and holes. This effect is illustrated in the inset of Fig. 5.3b, which compares the ratio $D_a/\mu_p$ to $k_B T/e$. The near agreement with the Einstein relation shows that $D_a$ is essentially determined by the nondegenerate gas of holes because the electrons in the packet are tethered to them through the long-range Coulomb interaction.

Recently, Shen and Vignale extend our theoretical analysis to include the possibility of a crossover between the normal regime with positive mobility to the anomalous regime with negative mobility [52]. At the crossover point the mobility is zero and the grating remains stationary. They have discussed various possibilities for observing this crossover. They also make a careful comparison with your experimental data and find good agreement.

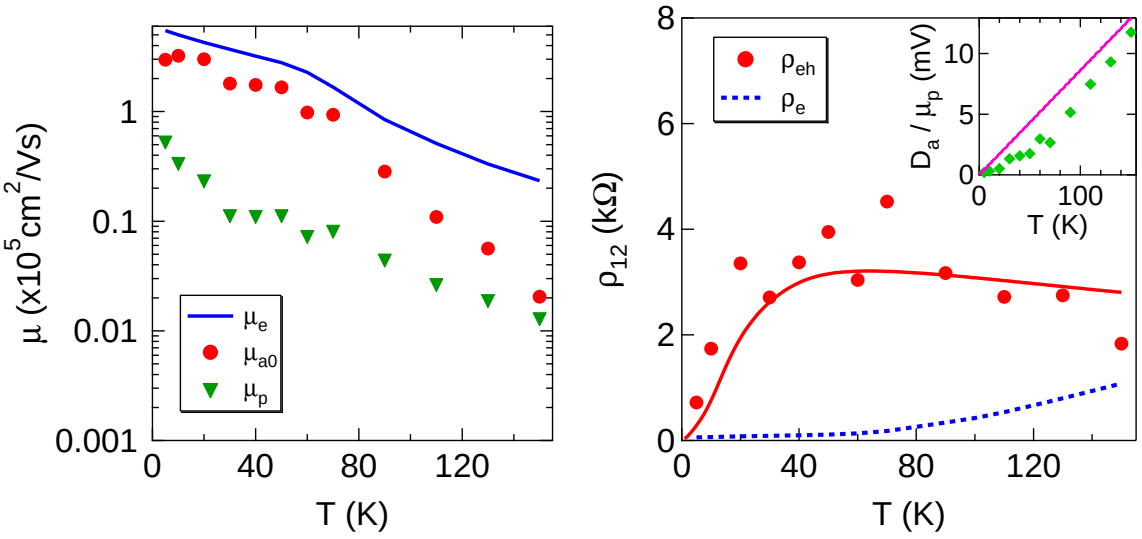


(a) (b)

Figure 5.3: (a) Comparison of electron mobility $\mu_e$; ambipolar mobility $\mu_{a0}$, and packet mobility $\mu_p$, as a function of $T$. (b) The $e$-$h$ drag transresistivity $\rho_{eh}$ as a function of $T$; solid line is a theoretical prediction of $\rho_{eh}$ based on the RPA. Inset: $D_a/\mu_p$ compared with the Einstein relation prediction in the non-degenerate regime $k_BT/e$.

## 5.5 RPA calculation

The values of $\rho_{eh}(T)$ that we obtain are several orders of magnitude larger than those obtained in Coulomb drag experiments on coupled quantum wells [53, 54]. However, in the experiments reported here $(i)$ electrons and holes are confined to the same quantum well and $(ii)$ one of the Fermi gases (the holes) is nondegenerate throughout the $T$ range of the experiment. To test whether the values of $\rho_{eh}(T)$ shown in Fig. 5.3b are reasonable, we apply the standard RPA model for Coulomb drag to the single layer case. The RPA expression for $\rho_{eh}(T)$ is the phase space integral of the product of the interaction, $V_{\rm RPA}(q)$, and $\Im\{\chi_{1,2}\}$, the imaginary part of the susceptibility of fermion species 1 and 2, respectively [55–57]. To apply this theory to our experiment, we substitute the nondegenerate Lindhard response for the hole susceptibility [58], leading to,

$$\rho_{eh}(T) = \frac{\hbar}{2n_e a_B^2 e^2}\sqrt{\frac{m_h}{\pi m_e}}\int_0^\infty dq \frac{q\exp(-q^2l_T^2/16)}{(q+q_{TF})^2} \times \int_0^\infty d\tilde{\omega}\frac{[\mathfrak{F}_{-1/2}(\eta_-)-\mathfrak{F}_{-1/2}(\eta_+)]\exp(-\tilde{\omega}^2/q^2l_T^2)}{\sinh(\tilde{\omega}/2)}, \tag{5.5}$$

where $q_{TF} = 2/a_B^*$ is the Thomas-Fermi screening wave vector, $l_T^2 \equiv 2\hbar^2/m_h k_B T$ is the square of the thermal wavelength of the holes, $\tilde{\omega} \equiv \beta\hbar\omega$, $\eta_\pm = \ln\left[\exp\left(\frac{T_F}{T}\right) - 1\right] - \frac{T_F}{T}\nu_\pm^2$, $\nu_\pm = \frac{\omega}{qv_F} \pm \frac{q}{2k_F}$, and $\mathfrak{F}_{-1/2}(\eta) \equiv \int_0^\infty t^{-1/2}dt/[1 + \exp(t - \eta)]$ is the Fermi-Dirac integral of order $-\frac{1}{2}$. See Appendix B for the derivation and discussion of the transresistivity. Numerical evaluation of the phase space integral, plotted as a solid line in Fig. 5.3b, shows that the RPA interaction describes the experimental data quite well without any free parameters.

In conclusion, we have used phase-resolved TGS to simultaneously measure the ambipolar drift and diffusion of photoinjected electrons and holes. From these measurements we determine for the first time the frictional force between a degenerate Fermi liquid of electrons and a dilute gas of holes in the same two-dimensional system. The measured values of $\rho_{eh}$ data are accurately described by the static limit of RPA-based theory with no free parameters. By combining $\rho_{eh}$ with a simple model based on conservation of momentum, the ambipolar dynamics of high-mobility electron gases can be predicted, enabling more powerful modeling of devices, for example those based on spin current of drifting polarized carriers.

# Chapter 6

# Doppler velocimetry of spin propagation

## 6.1 Introduction

The transistor, the iconic invention of 20th century science, is a semiconductor device in which the flow of electrons is modulated by voltages applied via electrodes known appropriately as gates. In a conventional transistor the gate electrode controls the number of mobile electrons in the current carrying pathway, or "channel." In pursuit of transistors with faster response and lower rates of energy dissipation, there has been intense investigation aimed at modulating current through manipulation of spin by applied electric fields [6, 46], a coupling that occurs because of the spin-orbit (SO) interaction. Recently, gate-controlled modulation of current via SO coupling has been demonstrated in prototype device structures that operate below room temperature [59, 60].

Further progress towards spintronic logic requires a deeper understanding of the basic physical principles upon which such devices are based. Essentially the question is this: how far, and how fast, can spin polarization propagate in a current-carrying electron gas? This question was first addressed in pioneering work that used magneto-optic imaging to follow the drift of spin polarization packets in real space [61]. These experiments were enabled by the enhanced spin lifetimes (in excess of 10 ns) that arise near the metal-insulator transition of a doped semiconductor at the expense of electron mobility, $\mu_e$. However, the high $\mu_e$ electron gas needed for fast devices is in a very different dynamical regime, where spin lifetimes are $\sim 10 - 100$ ps, during which time spin may propagate only $10 - 100$ nm (depending on the temperature, $T$, and applied field, $E$). To resolve spin propagation on picosecond time and nanometer length scales we have developed a technique to measure velocity via the Doppler shift of light scattered from propagating waves of spin density. Our method extends TGS [38], which has traditionally been used to measure rates of diffusion, to the measurement of drift velocity.

In the experiments reported here we photo-inject the SDW into a 2DEG subject to an in-

plane $E$ field that is parallel to the grating wave vector and measure the resulting propagation of spin polarization. If the polarization wave undergoes normal drift and diffusion, the spin density will evolve according to $S(x,t) = S_0 \exp[-t/\tau(q)] \cos q[x - x_0(t)]$, where $q\hat{\boldsymbol{x}}$ is the wave vector and $x_0(t)$ is the displacement. Measurement of the amplitude of a diffracted pulse yields the wave vector dependent lifetime $\tau(q)$, from which the spin memory time and diffusion coefficient can be determined. Information about $x_0(t)$ is contained in the phase, rather than the amplitude, of the diffracted light. For example, light diffracted from an SDW drifting at constant velocity, $x_0(t) = v_d t$, will contain the optical phase factor $\phi(t) = q v_d t$. The linear advance of phase with time is equivalent to a Doppler shift, $\Delta\omega = v_d q$.

## 6.2 Spin diffusion

Shown in Fig. 6.1a is $A(q,t)$, the amplitude of the probe diffracted from a photoinjected SDW with wavevector parallel to the [110] crystal axis, as measured at $T = 30$ K. The time dependence of the amplitude is the sum of two exponentially decaying components, $A(q,t) = A_+ \exp[-t/\tau_+(q)] + A_- \exp[-t/\tau_-(q)]$, with nearly equal weighting factors ($A_+ \approx A_-$). The two lifetimes, $\tau_\pm(q)$, are plotted as a function of $q$ in Fig. 6.1b. The decay rate of the shorter-lived component $1/\tau_+(q)$ is proportional to $q^2$ as expected for a simple diffusive process. However, the q-dependence of $1/\tau_-(q)$ is anomalous, with a minimum rate found at a nonzero wavevector, $q_0 \approx 0.6 \times 10^4$ cm$^{-1}$.

The existence of two rates is a consequence of SO coupling, which in a GaAs QW has the form of an effective magnetic field that induces spin precession at a rate that depends on the electron's momentum, $\boldsymbol{p}$. In a symmetric QW the Dresselhaus SO coupling [15] dominates, which is characterized by the precession rate vector field, $\boldsymbol{\Omega}(\boldsymbol{p}) = 2\hbar^{-2}\beta_1(\boldsymbol{p}_y\hat{\boldsymbol{x}} + \boldsymbol{p}_x\hat{\boldsymbol{y}})$, where $\beta_1$ is the linear Dresselhaus coupling strength and $\hat{\boldsymbol{x}}$ and $\hat{\boldsymbol{y}}$ are the [110] and [1$\bar{1}$0] crystal axes, respectively. The connection between the precession vector and momentum induces a strong correlation between the diffusion of electrons in real space and of the orientation of their spins on the Bloch sphere. Theoretical analysis of this correlation yields a pair of normal modes at each $q$ that are helical waves of spin density with opposite sense of rotation [16–18, 20, 21, 62]. The lifetime of the helix whose sense of rotation matches that of the electron's precession is strongly enhanced by SO coupling while the lifetime of the helix with opposite rotation is reduced. Both lifetimes, $\tau_\pm(q)$, are observed in the TSG experiment because the photogenerated initial state - a wave of pure $S_z$ - is a superposition of the two helices of opposite pitch. The solid lines through the data in Fig. 6.1b are fits to the spin helix theory [17, 18, 20] with $\beta_1 = 3.4 \times 10^{-3}$ eVÅ.

From analysis of the measured $\tau_\pm(q)$ we also obtain the spin diffusion coefficient, $D_s(T)$, plotted in Fig. 6.1c. For comparison we plot the electron diffusion coefficient $D_e(T)$ obtained by applying the Einstein relation to the electron transport mobility $\mu_e$. $D_s(T)$ is smaller than $D_e(T)$ as a result of spin Coulomb drag (SCD) [63] , which is a frictional force between oppositely oriented spins that is generated by electron-electron ($e$-$e$) collisions. As spin diffusion requires a counter flow of opposite spin populations, it is damped by SCD,

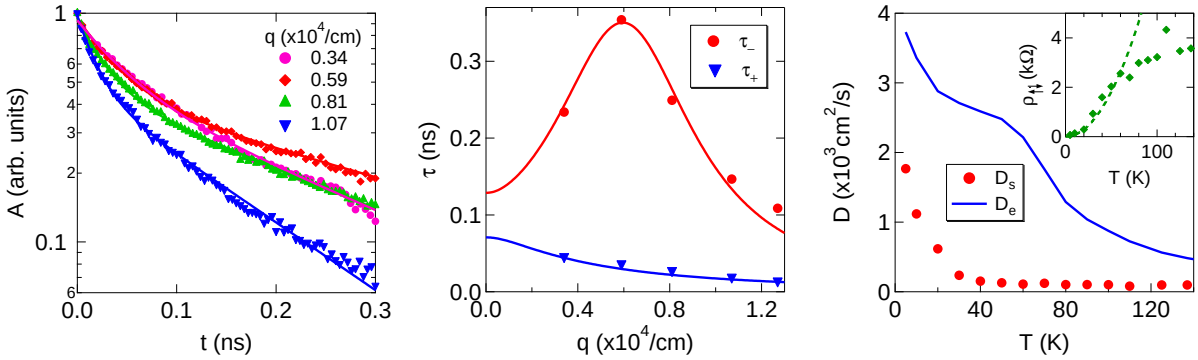


(a) (b) (c)

Figure 6.1: Spin diffusion and spin-Coulomb drag. (a) Decay of the amplitude of transient spin gratings measured at several values of the wave vector $q$. The solid lines are fits to a model of two exponentially decaying helical modes of equal amplitude. (b) Lifetimes $\tau_{\pm}(q)$ for the spin helix modes of opposite pitch obtained from fits to the data in (a). The short-lived mode, $\tau_{+}(q)$, is proportional to $1/q^2$ as expected for diffusion. The lifetime of the long-lived mode, $\tau_{-}(q)$, is peaked at a non-zero q which is commensurate with the inverse spin-precession length in the SO field. (c) Comparison of spin diffusion coefficient $D_s(T)$ determined from TGS with electron diffusion coefficient $D_e(T)$ determined by transport measurements. Inset: spin transresistivity $\rho_{\uparrow\downarrow}(T)$ extracted from ratio of $D_s(T)/D_e(T)$. The dashed line is the RPA prediction for $\rho_{\uparrow\downarrow}(T)$.

whereas charge transport is protected from $e$-$e$ collisions by momentum conservation. The reduction of spin relative to electron diffusion coefficient seen here is considerably larger than in previously reported measurements [40] - $D_s$ is only about 5% of $D_e$ when measured above the Fermi temperature of 80 K. The SCD effect is more pronounced in the cleaner sample studied here because, while its low T resistivity is approximately eight times smaller than the previously studied QW with the same electron density, the intrinsic spin-drag transresistivity $\rho_{\uparrow\downarrow}(T)$ is unchanged. This is evident when we invert the measured $D_e/D_s$ to extract the transresistivity (See Appendix B Sec. B.2). The $\rho_{\uparrow\downarrow}(T)$ thus obtained (plotted in Fig. 6.1c inset) is quantitatively consistent with earlier reports and in excellent agreement with the random phase approximation (RPA) theory of SCD in two-dimensions in the range of $T$ below the Fermi temperature [64, 65].

## 6.3 Spin drift

We turn now to Doppler shift measurements of spin helix drift under the influence of an $E$ field applied parallel to the SDW wave vector. Fig. 6.2a shows the phase, $\phi(q,t)$, of light diffracted from a transient spin grating as a function of $t$ for several values of $q$, measured

at 30 K. For wave vectors larger than $q_0$, the phase increases linearly with time, indicating near uniform drift in the same direction as the Fermi sea of electrons. However, $\phi(q,t)$ is clearly more complex for $q < q_0$. While $\dot{\phi}$ starts out positive, it quickly crosses zero and becomes negative for $t \gtrsim 50$ ps, indicating counter-propagation with respect to the Fermi sea. It is natural to associate the anomalous behavior of the phase with the presence of the two helical modes discussed previously, and to describe the overall $\dot{\phi}(q,t)$ as the weighted average of their individual rates of phase advance, $\dot{\phi}_{\pm}(q)$,

$$\dot{\phi}(q,t) = \frac{A_+ \exp[-t/\tau_+(q)]\dot{\phi}_+(q) + A_- \exp[-t/\tau_-(q)]\dot{\phi}_-(q)}{A_+ \exp[-t/\tau_+(q)] + A_- \exp[-t/\tau_-(q)]}. \tag{6.1}$$

The lines through the data in Fig. 6.2a are fits obtained with this expression, using the values of $\tau_{\pm}(q)$ obtained previously. The high quality of the fits suggests that the complicated behavior of $\dot{\phi}(q,t)$ reflects contributions from the two helices of opposite pitch, each propagating with its own uniform phase velocity. Shown in Fig. 6.2b are values $\dot{\phi}_{\pm}(q)$ obtained using Eq. 6.1 and the solid lines are fits to a theory of spin helix propagation described qualitatively below.

While for a Fermi sea at rest the average of $\mathbf{\Omega}(\boldsymbol{p})$ over occupied states is clearly zero, an electron gas drifting with velocity $v_d\hat{\boldsymbol{x}}$ will experience a nonzero $\langle\mathbf{\Omega}\rangle = 2\beta_1\hbar^{-2}m^*v_d\hat{\boldsymbol{y}}$. Consider first spin helices injected into a drifting Fermi sea in the absence of SO coupling. In this case the angle, $\theta$, of the local spin polarization with respect to $\hat{\boldsymbol{z}}$ would be static in a frame moving with $\boldsymbol{v}_d$, $\theta(x') = \pm qx'$, where $x' = x - v_dt$. However, the nonzero SO coupling will cause the spins to precess as they drift, such that $\theta(x',t) = \pm qx' + \langle\Omega\rangle t$. When viewed in the stationary frame, $\theta(x,t) = \pm qx - v_d(q_0 \pm q)t$, where $q_0 \equiv 2\beta_1\hbar^{-2}m^*$, which corresponds to the two rates of phase advance, $\dot{\phi}_{\pm}(q,t) = v_d(q \pm q_0)$. Thus for example, the long-lived helix will appear to be stationary when $q = q_0$ and counter-propagate for $q < q_0$. The lines through the data points in Fig. 6.2b are the predictions of quantitative theories of helix drift [23, 31], which differ from the qualitative picture outlined above only at very low values of $q$ not accessible in our experiments.

The propagation of spin in the Dresselhaus field can also be visualized in the spatial rather than wave vector domain. As we have shown, TGS measures $S_z(q,t)$ over a broad range of $q$. The Fourier transform of $S_z(q,t)$ yields the real space spin propagator, $S_z(x,t)$, which describes the time evolution of spin polarization following pulsed injection of a narrow stripe of $z-$oriented spin density along the $y-$axis. Fourier transformation of the theoretical fits to the amplitude and phase of $S_z(q,t)$ shown in Figs. 6.1b and 6.2b yield the propagator illustrated in Fig. 6.2c, which has the form of an envelope function that moves with uniform velocity $v_d$ while modulating a stationary SDW (See Refs. [23, 31], Chapter 3 and footnote[1]).

[1]For simplicity, let us first consider the case where the Rashba and the Dresselhaus spin-orbit terms are equal. The dispersion relation for the two normal modes is given by [23, 31], $i\omega_{\pm}(q) = D_s(q \pm q_0)^2 + iv_d(q \pm q_0)$. The time-evolution of the $z-$component of the photoinduced spin density after pulsed photoinjection is given as the equal weighted sum of the two normal modes, $S_z(q,t) = \frac{S_{z0}}{2}[\exp(-i\omega_+t) + \exp(-i\omega_-t)]$, where $S_{z0}$

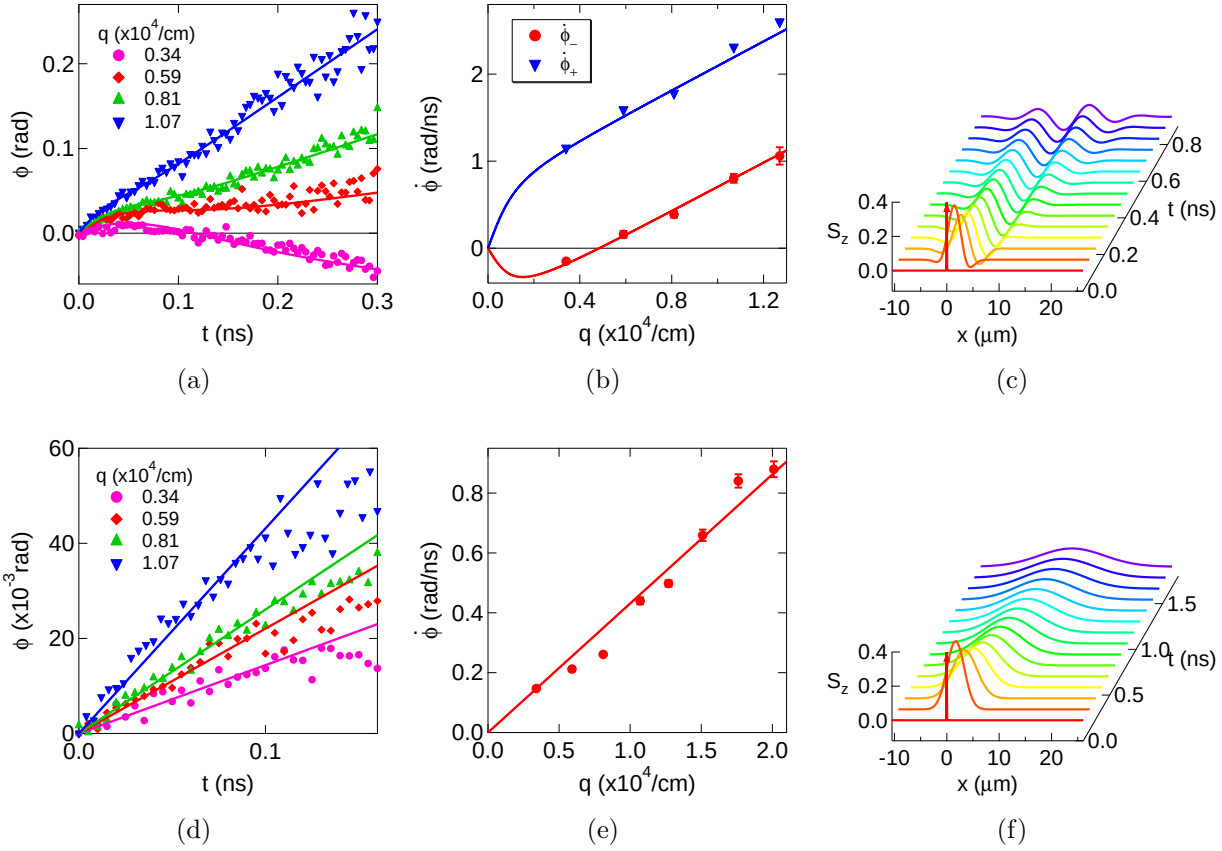


Figure 6.2: Spin drift in different temperature regimes. (a) Spin drift observed by Doppler velocimetry in the presence of an applied electric field ($E = 2$ V/cm) at $T = 30$ K. The quantity $\phi$ is the optical phase shift of the probe beam diffracted from the drifting spin grating. After the short-lived helix has decayed, the slope of $\phi(t)$ is proportional to the velocity of the long-lived helix. The solid lines are a fit to Eq. 6.1 describing two independently propagating spin helix modes. The negative slope of the data at low $q$ demonstrates that the long-lived helix mode moves backwards (relative to the Fermi sea) for $q < q_0$. (b) Wave vector dependence of the phase velocity associated with the two helical modes, $\dot{\phi}_\pm(q)$, obtained from the fits in (a). The solid lines are a fit to the theoretical model of spin propagation in the presence of Dresselhaus SO coupling described in the text. (c) Real-space spin propagator corresponding to the Fourier transform of the fit in (b). The spin propagator, which describes the space-time evolution of spin polarization following $\delta-$function injection, has the form of an envelope function that moves at velocity $v_d$ while modulating a stationary helical SDW. Because this stationary pattern decays exponentially, it is necessary to multiply the propagator by $\exp[t/\tau_-(q_0)]$ in order to visualize the motion at long times. (d) and (e) show the same quantities as in (a) and (b), but measured at 150 K. (f) Spin propagator at 150 K showing that transport takes place without coherent spin precession. Error bars (s.d.) in (b) and (e) represent the uncertainty in the fitting of (a) and (d).

The polarization wave that emerges as the envelope propagates is closely related the stripe-like patterns imaged in steady state measurements on low$-\mu_e$ semiconductors [66].

A surprising feature of our results is that the spin propagation dynamics described above change drastically as $T$ is increased towards room temperature. As shown in Fig. 6.2d and 6.2e, at 150 K the two helices with phase dispersion $\phi_\pm(q,t) = v_d(q \pm q_0)t$ have been replaced by a single mode with $\phi_\pm(q,t) = v_d q t$. The latter corresponds to drift with velocity $v_d$ without spin precession. Fourier transformation of fits to $S_z(q,t)$ at 150 K yields a spin packet that propagates at $v_d$ and does not modulate a polarization wave, as shown in Fig. 6.2f (See footnote[2]). Thus a spin-transistor based on control of SO-induced precession will not operate in this $T$ regime. We note that the clear cross-over in spin dynamics that has taken place can be seen only in spatial or wave vector-resolved measurements, as the lifetime of the uniform spin polarization, $S_z(q=0,t)$ increases monotonically from 30 to 150 K [67].

The absence of spin precession at 150 K cannot be attributed to a change in the SO coupling strength, $\beta_1$, which is an intrinsic property of the GaAs band structure. Instead, our results suggest that the effective precession vector $\langle \mathbf{\Omega} \rangle$ does not survive increased thermal averaging. One possible reason for this is the cubic (in $p$) Dresselhaus coupling, which causes the net precession angle between scattering events to depend on the electron's velocity, and has been shown to degrade the spin-spatial correlations described previously [21, 68].

## 6.4 Temperature dependence of spin mobility

We have seen that, when viewed in the spatial domain, an injected spin packet moves with $v_d = \partial\dot{\phi}/\partial q$, regardless of whether the propagation is accompanied by coherent spin precession. Thus at each $T$ we can determine a spin packet velocity from the dispersion of $\dot{\phi}(q)$, obtain a spin packet mobility, $\mu_s \equiv v_d/E$, and compare with the electron mobility, $\mu_e$ as determined from dc transport. In the course of such measurements we discovered that $\mu_s$ depends strongly on the intensity, $I$, of the laser pulse that generates the spin grating. Fig. 6.3a is a plot of $\mu_s$ as a function of $I$ for various $T$. As $I$ is reduced from its maximum value $I_0 = 0.25$ J/cm$^2$, $\mu_s$ initially increases and then approaches an asymptotic value $\mu_{s0}$ in the limit that $I \to 0$. The curves through the data points are fits to the relation,

---

is the initial amplitude of the SDW. Fourier transformation from the wave vector to spatial domain gives, $G_z(x,t) \propto \int_0^\infty dq \exp(iqx) S_z(q,t) \propto \frac{1}{\sqrt{D_s t}} \exp\left[-\frac{(x-v_d t)^2}{4D_s t}\right] \cos(q_0 x)$. The spin propagator is the product of a Gaussian envelope function and a static spin wave with wave vector $q_0$. If $\alpha \neq \beta_1$, numerical integration gives a similar propagator, but the amplitude decays exponentially [23]. Fig. 6.2c is the Fourier transform of the theoretic fit to the data at 30 K. For demonstration purpose, we multiply the propagator by $\exp[t/\tau_-(q_0)]$ and extend the time to about 1 ns.

[2]If we have the simple dispersion relation, $i\omega(q) = D_s q^2 + 1/\tau_0 + i v_d q$, then $S_z(q,t) = S_{z0}\exp(-i\omega t)$, with the corresponding Fourier transform, $G_z(x,t) \propto \frac{1}{\sqrt{D_s t}} \exp\left[-\frac{(x-v_d t)^2}{4D_s t}\right] \exp(-t/\tau_0)$. In this case there is no helical spin wave underlying the Gaussian packet. Fig. 6.2f is the Fourier transform of the theoretic fit to the data at 150 K. We multiply the propagator by $\exp(t/\tau_0)$.

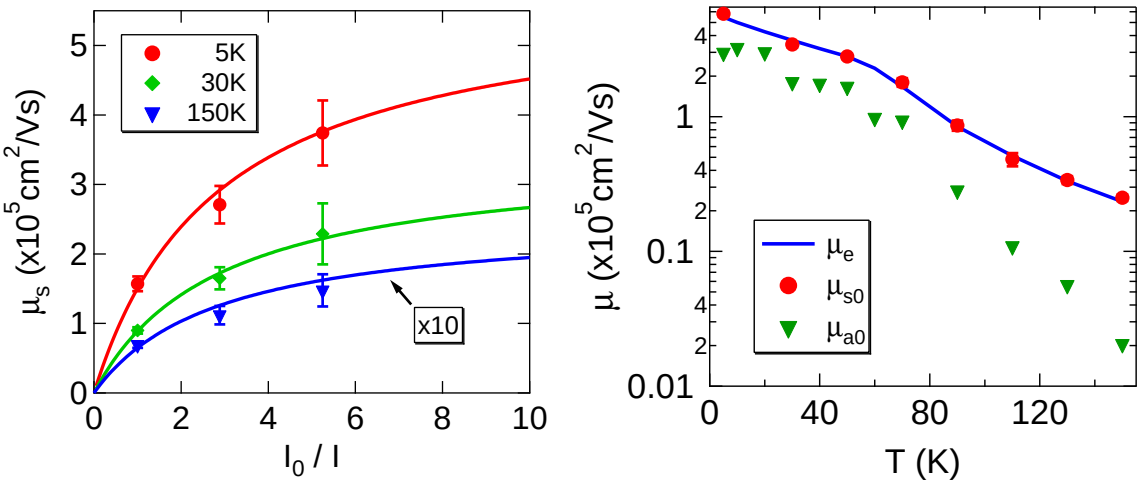


(a) (b)

Figure 6.3: Spin mobility. (a) Spin mobility $\mu_s$ as a function of inverse laser intensity $I_0/I$, where $I_0 = 0.25$ J/cm$^2$, at various $T$. The solid lines are fits as described in the text, from which we determine $\mu_{s0}$, the spin mobility in the limit of zero laser intensity. (b) Electron transport mobility, $\mu_e$, compared with spin and ambipolar mobility in the limit of zero laser intensity ($\mu_{s0}$ and $\mu_{a0}$ respectively). In this limit, the spin mobility is equal to the electron mobility, despite the crossover to coherent precession that takes place as the temperature is lowered.

$\mu_s(I) = \mu_{s0}(T)/(1 + 2.86I/I_0)$. The red circles in Fig. 6.3b represent $\mu_{s0}(T)$ as determined from fits to the intensity dependence. Error bars (s.d.) represent weighted uncertainty carried through several fitting steps as described in the footnote.[3] The plot shows that $\mu_{s0}(T) = \mu_e(T)$ the over the entire $T$ range of the experiment. Furthermore, this equality holds even as the nature of spin propagation crosses over from the precession regime, where $\dot{\phi}_\pm(q) = v_d(q \pm q_0)$, to the incoherent regime, where $\dot{\phi}(q) = v_d q$.

We argue below that the dependence of $\mu_s$ on $I$ indicates that the direct force of the

[3]The error bars in Fig. 6.3 stem from the uncertainty in fitting the Doppler velocimetry data such as that in Fig. 4a and 4d. The uncertainty in these fits (barely visible error bars in Figs. 6.2b and 6.2f) was used to weight subsequent fitting of the phase velocity $\dot{\phi}(q)$, and drift velocity $v_d$. The spin mobility $\mu_s(I,T)$ was obtained through normalization by the applied field. The uncertainty in $\mu_s(I,T)$, which is shown at several temperatures as error bars in Fig. 6.3a, was then used to weight the fits from which we extracted the values of $\mu_{s0}(T)$ shown in Fig 6.3b. The error bars shown in Fig. 6.3b for $\mu_{s0}(T)$ are smaller than the circles for almost all of the data points. Error bars for $\mu_{a0}(T)$ are even smaller and cannot be seen on the plot. Although the mobility decreases with T between 30 and 150 K the relative uncertainty in $\mu_{s0}(T)$ remains essentially the same. This is the case because the measurements were performed while maintaining a constant current by increasing the applied voltage. In all cases the applied fields are small and well inside the linear response regime.

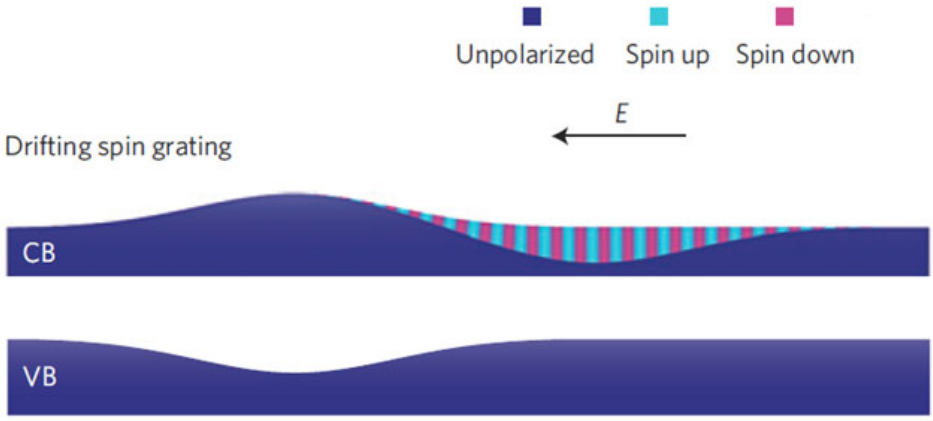


Figure 6.4: Under the influence of an applied E field, the spin grating and the Gaussian e-h packet move in the direction of the Fermi sea of electrons. While the spin grating moves at or near the velocity of the Fermi sea, the e-h packet moves at the much slower ambipolar velocity. This leads to an increasing spatial separation of the spin and charge degrees of freedom. c.f. Fig. 4.2.

electric field on the spin polarization is zero, and that spin waves (or packets) are propelled solely by momentum transfer from the surrounding Fermi sea. The basis of this claim is that the same dependence of mobility on pump intensity is observed when the Fermi sea drives another neutral excitation of the 2DEG, namely packets of *e-h* density [26, 48]. Individual packets of electron and hole density cannot separate in weak applied fields − the constraint of local charge neutrality forces the two charge species drift together at a speed $\mu_a E$, where $\mu_a$ is the ambipolar mobility. Because the driving force of the Fermi sea scales with the equilibrium carrier concentration, $n_0$, while the packet's inertia varies as the photoinduced carrier concentration, $\delta n$, the packet drift velocity depends on the ratio $\delta n/n_0$, which is proportional to $I$. Solving the appropriate force balance equations yields $\mu_a \propto I^{-1}$ in the limit that $\delta n \gg n_0$ and $\mu_a \rightarrow \mu_{a0}$ in the limit $\delta n \ll n_0$, i.e., the same trends that we observe in the spin packet mobility. In Fig. 6.3b we compare $\mu_{a0}(T)$ determined from TGS measurements on the same QW using parallel polarization with the electron and spin mobility. The slower rate of ambipolar propagation reflects the fact that, in contrast with electron spin propagation, the low mobility holes must be dragged along with the drifting electrons.

Overall, the phenomena described above demonstrate that spin density propagates in a Fermi sea as a distinct, neutral degree of freedom that couples to electron motion through various interactions (*e.g.* SO and Coulomb). Fig. 6.4 illustrates the distinct nature of the spin polarization - given sufficient time, the more rapidly drifting SDW will leave the unpolarized packet of *e-h* density in its wake. In the limit that the number of photoexcited carriers is much less than the equilibrium number, we find that spin density propagates at the

drift velocity of the Fermi sea. While this result has been predicted theoretically in models that don't include SO-induced precession [69, 70], it is quite striking that this equality is preserved even as spin dynamics cross over from incoherent relaxation to coherent precession with decreasing $T$.

In conclusion, measuring the Doppler shift of light induced by drifting spin density waves has revealed several surprising aspects of spin propagation in a 2DEG that are highly relevant to the development of spin logic devices. First, coherent precession within a propagating spin density is lost for $T$ well below room temperature. We note that, in agreement with theoretical expectation [16], this decoherence is not a consequence of the transition from ballistic to diffusive motion, as coherence remains robust when the electron mean-free-path is a factor of ten smaller than precession length. The cause (or causes) of decoherence is not known as present, although recent theoretical work has identified potential factors such as inelastic scattering, electron-electron collisions, and the cubic Dresselhaus spin-orbit interaction [68]. Second, a remarkable form of spin/charge separation takes place in a packet of polarized electrons and unpolarized holes immersed in a Fermi sea of drifting electrons. While co-propagation may be expected on general grounds for a Galilean invariant system [69, 70], here disorder, SO interactions, and the presence of holes all break the translational symmetry, suggesting that a more general principle is at work. Finally, while the spin packet co-propagates with the 2DEG, spin diffusion is strongly suppressed by spin Coulomb drag, leading to anomalous rigidity of the drifting pulse of polarization. Hopefully these observations will encourage a deeper understanding of the underlying physics of spin propagation in metallic systems, providing the basis for extending the temperature range of spin-current control.

# Chapter 7

# Coherent propagation of spin helices

As mentioned in previous chapters, for GaAs QWs, there exist two two normal mode of the system. For a Fermi sea at rest with respect to the lattice, the modes are overdamped, that is spin density fluctuations decay exponentially, with a lifetime that depends on the distance in parameter space of the SO Hamiltonian from the SU(2) point [17, 20]. However, it has been predicted that helical modes become underdamped coherent excitations in a drifting Fermi sea [23, 31], as would result from an electric field applied in the plane, for example. In this regime, the spin polarization helix propagates at least one wavelength before it decays and the local spin density acquires an oscillatory component. This form of coherent propagation is essential in order for spins to ultimately play a role in information processing. As the theoretical predictions are based on simplified models that neglect electron-electron and electron-phonon coupling, it is an open question as to whether such modes exist in real, interacting many-body systems. In this chapter, we present the observation of such modes.

## 7.1 Time evolution of SDW at high fields

Spin density waves with out-of-plane polarization and wave vector, $\boldsymbol{q}$, along the [110] crystal axis were photoinjected by 100 fs pulses from a Ti:sapphire laser focused to deliver an intensity of 80 nJ cm$^{-2}$. Drift motion of the 2DEG parallel to $\boldsymbol{q}$ was induced by in-plane electric fields, $\boldsymbol{E}$, applied parallel to $\boldsymbol{q}$, with variable strength up to 70 V cm$^{-1}$. For a spin wave that propagates uniformly with exponentially decaying amplitude, the photodiode signal will have the form of a damped oscillation, that is, $V(t) \sim S_z(\boldsymbol{q}; 0) \exp[-\gamma(q)t] \cos(\boldsymbol{q} \cdot \boldsymbol{v}t + \phi_0)$.

Figure 7.1 shows the time evolution of a $q = 1.07 \times 10^4$ cm$^{-1}$ spin wave, photoinjected into the 2DEG held at 10 K, as recorded with the technique described above. The dotted lines illustrate the exponential decay observed when the applied electric field is zero. (Both the amplitude and its negative are shown as a guide to eye in interpreting the signals observed with nonzero field). The red and blue curves are the signals recorded with nonzero $\boldsymbol{E}$ and $\phi_0$ set to 0 and $\pi/2$, respectively. The oscillations that appear with application of $\boldsymbol{E}$ clearly

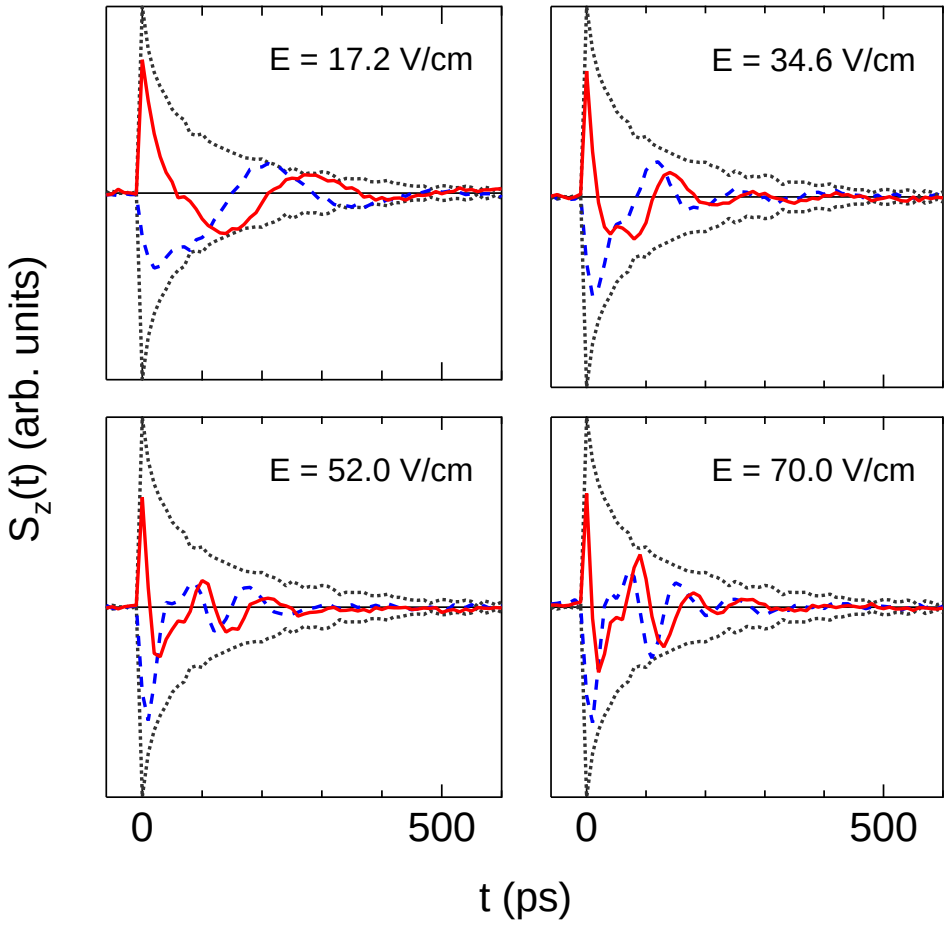


Figure 7.1: Time evolution of a transient spin grating for various applied electric fields at $q = 1.07 \times 10^4$ cm$^{-1}$ and $T = 10$ K. The black dotted lines show the decay of the amplitude in zero field (the negative of the amplitude is shown as well as a guide to the eye). The red and blue curves are the spin grating with $\phi_0$ set to 0 and $\pi/2$, respectively.

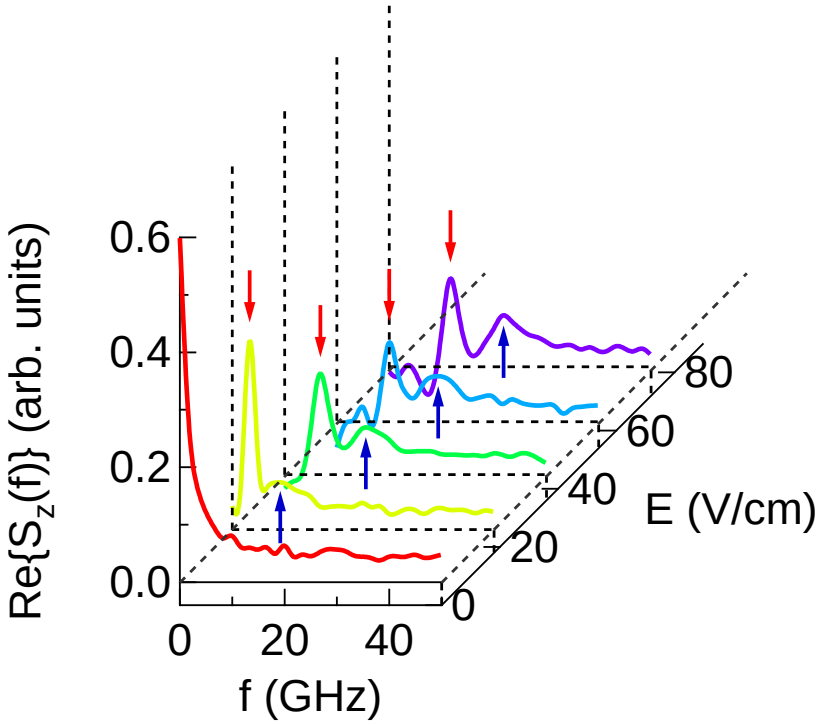


Figure 7.2: The real part of the Fourier transform of the in-phase component of $S_z(t)$ for various $E$ at 10 K, as a function of frequency, $f$. Two peaks (indicated by the red and blue arrows) are observed for each value of $E$. Each peak frequency is the inverse of the time required for a spin helix to propagate a distance equal to its wavelength.

demonstrate coherent propagation of spin density waves. Roughly speaking, each period of the oscillations corresponds to a translation of the transient spin grating by one wavelength. The drift velocity can be estimated directly from the raw data; for example, at $E = 17.2$ V cm$^{-1}$ the period is of order 250 ps, during which time the spin wave shifts by approximately 6 microns, corresponding to a drift velocity of $\sim 2 \times 10^6$ cm s$^{-1}$. Even at this relatively low electric field, the velocity of the current-driven spin texture is quite large, as compared, for example, to driven domain walls in ferromagnets where the typical maximum velocity is $\sim 10^4$ cm s$^{-1}$ [71].

## 7.2 Spin propagation spectra

Closer inspection of the curves in Fig. 7.1, particularly at higher fields, indicates additional structure is present that cannot be described by a single damped sine or cosine function. To better understand the origin of these features, we Fourier transform the data from time

to frequency domain; the real part of the transform of the $\phi_{pld} = 0$ (red curves) is plotted in Fig. 7.2. As is apparent from the spectra, the structure in the time domain reflects the fact that there are actually two propagating modes at this wave vector, which become more clearly resolved with increasing $\boldsymbol{E}$.

If the SDW undergoes normal diffusion and drift, its amplitude and phase will evolve according to

$$S_z(q,t) = S_0 \exp[-\gamma(q)t] \cos[\dot{\phi}(q)t + \phi_0]. \tag{7.1}$$

The real part of the Fourier transform of for $\phi_0 = 0$ is

$$\Re\{S_z(q,\omega)\} = \frac{S_0}{2}\left[\frac{\gamma}{\gamma^2 + (\omega - \dot{\phi})^2} + \frac{\gamma}{\gamma^2 + (\omega + \dot{\phi})^2}\right], \tag{7.2}$$

which is symmetrical about $\omega = 0$, and has two resonant peaks at $\omega = \pm\dot{\phi}$, respectively. We would expect one resonant peak for $\omega > 0$ provided that $\dot{\phi} > \gamma$ (underdamped condition). The width of it is given by the decay rate $\gamma$.

The salient features of Fig. 7.2 indicate that the SDW does not simply evolve according to Eq. 7.1, because there are two normal modes as a consequence of the SO coupling. Instead, a current-driven SDW evolves as

$$S_z(q,t) = S_0 \sum_{i=+,-} \Re\{A_i(q) \exp[-i\phi_0 - i\omega_i(q)t]\}, \tag{7.3}$$

where the weighing factor $A_\pm$ is complex in general, and the normal modes can be decomposed into the decay rate and the rate of phase advance [23, 31]:

$$i\omega_\pm(q) = \gamma_\pm(q) + i\dot{\phi}_\pm(q). \tag{7.4}$$

The spectrum of Eq. 7.3 has four resonant peaks at $\omega = \pm\dot{\phi}_\pm$, respectively. For $\omega > 0$, we expect and observe experimentally two peaks at $\omega = |\dot{\phi}_\pm|$ corresponding to the rates of the phase advance of the spin-orbit reduced and enhanced modes, respectively.

## 7.3 Dispersion relations and spin texture velocity

Figures 7.3 and 7.4 illustrate how the time revolution and spectra shown in Figs. 7.1 and 7.2 vary with wave vector, respectively. For each value of $\boldsymbol{q}$, two modes are seen, again most clearly resolved at the highest field. The inset of each panel in Fig. 7.4 shows the increase of the frequency of the two peaks with increasing $\boldsymbol{E}$. The interpretation of the two collective modes observed with nonzero $\boldsymbol{E}$ follows directly from our understanding of the modes with $\boldsymbol{E} = 0$. The out-of-plane polarized spin wave that is photogenerated at time delay zero is an equal weight superposition of the two oppositely oriented helical normal modes [62]. In zero field, as stated previously, the two photoinduced helices decay exponentially, with different lifetimes. When photoinjected into a drifting Fermi sea our results show that both helices

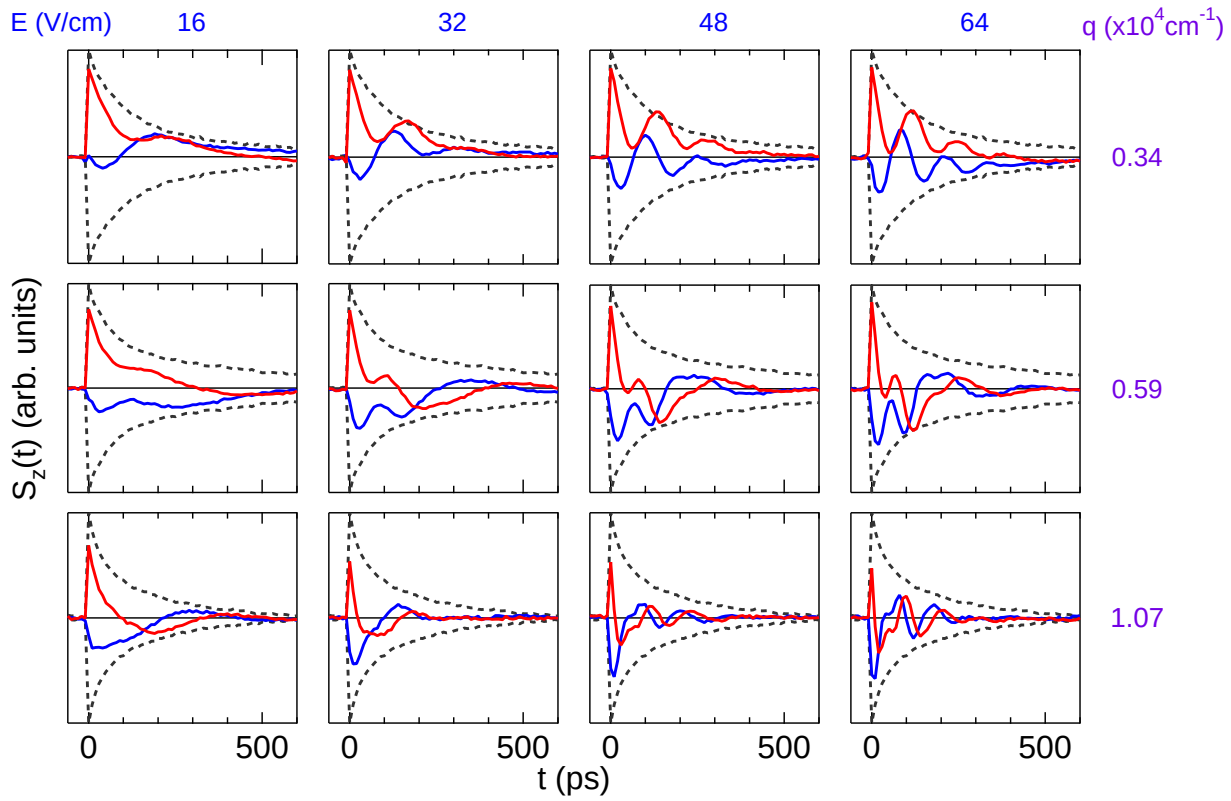


Figure 7.3: The time evolution of spin grating for different values of applied $E$ field and wave vector $q$ at $T = 30$ K.

propagate coherently, but at different velocities, yielding the two resonant frequencies for each wave vector.

In Fig. 7.5a, we plot the frequencies, $f_{\pm}$, of the two modes as a function of wave vector for $E = 64$ V cm$^{-1}$. Both helices disperse linearly and with very nearly the same slope, in qualitative agreement with theoretical predictions for the modes of a drifting 2DEG in the presence of SO coupling [23, 31]. In particular, Kleinert and Bryksin [31] (KB) obtained a dispersion relation of the form, $2\pi f_{\pm}(q) = i\gamma_{\pm}(q) + v_d(q \pm q_0)$, where $v_d$ is the drift velocity, $\gamma_{\pm}$ are the helix decay rates, and $q_0$ is the wave vector at which the lifetime of the SO stabilized helix is maximal. The KB dispersion relation is somewhat unusual, as it predicts that the longer-lived, (-), helix is stationary when $q = q_0$ and actually propagates in the direction opposite to the 2DEG for $q < q_0$. However, the propagation of the helical pattern is not equivalent to the velocity of the envelope of a packet of spin polarization. For example, a helical pattern of noninteracting localized spins in an applied magnetic field will appear to propagate with $v = \omega_Z/q$, where $\hbar\omega_Z$ is the Zeeman energy, whereas an envelope of spin polarization would be immobile.

Applying the usual analysis of wave packet motion to the KB dispersion relation shows

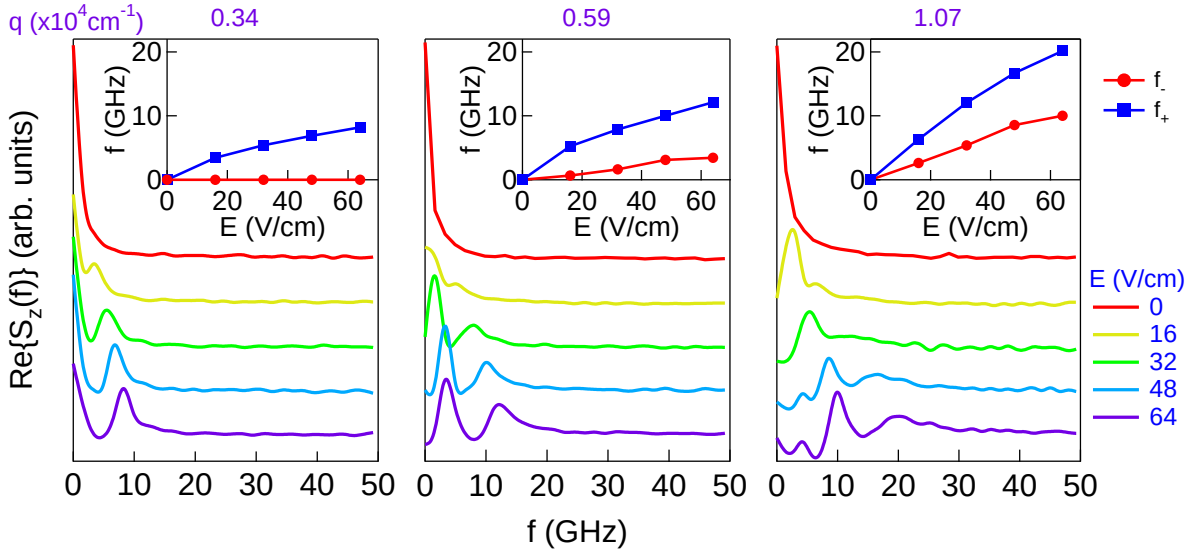


Figure 7.4: The three panels show the Fourier transform of $S_z(t)$ as a function of $f$ for several values of $E$ at $T = 30$ K, for (left to right) $q$=0.34, 0.59, and $1.07\times10^4$ cm$^{-1}$. Inset: the frequencies of the two peaks as a function of $E$.

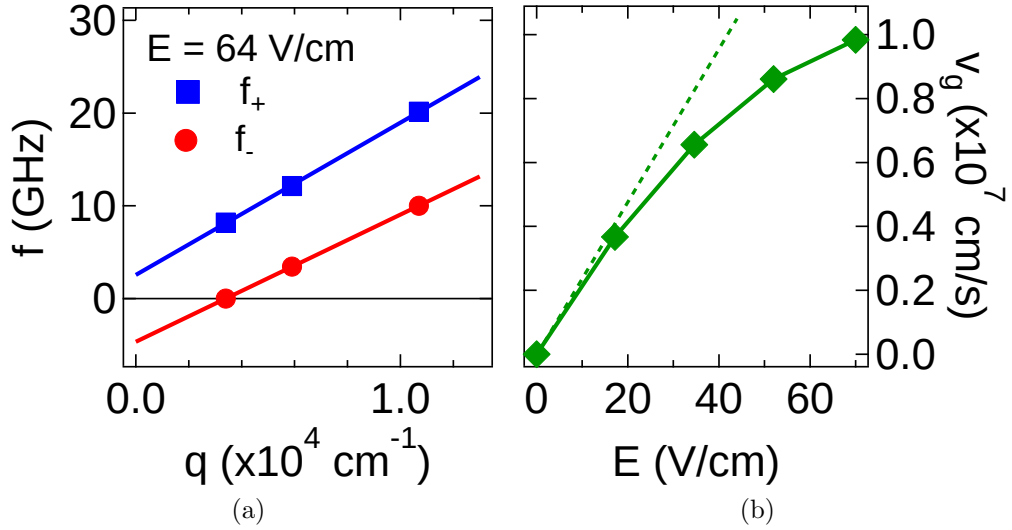


Figure 7.5: (a) The dispersion relations of the resonant frequencies associated with the two helical modes, $f_\pm$, at $E = 64$ V cm$^{-1}$ and $T = 30$ K. The solid lines are a linear fit. (b) The group velocity $v_g$ of the spin packet as a function of the applied $E$ field at $q = 1.07 \times 10^4$ cm$^{-1}$ and $T = 10$ K. The dashed line is the extrapolation of the linear response regime at low $E$, i.e., $v_g = \mu_s E$.

that it is the quantity $\partial\omega/\partial q$ (where $\omega = 2\pi f$), rather than the frequencies of the modes themselves, that determines the group velocity, $v_g$, at which a spin polarized wave packet will propagate. In Fig. 7.5b, we plot $v_g$ as a function of $E$, as determined from the average value of $\partial\omega/\partial q$ for the two modes. The group velocity increases linearly at first and then begins to saturate with further increase of $E$, nevertheless reaching $\sim 10^7$ cm s$^{-1}$ at 70 V cm$^{-1}$, which is approximately the Fermi velocity. In the linear regime at low $E$, the spin mobility $\mu_s \equiv v_g/E \approx 2.5 \times 10^5 \mathrm{cm^2 V^{-1} s^{-1}}$, which is roughly half of the electron mobility as determined from dc transport methods. This difference is consistent with the observation [24] that $v_g/v_d$ depends on the photoinjected electron density, $\Delta n$, approaching unity only in the limit that $\Delta n/n \to 0$.

Our results demonstrate that overdamped modes of a spin-orbit coupled 2DEG in GaAs crossover to coherently propagating helical waves when the spin-precession period becomes smaller than the spin-relaxation time, which for our sample occurs in the presence of modest electric fields $\sim$0.2 V applied across a 200 micron channel. In the Dresselhaus-coupled system studied here, electron spins precess $\sim$3 full revolutions within the 200 ps polarization lifetime, during which time a wave packet of spin polarization will propagate $\sim$25 microns. These results suggest that controlling the coherence length of spin transport, with large dynamic range, can be achieved by adding Rashba SO coupling via out-of-plane electric fields. For example, a $\times$50 variation of helix lifetime as a function of electric fields applied by asymmetric doping has been demonstrated [21] and, in theory, this dynamic range can be exceeded with fields applied by an external gate electrode. Finally, the phenomena that we have observed in semiconductor quantum wells should arise in all inversion breaking SO systems, of particular interest are those in which stronger coupling implies nanoscale precession lengths and precession rates in the terahertz regime.

# Bibliography


[1] Y. A. Bychkov and E. I. Rashba. "Oscillatory effects and the magnetic susceptibility of carriers in inversion layers". In: *J. Phys. C* 17.33 (1984), pp. 6039–6045.

[2] J. Sinova et al. "Universal Intrinsic Spin Hall Effect". In: *Phys. Rev. Lett.* 92.12 (2004), p. 126603.

[3] S. Murakami, N. Nagaosa, and S.-C. Zhang. "Dissipationless Quantum Spin Current at Room Temperature". In: *Science* 301 (2003), pp. 1348–1351.

[4] C. L. Kane and E. J. Mele. "Quantum Spin Hall Effect in Graphene". In: *Phys. Rev. Lett.* 95.22 (2005), p. 226801.

[5] M. König et al. "Quantum Spin Hall Insulator State in HgTe Quantum Wells". In: *Science* 318 (2007), pp. 766–770.

[6] Tomasz Dietl et al. *Spintronics*. Vol. 82. Semiconductors and Semimetals. Academic Press, New York, 2008.

[7] J. Fabian et al. "Semiconductor spintronics". In: *Acta Phys. Slovaca* 57 (2007), pp. 565–907.

[8] M. W. Wu, J. H. Jiang, and M. Q. Weng. "Spin dynamics in semiconductors". In: *Phys. Rep.* 493 (2010), pp. 61–236.

[9] F. J. Ohkawa and Y. Uemura. "Quantized surface states of a narrow-gap semiconductor". In: *J. Phys. Soc. Jpn.* 37 (1974), p. 1325.

[10] Y. A. Bychkov and E. I. Rashba. "Properties of a 2D electron gas with lifted spectral degeneracy". In: *JETP Lett.* 39 (1984), p. 78.

[11] M. I. D'yakonov and V. I. Perel'. "Possibility of Orienting Electron Spins with Current". In: *JETP Lett.* 13 (1971), p. 467.

[12] M. I. D'yakonov and V. I. Perel'. "Spin Orientation of Electrons Associated with the Interband Absorption of Light in Semiconductors". In: *Sov. Phys. JETP* 33 (1971), p. 1053.

[13] F. Meier and B. P. Zakharchenya. *Optical Orientation*. Vol. 8. Modern Problems in Condensed Matter Sciences. North-Holland, Amsterdam, 1984.

[14] M. I. D'yakonov and V. Yu. Kachorovskii. In: *Sov. Phys. Semicond.* 20 (1986), p. 110.

[15] G. Dresselhaus. "Spin-orbit coupling effects in zinc blende structures". In: *Phys. Rev.* 100 (1955), pp. 580–586.

[16] John Schliemann, J. Carlos Egues, and Daniel Loss. "Nonballistic Spin-Field-Effect Transistor". In: *Phys. Rev. Lett.* 90 (2003), p. 146801.

[17] B. Andrei Bernevig, J. Orenstein, and Shou-Cheng Zhang. "Exact SU(2) Symmetry and Persistent Spin Helix in a Spin-Orbit Coupled System". In: *Phys. Rev. Lett.* 97 (2006), p. 236601.

[18] A. A. Burkov, Alvaro S. Núñez, and A. H. MacDonald. "Theory of spin-charge-coupled transport in a two-dimensional electron gas with Rashba spin-orbit interactions". In: *Phys. Rev. B* 70.15 (2004), p. 155308.

[19] E. G. Mishchenko, A. V. Shytov, and B. I. Halperin. "Spin Current and Polarization in Impure Two-Dimensional Electron Systems with Spin-Orbit Coupling". In: *Phys. Rev. Lett.* 93 (2004), p. 226602.

[20] Tudor D. Stanescu and Victor Galitski. "Spin relaxation in a generic two-dimensional spin-orbit coupled system". In: *Phys. Rev. B* 75 (2007), p. 125307.

[21] J. D. Koralek et al. "Emergence of the persistent spin helix in semiconductor quantum wells". In: *Nature (London)* 458.2 (2009), pp. 610–613.

[22] M. P. Walser et al. "Direct mapping of the formation of a persistent spin helix". In: *Nature Physics* 8 (2012), pp. 757–762.

[23] Luyi Yang, J. Orenstein, and Dung-Hai Lee. "Random walk approach to spin dynamics in a two-dimensional electron gas with spin-orbit coupling". In: *Phys. Rev. B* 82 (15 2010), p. 155324.

[24] Luyi Yang et al. "Doppler velocimetry of spin propagation in a two-dimensional electron gas". In: *Nature Physics* 8 (2012), pp. 153–157.

[25] Luyi Yang et al. "Coherent Propagation of Spin Helices in a Quantum-Well Confined Electron Gas". In: *Phys. Rev. Lett.* 109 (2012), p. 246603.

[26] Luyi Yang et al. "Measurement of Electron-Hole Friction in an $n$-Doped GaAs/AlGaAs Quantum Well Using Optical Transient Grating Spectroscopy". In: *Phys. Rev. Lett.* 106 (24 2011), p. 247401.

[27] A. R. Cameron, P. Riblet, and A. Miller. "Spin Gratings and the Measurement of Electron Drift Mobility in Multiple Quantum Well Semiconductors". In: *Phys. Rev. Lett.* 76 (1996), pp. 4793–4796.

[28] G. D. Goodno, G. Dadusc, and R. J. D. Miller. "Ultrafast heterodyne-detected transient-grating spectroscopy using diffractive optics". In: *J. Opt. Soc. Am. B* 15 (1998), pp. 1791–1794.

[29] A. A. Maznev, K. A. Nelson, and J. A. Rogers. "Optical heterodynedetection of laser-induced gratings". In: *Opt. Lett.* 23 (1998), pp. 1319–1321.

[30] N. Gedik and J. Orenstein. "Absolute phase measurement in heterodyne detection of transient gratings". In: *Opt. Lett.* 29 (2004), pp. 2109–2111.

[31] P. Kleinert and V. V. Bryksin. "Spin polarization in biased Rashba-Dresselhaus two-dimensional electron systems". In: *Phys. Rev. B* 76 (2007), p. 205326.

[32] Roland Winkler. *Spin-Orbit Coupling Effects in Two-Dimensional Electron and Hole Systems*. Vol. 191. Springer Tracts in Modern Physics. Springer, New York, 2003.

[33] P. Kleinert and V. V. Bryksin. "Electric-field-induced long-lived spin excitations in two-dimensional spin-orbit coupled systems". In: *Phys. Rev. B* 79 (2009), p. 045317.

[34] M. M. Glazov and E. Ya. Sherman. "Nonexponential spin relaxation in magnetic fields in quantum wells with random spin-orbit coupling". In: *Phys. Rev. B* 71 (2005), 241312(R).

[35] V. K. Dugaev et al. "Spin relaxation and combined resonance in two-dimensional electron systems with spin-orbit disorder". In: *Phys. Rev. B* 80 (2009), 081301(R).

[36] Munekazu Ohno and Kanji Yoh. "Datta-Das-type spin-field-effect transistor in the nonballistic regime". In: *Phys. Rev. B* 77 (2008), p. 045323.

[37] Supriyo Datta and Biswajit Das. "Electronic analog of the electro-optic modulator". In: *Appl. Phys. Lett.* 56 (1990), pp. 665–667.

[38] H.J. Eichler, P. Gunter, and D.W. Pohl. *Laser-Induced Dynamic Gratings*. Springer-Verlag, Berlin, 1986.

[39] N. Gedik et al. "Diffusion of Nonequilibrium Quasi-Particles in a Cuprate Superconductor". In: *Science* 300 (2003), pp. 1410–1413.

[40] C. P. Weber et al. "Observation of spin Coulomb drag in a two-dimensional electron gas". In: *Nature (London)* 437 (2005), pp. 1330–1333.

[41] P. Vohringer and N.F. Scherer. "Transient Grating Optical Heterodyne Detected Impulsive Stimulated Raman Scattering in Simple Liquids". In: *J. Phys. Chem.* 99.9 (1995), 2684C2695.

[42] Y.J. Chang, P. Cong, and J.D. Simon. "Optical heterodyne detection of impulsive stimulated Raman scattering in liquids". In: *J. Phys. Chem.* 99.20 (1995), 7857C7859.

[43] Nuh Gedik. "Recombination and Propagation of Quasiparticles in Cuprate Superconductors". PhD thesis. University of California at Berkeley, 2005.

[44] S.M. Sze and K.K. Ng. *The Physics of Semiconductor Devices*. John Wiley and Sons, New York, 2003.

[45] D.A. Neamen. *Semiconductor Physics and Devices: basic principles*. 3rd ed. Ch. 6. McGraw-Hill Higher Education, Boston, 2003.

[46] I. Žutić, J. Fabian, and S. Das Sarma. "Spintronics: Fundamentals and applications". In: *Rev. Mod. Phys.* 76 (Apr. 2004), pp. 323–410.

[47] D. D. Awschalom and M. E. Flatté. "Challenges for semiconductor spintronics". In: *Nature Physics* 3 (2007), pp. 153–159.

[48] R. A. Höpfel et al. "Negative absolute mobility of minority electrons in GaAs quantum wells". In: *Phys. Rev. Lett.* 56 (1986), pp. 2736–2739.

[49] P. Price. "Hot electron effects in heterolayers". In: *Physica (Amsterdam) B+C* 117 (1983), pp. 750–752.

[50] T. J. Gramila et al. "Mutual friction between parallel two-dimensional electron systems". In: *Phys. Rev. Lett.* 66 (1991), pp. 1216–1219.

[51] U. Sivan, P. M. Solomon, and H. Shtrikman. "Coupled electron-hole transport". In: *Phys. Rev. Lett.* 68 (1992), pp. 1196–1199.

[52] Ka Shen and G. Vignale. "Interacting Drift-Diffusion Theory for Photoexcited Electron-Hole Gratings in Semiconductor Quantum Wells". In: *Phys. Rev. Lett.* 110 (2013), p. 096601.

[53] A. F. Croxall et al. "Anomalous Coulomb Drag in Electron-Hole Bilayers". In: *Phys. Rev. Lett.* 101.24 (2008), p. 246801.

[54] J. A. Seamons et al. "Coulomb Drag in the Exciton Regime in Electron-Hole Bilayers". In: *Phys. Rev. Lett.* 102.2 (2009), p. 026804.

[55] L. Zheng and A. H. MacDonald. "Coulomb drag between disordered two-dimensional electron-gas layers". In: *Phys. Rev. B* 48 (1993), pp. 8203–8209.

[56] K. Flensberg and B. Y.-K. Hu. "Plasmon enhancement of Coulomb drag in double-quantum-well systems". In: *Phys. Rev. B* 52 (1995), pp. 14796–14808.

[57] G. Vignale and A. H. MacDonald. "Drag in Paired Electron-Hole Layers". In: *Phys. Rev. Lett.* 76 (1996), pp. 2786–2789.

[58] G.F. Giuliani and G. Vignale. *Quantum theory of the electron liquid*. Ch. 4. University Press, 2005.

[59] H. C. Koo et al. "Control of Spin Precession in a Spin-Injected Field Effect Transistor". In: *Science* 325 (Sept. 2009), pp. 1515–1518.

[60] J. Wunderlich et al. "Spin Hall Effect Transistor". In: *Science* 330 (2010), pp. 1801–1804.

[61] J. M. Kikkawa and D. D. Awschalom. "Lateral drag of spin coherence in gallium arsenide". In: *Nature (London)* 397 (1999), pp. 139–141.

[62] C. P. Weber et al. "Nondiffusive Spin Dynamics in a Two-Dimensional Electron Gas". In: *Phys. Rev. Lett.* 98.7 (2007), p. 076604.

[63] I. D'amico and G. Vignale. "Theory of spin Coulomb drag in spin-polarized transport". In: *Phys. Rev. B* 62 (2000), pp. 4853–4857.

[64] K. Flensberg, T. Stibius Jensen, and N. Asger Mortensen. "Diffusion equation and spin drag in spin-polarized transport". In: *Phys. Rev. B* 64.24 (2001), p. 245308.

[65] Irene D'Amico and Giovanni Vignale. "Spin Coulomb drag in the two-dimensional electron liquid". In: *Phys. Rev. B* 68 (2003), p. 045307.

[66] S. A. Crooker and D. L. Smith. "Imaging Spin Flows in Semiconductors Subject to Electric, Magnetic, and Strain Fields". In: *Phys. Rev. Lett.* 94.23 (2005), p. 236601.

[67] W. J. H. Leyland et al. "Enhanced spin-relaxation time due to electron-electron scattering in semiconductor quantum wells". In: *Phys. Rev. B* 75.16 (Apr. 2007), p. 165309.

[68] M. C. Lüffe, J. Kailasvuori, and T. S. Nunner. "Relaxation mechanisms of the persistent spin helix". In: *Phys. Rev. B* 84.7 (2011), p. 075326.

[69] M. E. Flatté and J. M. Byers. "Spin Diffusion in Semiconductors". In: *Phys. Rev. Lett.* 84 (2000), pp. 4220–4223.

[70] I. D'Amico and G. Vignale. "Spin diffusion in doped semiconductors: The role of Coulomb interactions". In: *Europhys. Lett.* 55 (2001), pp. 566–572.

[71] S. S. P. Parkin, M. Hayashi, and L. Thomas. "Magnetic Domain-Wall Racetrack Memory". In: *Science* 320 (2008), pp. 190–194.

[72] M.V. Weckwerth et al. "Epoxy bond and stop-etch (EBASE) technique enabling backside processing of (Al)GaAs heterostructures". In: *Superlattice Microst.* 20.4 (1996), pp. 561–567.

# Appendix A

# Sample processing

In this appendix, we detail the sample fabrication procedures. Sample growth and processing and some of the transport measurements were performed at the Center for Integrated Nanotechnologies (CINT), Sandia National Laboratories. John Reno grew our GaAs quantum well samples. Denise Tibbetts taught me how to process the devices at CINT. Michael Lilly and I did the transport measurements by the standard van der Pauw techniques.[1]

## A.1 Introduction

### Sample growth

The samples were grown by MBE on top of a semi-insulating [001] GaAs wafer. The crystal directions of the wafer are shown in Fig. A.1. John has grown several wafers with different structures for us. We did most measurements on the first wafer (VB0355) described as follows. It is symmetric QW structures such that the Rashba interaction is near zero and the Dresselhaus coupling dominates ($\beta_1 = 3.4 \times 10^{-3}$ eVÅ). An initial 500 nm $Al_{0.55}Ga_{0.45}As$ etch stop layer was grown on the substrate, followed by a second 10 nm etch stop of GaAs. The lower barrier was 210 nm $Al_{0.24}Ga_{0.76}As$ with Si $\delta$-doping 95 nm below the 9 nm GaAs quantum well. The upper barrier of 190 nm $Al_{0.24}Ga_{0.76}As$ includes a $\delta$-doped layer 75 nm above the quantum well. The top layer is a 10 nm GaAs cap. The slight asymmetry in the $\delta$-doped layers compensates for the upward drift of the Si atoms and results in nearly symmetric doping when the growth is complete. The GaAs cap layers prevent oxidation of the AlGaAs barriers. The layers after the growth are schematically demonstrated in Fig. A.2. Then the wafter was cut into $\sim 1 \times 1$ cm$^2$ pieces along the [110] and [1$\bar{1}$0] axes for device fabrication.

[1]The van der Pauw method is a technique commonly used to measure the resistivity and the Hall coefficient of a sample. There is a good description on Wikipedia. The ohmic contacts were made by soldering 50/50 In/Sn on the four corners of the sample under a microscope followed by RTA with the same recipe as described in A.5.

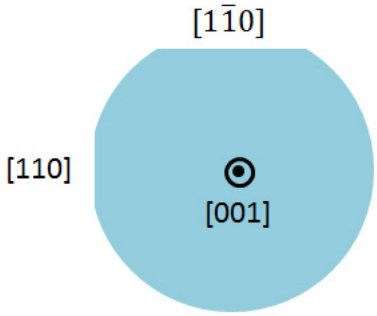


Figure A.1: Crystal axis directions for the wafers on which John Reno grows our quantum well samples. The wafers are (001) cut, undoped, 4 inches in diameter and 625 $\mu$m thick.

### Processing overview

The samples were prepared using the so-called double epoxy bond and stop-etch (EBASE) technique [72], which enables both the front and back side processing of very thin epitaxial structures. First, the 2DEG channel was defined by mesa etching, then Ohmic contact was made by annealing NiGeAu into the sample, and front gate was made by deposition of TiAu. After patterning the top side, the samples were epoxied top side down on new host substrates (c-axis cut sapphire discs in this case) and then both the GaAs substrate and AlGaAs etch stop were removed as shown in Fig. A.2 to allow for optical measurement in transmission geometry and backside processing. Then vias to the ohmic contacts and front gate were etched and finally the electrical pads and back gate were made. A schematic cross section of the device after the whole procedure is shown in Fig. A.3. The process flow for our devices is shown in Figs. A.4 and A.5, which requires five mask steps. Each mask step involves the repeated application of photolithography, which will be described in detail in Sec. A.3. In the following, we present a step-by-step procedure for device fabrication. During the process ultraclean conditions must be maintained.

## A.2 Cleaving and cleaning

Denise told me that on average fewer than half of the chips would survive after the fabrication, so we start with a few samples at a time.

GaAs is very easy to cut along [110] and [1$\bar{1}$0]. Under the solvent bench, cut the wafter into $\sim 1 \times 1$ cm$^2$ pieces. First, use a ruler and a diamond pen to scribe the surface gently. Blow off the dust with an airgun. Then use two glass slides to sandwich the sample along the scribed line and use two wooden sticks to press near that line on the edge. Gently scribe an identifying mark on the backside of each chip.

To clean the samples, we first spread acetone on the samples. Before the acetone dry, spread methanol. Then soak the samples into the rinse bath of flowing deionized (DI) water, which is a very important chemical throughout microelectrical fabrication. Wait until the

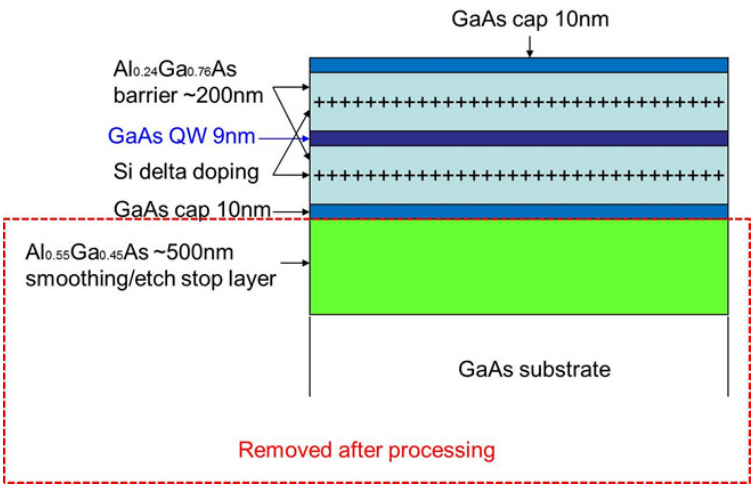


Figure A.2: Schematic cross section of the MBE growth GaAs quantum well.

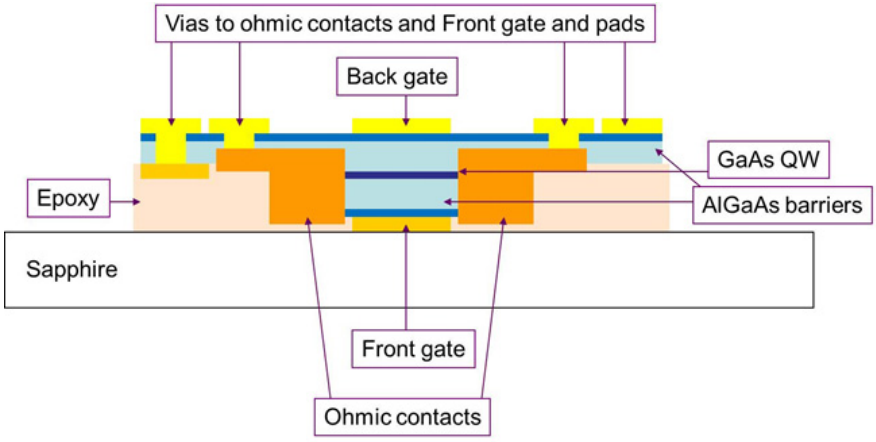


Figure A.3: Schematic cross section of the GaAs quantum well device after full processing.

resistivity of the DI water is greater than 13 MΩ cm. Take them out and blow dry the surface with nitrogen.[2]

## A.3 Photolithography

Photolithography is a photoengraving process that transfers a pattern from a mask to the surface of the sample. The patterns are first transferred from the mask to a light-sensitive chemical *photoresist* by ultraviolet (UV) light. The process takes place in a clean room illuminated with yellow light. Chemical or plasma etching, or deposition of a new material is

[2]The electrical resistivity of ultrapure water is 18 MΩ cm, but it takes too long.

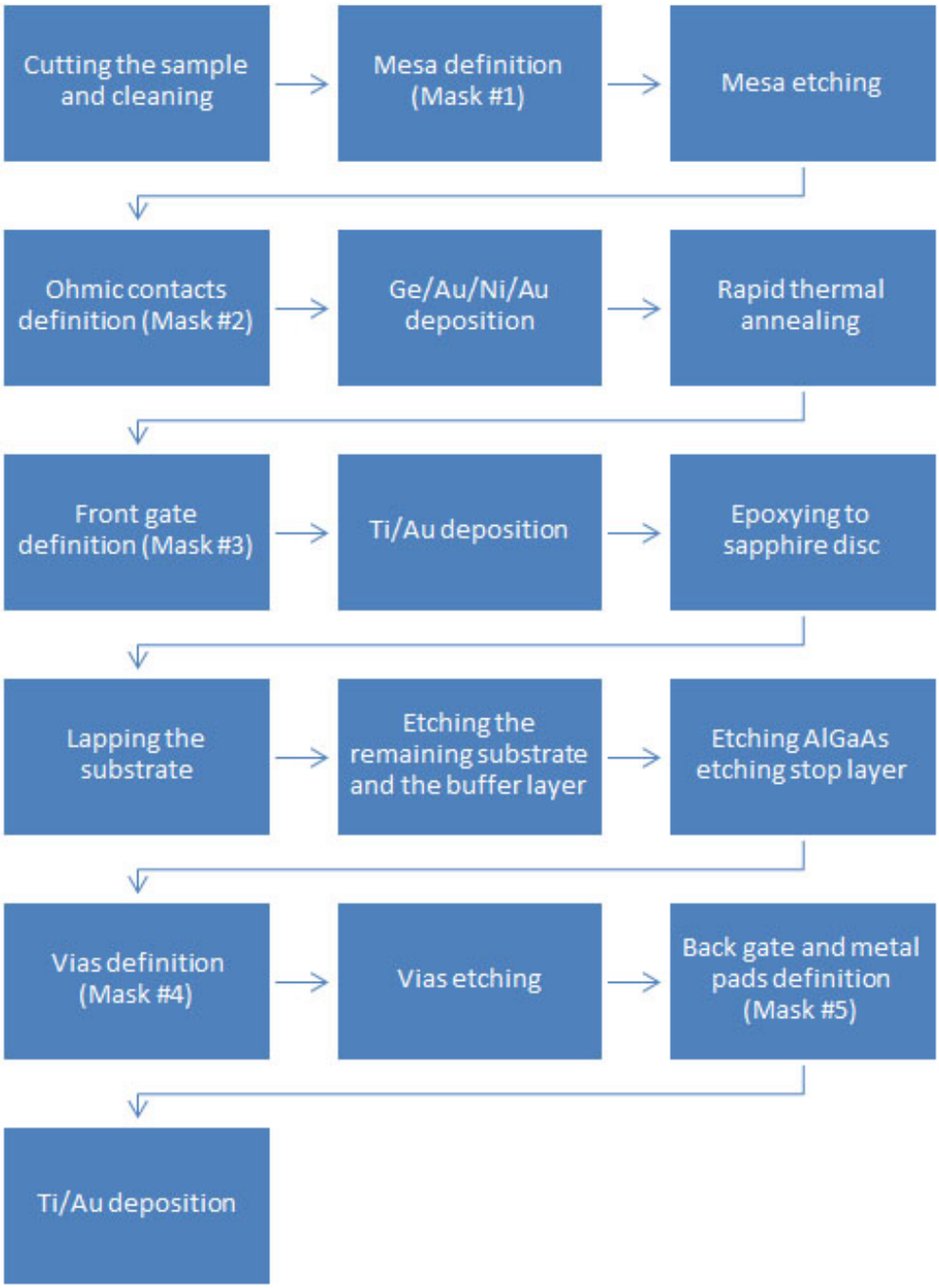


Figure A.4: Process flowchart.

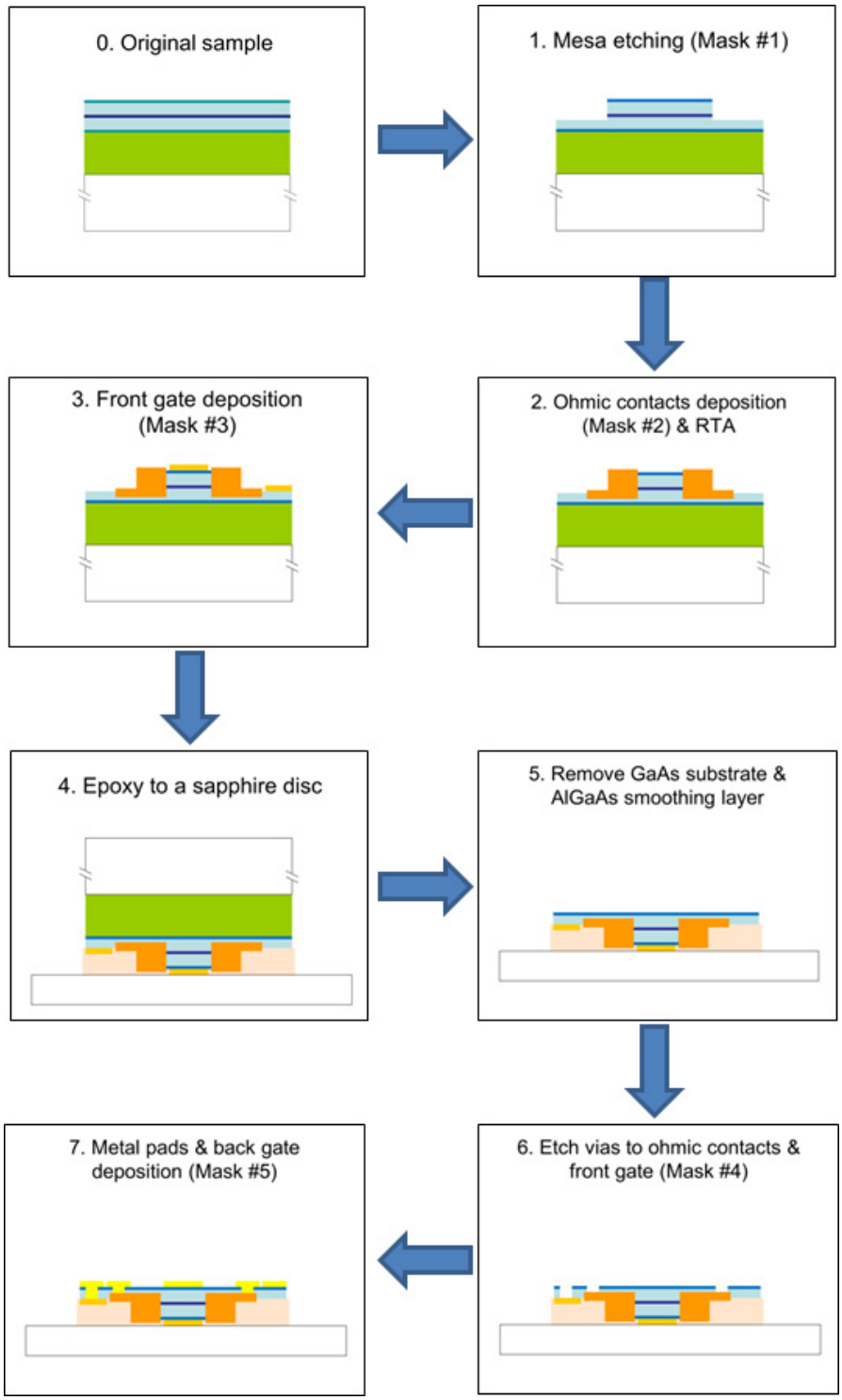


Figure A.5: Schematic process flowchart. c.f. Figs. A.2 and A.3 for the meaning of the layers in different colors.

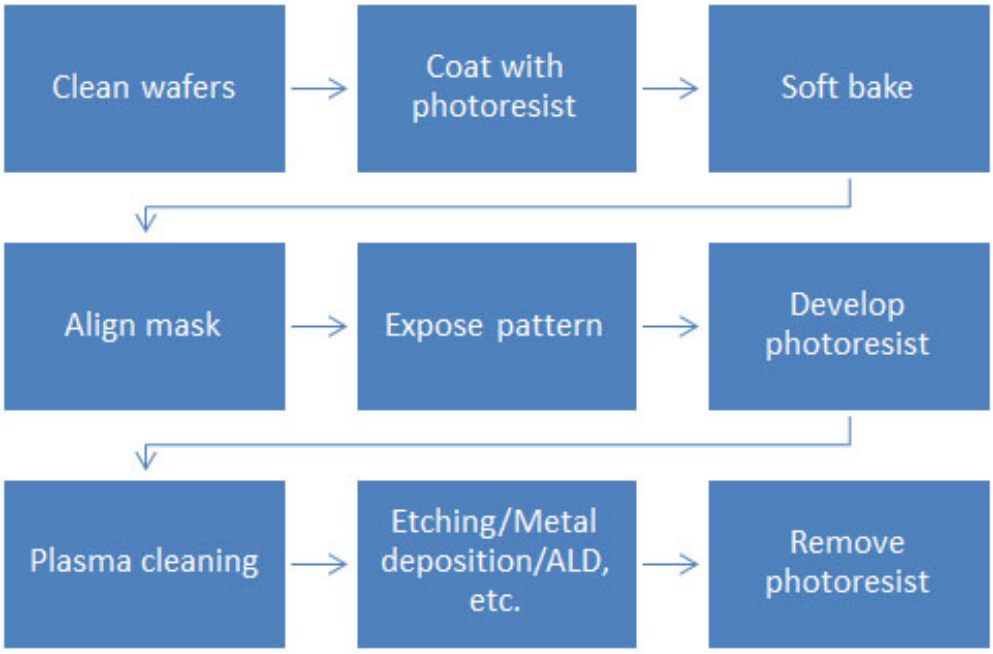


Figure A.6: Steps of the photolithographic process.

then employed to transfer the pattern from the exposure pattern to the sample. The various steps of the photolithographic process shown in Fig. A.6 and will be described in detail below followed by a discussion of the masks.

## Photolithographic process

Figure A.7 illustrates the various steps of the photolithographic process. Prior to the application of the photoresist, the surface of the samples must be clean and dry to ensure good adhesion. Load a sample on a vacuum chuck. Make sure the vacuum is good otherwise the sample will fly away when spinning the chuck. Then coat the samples with the positive tone AZ 5214-E photoresist. Drip a few drops of the photoresist to cover the sample surface. Choose the right recipe (5000 rpm for 30 sec) and start spinning. Then a thin ($\sim 1.25\mu$m) uniform layer is formed. Bake the samples on a 90 °C hot plate for 90 sec to improve adhesion and remove solvent from the photoresist.

Following the soft baking, the photoresist is ready for mask alignment and exposure. First, load the sample and mask. The mask needs to be clean as well. Be careful that the mask with the metal pattern must be face down, i.e., in close proximity to the surface of the sample. The mask is $\sim 100\mu$m above the sample surface when doing the alignment. Then move $x - y - \theta$ of the sample stage to align the sample with the mask. Each mask following the first must be carefully aligned to the previous pattern. After the alignment, the sample

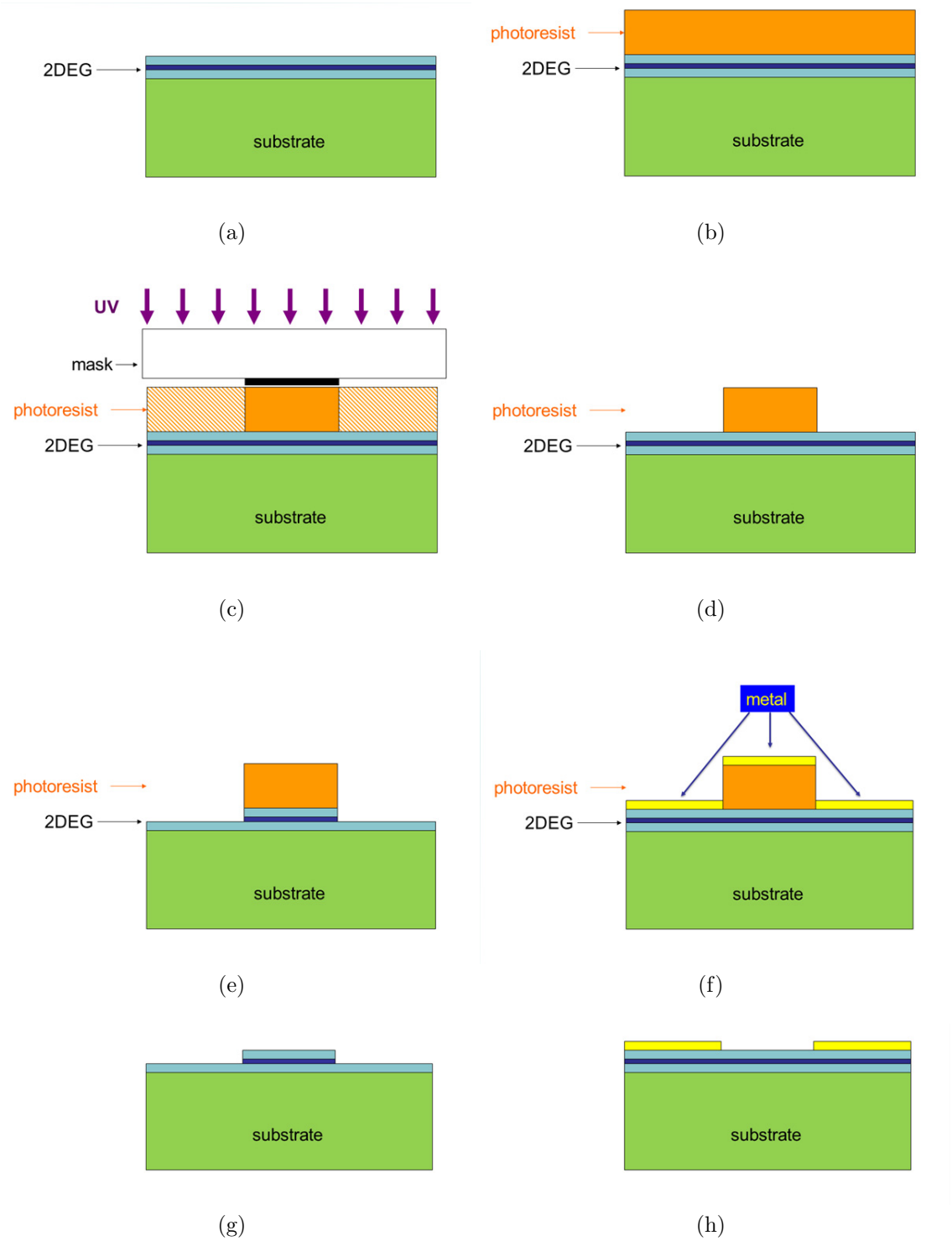


Figure A.7: Demonstration of a sample through the various steps of the photolithographic process. (a) Clean sample; (b) photoresist application; (c) mask alignment and UV exposure; (d) development; (e) mesa etching; (f) metal deposition; (g) and (h) resist removal.

is brought into contact with the mask and the photoresist is exposed through the mask with high-intensity (20 mW $cm^{-2}$) UV light ($\sim$ 400 nm) for 8.5 sec, as depicted in Fig. A.7c.

Under the base bench, develop the pattern in a beaker with 5 : 1 DI water : AZ400K developer with constant gentle agitation for about 45 sec. As shown in Fig A.7d, the resist exposed with UV light is dissolved by the developer.[3] Watch the appearance of the image until it is fully developed. Rinse in flowing DI water immediately until the resistivity is above 13 M$\Omega$ cm and blow dry with nitrogen.

Load the samples into an oxygen plasma chamber and set the strip power be 5 watts for 5 min to remove the organic polymer residues. For lithography followed by metal deposition, dip the samples into ammonium hydroxide $NH_4OH$ : DI = 1 : 20 for 30 sec and then dry with nitrogen to remove the oxygen on the surface from the plasma cleaning.

Now the samples are ready for the etching or deposition of a new material as shown in Figs. A.7e and A.7f, respectively, and then the photoresist is removed by acetone illustrated in Figs. A.7g and A.7h and will be described in the following sections.

### Mask

Before carrying out any device fabrication, the very first step to take is to devise the circuit. In our project, we need to drive the photoinduced charge/spin grating and tune the electron density and Rashba SOC by electrical gates. The laser spot diameter is about 100 $\mu$m and a uniform field across the grating is desired, so we design the active width of the 2DEG channel to be $200 - 400$ $\mu$m (larger than the laser spot) and the length is larger than the width by a factor of 4 (to ensure the field is uniform in the center of the device). Meanwhile the active area needs to be small as well to reduce the heating effect. In order to monitor the transport properties, we also make Hall bars on the same chip of the device. In addition, for a multi-mask process, the alignment marks are required.

In Fig. A.8, we plot the masks for each photolithographic process. The blank area is transparent. As depicted in Figs. A.7e and A.7g, the transparent patterns will be etched during the mesa and vias etching, and Figs. A.7f and A.7h illustrate that the metal will be deposited on the transparent patterns during the ohmic contacts, front and back gates deposition. The repeated boxes on each mask are the alignment marks. We draw the masks in AutoCad in the order of the process. Make sure each front side mask follows the 1st one is aligned and the mirror images of the backside masks are aligned with the front side ones.

## A.4 Mesa etching

First, perform mesa photolithography. Then etch the mesa with phosphoric acid. Be sure to wear all the personal protective equipments (PPE, acid protective clothing, gloves, goggles and face mask). Under the acid bench, mix the chemicals as follows: phosphoric acid ($H_3PO_4$) : hydrogen peroxide ($H_2O_2$) : DI water ($H_2O$) = 1 : 4 : 45. The average etching

[3] If a negative tone photoresist is used, the unexposed pattern is dissolved instead of the exposed region.

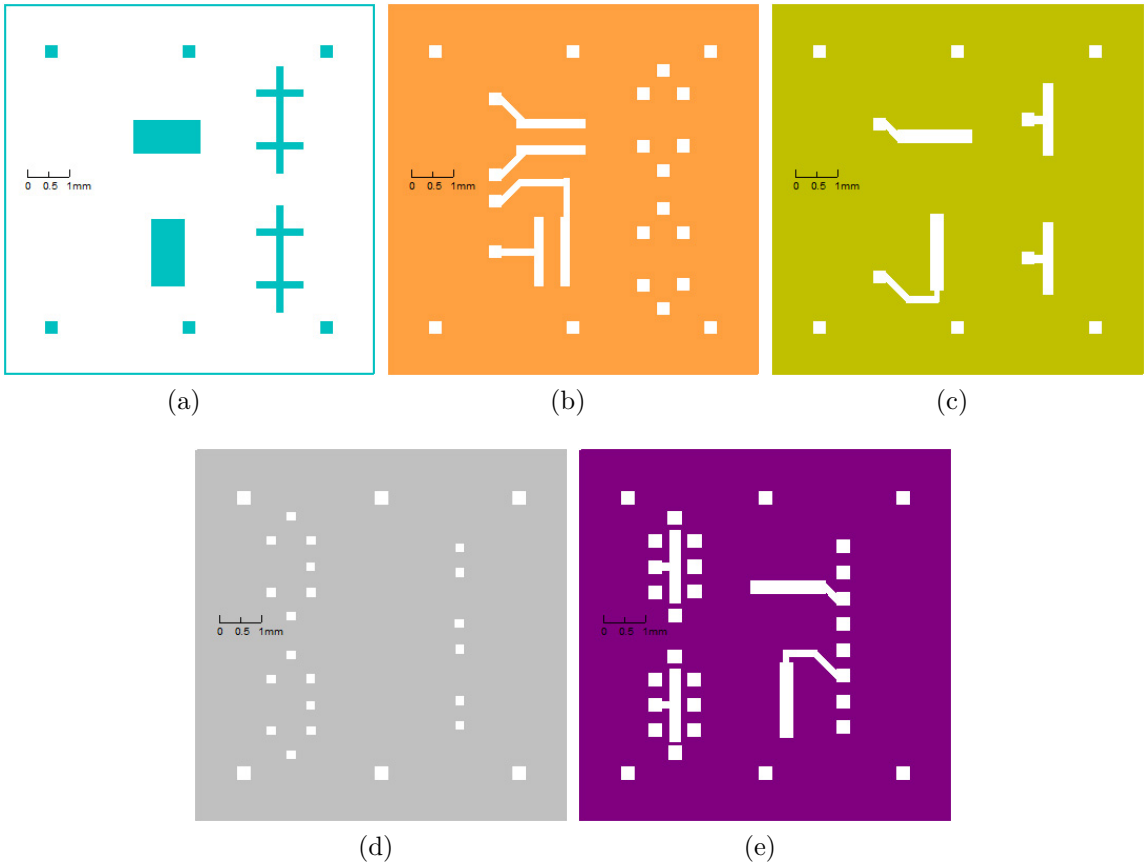


(a) (b) (c)

(d) (e)

Figure A.8: A set of masks (a) mesa; (b) ohmic contacts; (c) front gate; (d) vias; (e) back gate and metal pads.

rate is $\sim$ 60Å per sec. We etch below the Si $\delta-$doping layer, but do not want to etch all the way through the MBE−grown material. Calculate the etching depth according to the sample structure ($\sim$ 3400Å for the structure shown in Fig. A.2) and the etching time.[4] Dip the sample face up into the acid. When the etching is done, take it out and soak it into the DI water to prevent further etching.

## A.5 Creating ohmic contacts

Electrical contact is made to the 2DEG by e-beam evaporating AuGeNi onto the sample and heating the sample to a suitable temperature for a certain amount of time to allow the metals to melt and diffuse into the GaAs/AlGaAs heterostructure.

[4]Do a few test etching on dummy samples and measure the depth to get a more accurate etching rate.

First, perform ohmic photolithography. Then load the samples into the e-beam chamber and pump down until the vacuum is better than $10^{-6}$ Torr. For the ohmic contacts, the following sequence is evaporated: 260Å Ge, 540Å Au, 140Å Ni, 2000Å Au. The Ge layer allows the contact to diffuse into the sample when annealed. The Au layers reduce contact resistance. The Ni layer allows the contact to stick to the surface.

After deposition, dip the samples into acetone for at least an hour. Use acetone airbrush or acetone washer to liftoff the metal followed by methanol, DI water and nitrogen dry. It is important to remove all excess metal.

Load the samples into the rapid thermal annealing (RPA) chamber. We use the following recipe to minimize the contact resistance: Argon Vacuum 420 °C for 60 sec. The typical contact resistance at low temperatures is about 30 Ω for our samples.

## A.6 Front gate deposition

Perform front gate photolithography. To form semi-transparent Schottky gates, we deposit 50Å Ti/0 − 100Å Au to the chips by evaporation and liftoff.[5] We find that the Ti layer alone forms a good electrical gate. The Au layer reduces the transmittancy. With the thin metal, acetone liftoff is very easy.

Figure A.9a is a microscope image of the left part of the chip after the front gate deposition (c.f. Fig. A.8). Now we are done with the front side processing. The chips are ready to be epoxied to the host support substrate as shown in Fig. A.7d.

## A.7 Epoxy to sapphire

Traditionally, for transport measurements, a dummy GaAs substrate is used as the new host substrate for the EBASE process. We choose c-axis cut sapphire, because it is transparent, c-cut so that it is not birefringent for light at normal incidence, and a good thermal conductor with thermal expansion coefficient close to GaAs. The sapphire discs are from Meller optics, 0.495" in diameter, and 0.040" thick.

Gatan G-1 epoxy is used as it is low viscosity and thermally matched to GaAs. The mix ratio of weight is 1 hardener : 10 resin. Mix the two parts with a toothpick for at least 1 min. The minimum cure time varies with temperature. We heat cure the epoxy with a copper sample clamp stage on a hotplate.

Place some blue Nitto tape underneath the clamps so that the samples are not glued to the stage. Put each sapphire disc next to its own clamp. Use the tip of a toothpick to drop a small amount of the mixed epoxy at the center of the sapphire disc. The GaAs sample is placed topside down on the sapphire. Slide the sample so that it is centered on the disc and then put each chip underneath its clamp. Drop a little excess epoxy on the Nitto tape to

[5] Ti is very bright, so the protective goggles are a must during the deposition.

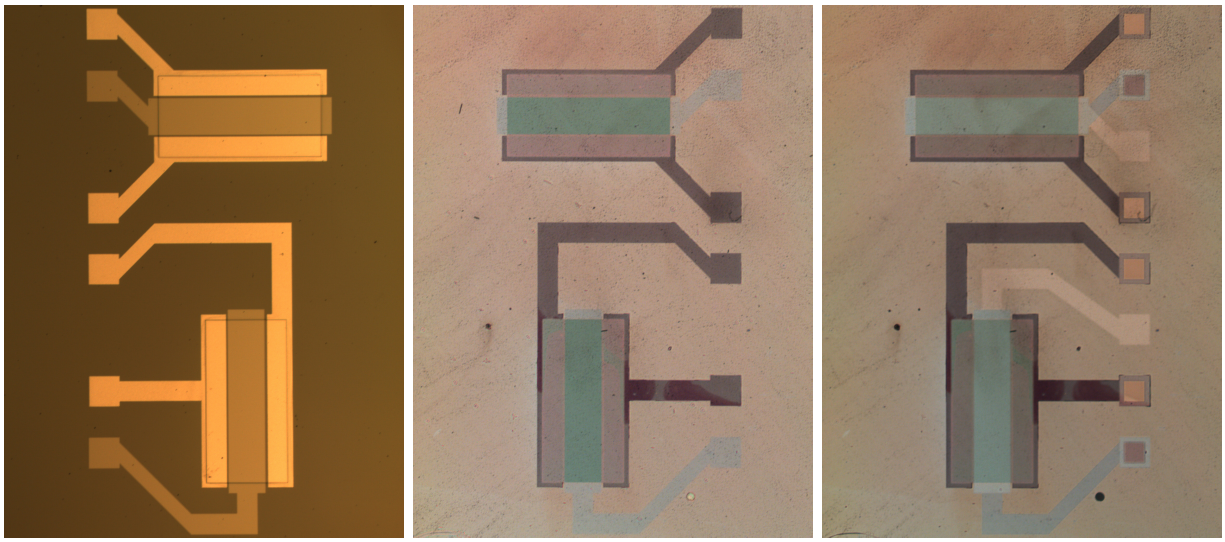

(a) (b) (c)

Figure A.9: Microscope images of the chip (a) after the front gate deposition; (b) after the HF etching; (c) after the full processing.

indicate whether it has hardened. The clamp stage is then baked on a 120 °C hotplate for about 30 min.

Once the epoxy has cured, take the samples off the clamp stage and copy the identifying marks from the back of the GaAs to the sapphire discs. Scribe near the edge of each disc. Now the samples are ready to be lapped.

## A.8 Remove the substrate and smoothing layer

Most of the substrate is first removed by mechanical lapping. The first etch is to remove the remainder of the GaAs substrate by citric acid. The second etch is to remove the AlGaAs etching stop layer by hydrofluoric (HF) acid. The structure after the process is depicted in Figs. A.2 and A.3.

### Lapping

Denise did most of the thinning for us. She used a fancy lapping machine on the air force base that can lap three samples at a time. The thickness of the GaAs substrate is 625 $\mu$m and the total thickness of epitaxial layers is $\sim 1$ $\mu$m. We aim to thin the samples until about 75 $\mu$m of the substrate remains. Then remove the samples from the lapping apparatus and clean them. At this stage, the samples are very fragile and the remaining process should be handled with great care.

### First etch

Under the acid bench, mix 300 g citric acid powder with 300 g water in a big beaker. Stir with a magnetic stir bar at 75 rpm on a stir plate for about an hour until the white powder dissolves. Then mix 420 mL citric acid with 84 mL 30% hydrogen peroxide.

Place the mixed citric acid etchant in a big beaker on a heat/stir place at 65 °C and 75 rpm. Place the chips in a basket with lapped side face-up and hang the basket in the acid. The etching takes about an hour which depends on the thickness of the remaining substrate. The etching slows down at the the AlGaAs etching stop layer. Keep watching the process and take the chips out and soak them into running water when the surface becomes smooth and shiny. In our case, since the sapphire is transparent, the finish is very obvious.

### Second etch

HF acid is highly corrosive. Wear all PPE! HF acid etches glass, and therefore use plastic container instead. Hold the chip with the tweezes and dip it into the HF acid for about 10 sec. The color of the sample is changing rapidly during the etching. When the color stops changing, take the chip out and soak it into the flowing DI water. The device after the HF etching is shown in Fig. A.9b and it is the mirror image of the A.9a.

## A.9 Backside processing

### Vias etching

Vias are etched through the active layers to the buried front side electrical contact pads for the ohmics and front gates as illustrated in Fig. A.3. Perform vias photolithography. Follow the same procedure as the mesa etching. The etching depth should be calculated according to the sample structure and the mesa etching depth. The etching stops at the front metal.

### Metal pads and back gate deposition

Perform metal pads and back gate photolithography. Follow the same procedure as the front gate deposition. The processing is complete shown in Fig. A.9c.

## A.10 Attaching the sample

The sample is then mounted on a Cu holder shown in Fig. A.10a, which can be attached to the cryostat's cold-finger. The sample is place over a hole to allow the measurements in transmission. Between the sapphire disc and the Cu holder, we apply a thin layer of N-grease to increase the thermal contact area. Glue electrical pins to the Cu holder. These pins connect the GaAs device with the external devices. Under a microscope, with great

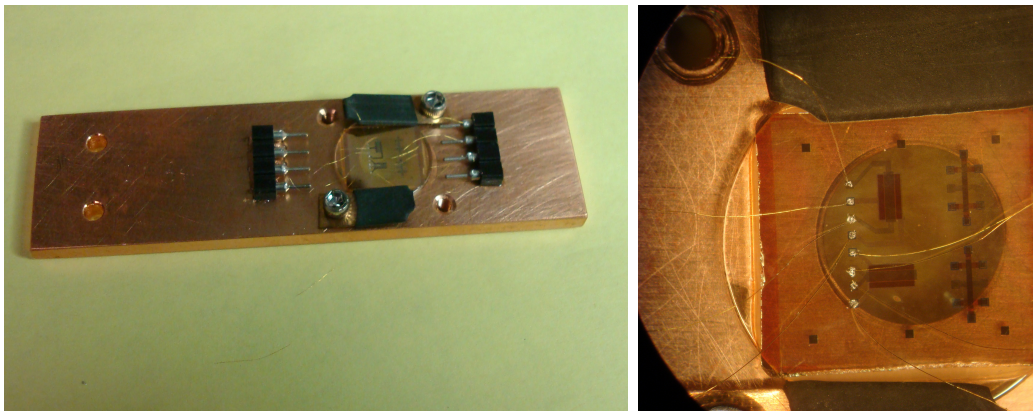

(a) (b)

Figure A.10: Sample mounted on the Cu holder with Au wires connecting the contact pads with the electrical pins.

patience, attach thin Au wires (0.02-0.05 mm diameter) to the contact pads and pins using 50/50 In/Sn solder[6] applied with a soldering iron at 475 °F as shown in Fig. A.10b.

[6]The melting temperature is 425 °F.

# Appendix B

# Transresistance Notes

## B.1 *e-h* transresistivity

The *e-h* transresistivity is derived from the coupled Bolzmann equations within the relaxation time approximation [56]

$$\rho_{eh} = \frac{\hbar^2\beta}{8\pi^2 e^2 n_e n_h}\int_0^\infty dq q^3 |V(q)|^2 \int_0^\infty d\omega \frac{\Im\{\chi_e(\omega,q,T)\}\Im\{\chi_h(\omega,q,T)\}}{\sinh^2(\beta\hbar\omega/2)}, \tag{B.1}$$

where $\beta = 1/k_B T$, $\Im\{\chi(\omega,q,T)\}$ is the imaginary part of the Lindard dielectric function [58]. For simplicity the 2D Thomas-Fermi potential is used in the discussion here,

$$\begin{aligned} V(q) =& \frac{e^2}{2\epsilon_0\epsilon^*(q+q_{TF})} \\ =& \frac{2\pi\hbar^2}{m^* a_B^*(q+q_{TF})}, \end{aligned} \tag{B.2}$$

where $q_{TF} = 2/a_B^*$ is the Thomas-Fermi screening wave vector and $a_B^* = 4\pi\epsilon_0\epsilon^*\hbar^2/m^* e^2$ is the effective Bohr radius.

### Linhard dielectric function

$$\chi(\omega,\boldsymbol{q},T) = \sum_{\boldsymbol{k},\sigma} \frac{f^0(\boldsymbol{k}+\boldsymbol{q}/2) - f^0(\boldsymbol{k}-\boldsymbol{q}/2)}{\hbar\omega - E(\boldsymbol{k}+\boldsymbol{q}/2) + E(\boldsymbol{k}-\boldsymbol{q}/2) + i0^+}, \tag{B.3}$$

where

$$f^0(E) = \frac{1}{1+\exp[\beta(E-\mu)]} \tag{B.4}$$

is the Fermi-Dirac distribution. The chemical potential $\mu$ is determined by

$$n = \int_0^\infty dE D(E) f^0(E) \tag{B.5}$$

for 2DEG

$$\mu = k_B T \ln\left[\exp\left(\frac{T_F}{T}\right) - 1\right]. \tag{B.6}$$

Using the identities

$$\frac{1}{x + i0^+} = P\left(\frac{1}{x}\right) - i\pi\delta(x) \tag{B.7}$$

and

$$\int_a^b g(x)\delta[f(x)] = \sum_i \frac{g(x_i)}{|f'(x_i)|} \tag{B.8}$$

where $x_i \in (a, b)$ are the roots of $f(x) = 0$. Then the imaginary part of Linhard dielectric function is

$$\begin{aligned}
&\Im\{\chi(\omega, \boldsymbol{q}, T)\} \\
=& -\pi \sum_{\boldsymbol{k},\sigma} [f^0(\boldsymbol{k} + \boldsymbol{q}/2) - f^0(\boldsymbol{k} - \boldsymbol{q}/2)]\delta[\hbar\omega - E(\boldsymbol{k} + \boldsymbol{q}/2) + E(\boldsymbol{k} - \boldsymbol{q}/2)] \\
=& -\frac{2\pi}{(2\pi)^2} \int d^2\boldsymbol{k} [f^0(\boldsymbol{k} + \boldsymbol{q}/2) - f^0(\boldsymbol{k} - \boldsymbol{q}/2)]\delta[\hbar\omega - E(\boldsymbol{k} + \boldsymbol{q}/2) + E(\boldsymbol{k} - \boldsymbol{q}/2)] \\
=& -\frac{1}{2\pi} \int d^2\boldsymbol{k} [f^0(\boldsymbol{k} + \boldsymbol{q}/2) - f^0(\boldsymbol{k} - \boldsymbol{q}/2)]\delta\left(\hbar\omega - \frac{\hbar^2 \boldsymbol{k}\cdot\boldsymbol{q}}{m}\right) \\
=& -\frac{1}{2\pi} \int_0^\infty k dk \int_{-\pi}^{\pi} d\theta [f^0(\boldsymbol{k} + \boldsymbol{q}/2) - f^0(\boldsymbol{k} - \boldsymbol{q}/2)]\delta\left(\hbar\omega - \frac{\hbar^2 kq\cos\theta}{m}\right) \\
&\left[\theta_{1,2} = \pm\theta_0, \text{ are the roots of } \delta\left(\hbar\omega - \frac{\hbar^2 kq\cos\theta}{m}\right) \text{ , where } \theta_0 = \arccos\left(\frac{m\omega}{\hbar kq}\right)\right] \\
=& -\frac{m}{\pi\hbar^2 q} \int_0^\infty dk \frac{[f^0(\boldsymbol{k} + \boldsymbol{q}/2) - f^0(\boldsymbol{k} - \boldsymbol{q}/2)]|_{\theta_0}}{\sqrt{1 - \cos^2\theta_0}} \Theta(1 - \frac{m\omega}{\hbar kq}) \\
=& -\frac{m}{\pi\hbar^2 q} \int_0^\infty kdk \frac{[f^0(\boldsymbol{k} + \boldsymbol{q}/2) - f^0(\boldsymbol{k} - \boldsymbol{q}/2)]|_{\theta_0}}{\sqrt{k^2 - (m\omega/\hbar q)^2}} \Theta(1 - \frac{m\omega}{\hbar kq}) \\
=& -\frac{m}{2\pi\hbar^2 q} \int_0^\infty dk^2 \frac{[f^0(\boldsymbol{k} + \boldsymbol{q}/2) - f^0(\boldsymbol{k} - \boldsymbol{q}/2)]|_{\theta_0}}{\sqrt{k^2 - (m\omega/\hbar q)^2}} \Theta(1 - \frac{m\omega}{\hbar kq}) \\
&\left\{\text{define} t = \frac{\beta\hbar^2}{2m}\left[k^2 - \left(\frac{m\omega}{\hbar q}\right)^2\right]\right\} \\
=& -\frac{m}{2\pi\hbar^2}\sqrt{\frac{T}{T_F}}\frac{k_F}{q} \int_0^\infty dt \left\{\frac{t^{-\frac{1}{2}}}{1 + \exp[t + \frac{T_F}{T}(\frac{\omega}{qv_F} + \frac{q}{2k_F})^2 - \frac{\mu}{k_B T}]}\right. \\
&\left. - \frac{t^{-\frac{1}{2}}}{1 + \exp[t + \frac{T_F}{T}(\frac{\omega}{qv_F} - \frac{q}{2k_F})^2 - \frac{\mu}{k_B T}]}\right\} \\
\equiv& \frac{m}{2\pi\hbar^2}\sqrt{\frac{T}{T_F}}\frac{k_F}{q}[\mathfrak{F}_{-\frac{1}{2}}(\eta_-) - \mathfrak{F}_{-\frac{1}{2}}(\eta_+)]
\end{aligned} \tag{B.9}$$

where

$$\eta_{\pm} = \ln\left[\exp\left(\frac{T_F}{T}\right) - 1\right] - \frac{T_F}{T}\nu_{\pm}^2, \tag{B.10}$$

$$\nu_{\pm} = \frac{\omega}{q v_F} \pm \frac{q}{2k_F}, \tag{B.11}$$

and

$$\mathfrak{F}_j(\eta) \equiv \int_0^{\infty} dt \frac{t^j}{1+\exp(t-\eta)} \tag{B.12}$$

is the Fermi-Dirac integral of order $j$ ($j > -1$). $\mathfrak{F}_j(\eta)$ is a well-known function and has the following properties:

$$\mathfrak{F}_j(\eta) \to \begin{cases} \eta^{j+1}/(j+1) & \text{if } \eta \gg 1, \text{ degenerate limit;} \\ \Gamma(j+1)e^{\eta} & \text{if } \eta \ll -1, \text{ nondegenerate limit.} \end{cases} \tag{B.13}$$

$\mathfrak{F}_{-\frac{1}{2}}(\eta)$ can be approximated as

$$\mathfrak{F}_{-\frac{1}{2}}(\eta) \approx \left\{ \frac{1}{\sqrt{2[b+\eta+(|\eta-b|^c + a^c)^{1/c}]}} + \frac{\exp(-\eta)}{\sqrt{\pi}} \right\}^{-1}, \tag{B.14}$$

where $a = 1.69742452, b = 1.495, c = 2\sqrt{2}$ [c.f. J. Appl. Phys. **54**, 5 (1983)].

In the degenerate limit, $\mathfrak{F}_{-\frac{1}{2}}(\eta) = 2\sqrt{\eta}$, then

$$\Im\{\chi(\omega, \boldsymbol{q}, T)\} = \frac{m^2\omega}{\pi\hbar^3 q k_F}. \tag{B.15}$$

In the non-degenerate limit, $\mathfrak{F}_{-\frac{1}{2}}(\eta) = \sqrt{\pi}e^{\eta}$, then

$$\Im\{\chi(\omega, \boldsymbol{q}, T)\} = \frac{m k_F}{\sqrt{\pi}\hbar^2 q}\sqrt{\frac{T_F}{T}} \exp\left(-\frac{\beta\hbar^2 q^2}{8m}\right) \exp\left(-\frac{\beta m\omega^2}{2q^2}\right) \sinh\left(\frac{\beta\hbar\omega}{2}\right) \tag{B.16}$$

## Limits

In the limit, $T \gg T_{Fh}$, where $T_{Fh}$ is the Fermi temperature of the holes,

$$\rho_{eh} = \frac{\hbar}{n_e a_B^{*2} e^2}\sqrt{\frac{m_h}{4\pi m_e}} \int_0^{\infty} dq \frac{q\exp(-q^2 l_T^2/16)}{(q+q_{TF})^2} \int_0^{\infty} d\tilde{\omega} \frac{[\mathfrak{F}_{-\frac{1}{2}}(\eta_-) - \mathfrak{F}_{-\frac{1}{2}}(\eta_+)]\exp(-\tilde{\omega}^2/q^2 l_T^2)}{\sinh(\tilde{\omega}/2)} \tag{B.17}$$

is independent of the hole concentration $n_h$, where $l_T^2 \equiv 2\hbar^2/m_h k_B T$ is the square of the thermal wavelength of the holes and $\tilde{\omega} \equiv \beta\hbar\omega$. This expression was used to evaluate the $e$-$h$ drag resistivity of the sample studied in this work in the low injection limit with the following parameters: $n_e = 2 \times 10^{11}\text{cm}^{-2}$, $m_e = 0.067m_0$ and $m_h = 0.082m_0$. Numerical

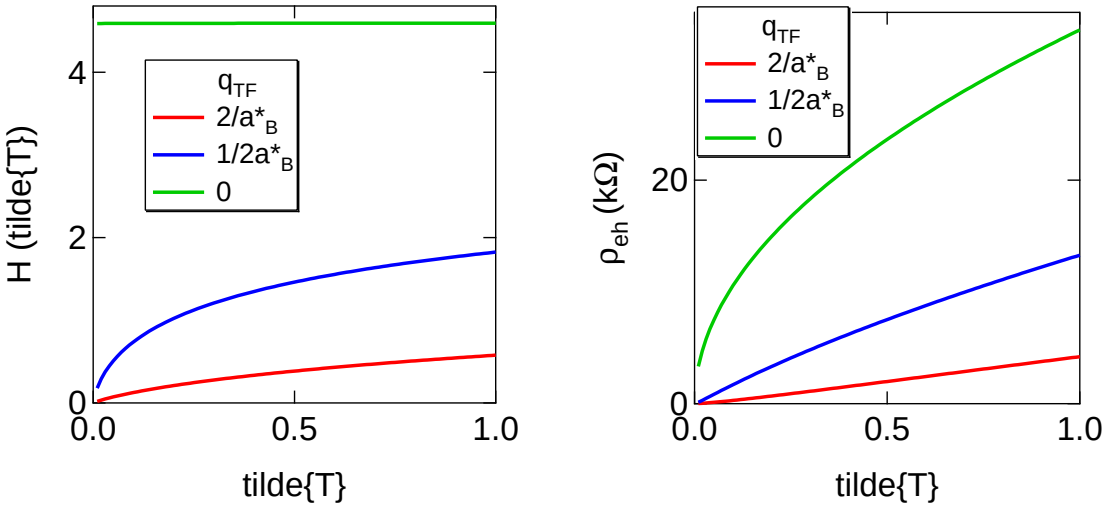


(a) (b)

Figure B.1: (a) Function $H$ and (b) $\rho_{eh}$ for different $q_{TF}$'s.

evaluation of Eq. B.17, plotted as a solid line in Figs. 5.3b and B.3, shows that the RPA interaction describes the experimental data quite well without any free parameters.

In the limit, $T_{Fh} \ll T \ll T_{Fe}$, where $T_{Fe}$ is the Fermi temperature of the electrons,

$$\begin{aligned}
&\rho_{eh} \\
=&\frac{\sqrt{\pi}\hbar}{e^2}\sqrt{\frac{T}{T_{Fe}}}\int_0^\infty d\tilde{q}\frac{\tilde{q}}{(a_B^* k_{Fe}\tilde{q}+a_B^* q_{FT})^2}\exp\left(-\frac{T_{Fe}\tilde{q}^2}{4T}\right)\int_0^\infty d\tilde{\omega}\frac{\tilde{\omega}}{\sinh(\tilde{\omega}/2)}\exp\left(-\frac{m_h T\tilde{\omega}^2}{4m_e T_{Fe}\tilde{q}^2}\right) \\
=&\frac{\sqrt{\pi}\hbar}{e^2}\sqrt{\tilde{T}}\int_0^\infty d\tilde{q}\frac{\tilde{q}}{(a_B^* k_{Fe}\tilde{q}+a_B^* q_{FT})^2}\exp\left(-\frac{\tilde{q}^2}{4\tilde{T}}\right)\int_0^\infty d\tilde{\omega}\frac{\tilde{\omega}}{\sinh(\tilde{\omega}/2)}\exp\left(-\frac{m_h\tilde{T}\tilde{\omega}^2}{4m_e\tilde{q}^2}\right) \\
=&\frac{\sqrt{\pi}\hbar}{e^2}\sqrt{\tilde{T}}\int_0^\infty dq_T\frac{q_T}{(a_B^* k_{Fe}q_T+a_B^* q_{FT}/\sqrt{\tilde{T}})^2}\exp\left(-\frac{q_T^2}{4}\right)\int_0^\infty d\tilde{\omega}\frac{\tilde{\omega}}{\sinh(\tilde{\omega}/2)}\exp\left(-\frac{m_h\tilde{\omega}^2}{4m_e q_T^2}\right) \\
\equiv&\frac{\sqrt{\pi}\hbar}{e^2}\sqrt{\tilde{T}}H(\tilde{T})
\end{aligned} \tag{B.18}$$

where $\tilde{q} \equiv q/k_{Fe}$, $\tilde{\omega} \equiv \beta\hbar\omega$, $\tilde{T} \equiv T/T_{Fe}$, and $q_T \equiv \tilde{q}/\sqrt{\tilde{T}}$. As shown in Fig. B.1, both $H$ and $\rho_{eh}$ depend on the screen wave vector $q_{TF}$. When $q_{TF} = 2/a_B^*$, i.e., the literature value, $\rho_{eh}$ is a little bit super linear; when $q_{TF} = 1/2a_B^*$, $\rho_{eh}$ is a little bit under linear; when there is no screen, $H$ is a constant, and $\rho_{eh} \propto \sqrt{\tilde{T}}$.

If $m_e/m_h \to 0$, then $\rho_{eh} \to 0$, i.e., the holes will not be driven by the electrons. If

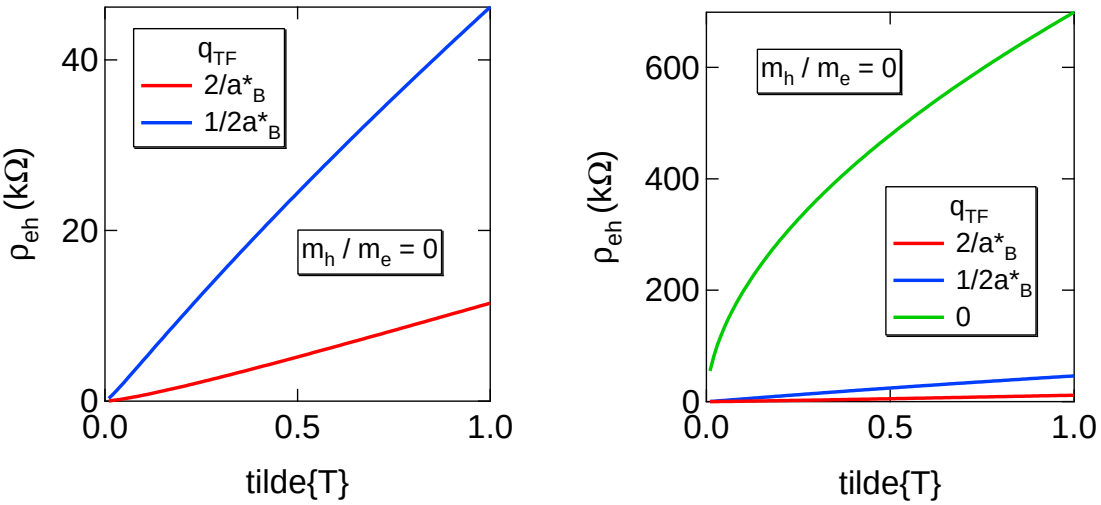


(a) (b)

Figure B.2: $\rho_{eh}$ for different $q_{TF}$'s with $m_h/m_e \to 0$.

$m_h/m_e \to 0$, then

$$\int_0^\infty d\tilde{\omega} \frac{\tilde{\omega}}{\sinh(\tilde{\omega}/2)} \exp\left(-\frac{m_h \tilde{\omega}^2}{4 m_e q_T^2}\right) = \int_0^\infty d\tilde{\omega} \frac{\tilde{\omega}}{\sinh(\tilde{\omega}/2)} = \pi^2, \tag{B.19}$$

and

$$\rho_{eh} = \frac{\pi^2 \sqrt{\pi}\hbar}{e^2} \sqrt{\tilde{T}} \int_0^\infty dq_T \frac{q_T}{(a_B^* k_{Fe} q_T + a_B^* q_{FT}/\sqrt{\tilde{T}})^2} \exp\left(-\frac{q_T^2}{4}\right). \tag{B.20}$$

In Fig. B.3, we plot $\rho_{eh}$ as a function of temperature with the same electron density but $m_h/m_e \to 0$. The feature looks similar as before, but the magnitude depends strongly on the screen wave vector and is larger than before.

## B.2 Spin transresistivity

We extract the spin drag transresistivity, $\rho_{\uparrow\downarrow}$, from the relationship derived by D'Amico and Vignale [63],

$$\frac{D_s}{D_e} = \frac{1}{1 + \rho_{\uparrow\downarrow}/\rho}, \tag{B.21}$$

where $\rho = (n_0 e \mu_e)^{-1}$ is the resistivity, $D_s$ is the spin diffusion coefficient, and $D_e$ is the electron diffusion coefficient. The latter is related to electron mobility, $\mu_e$, by the Einstein

relation in two dimensions,

$$\frac{D_e}{\mu_e} = \frac{E_F}{e[1-\exp(-E_F/k_BT)]} \tag{B.22}$$

From Eqs. B.21 and B.22, we see that independent measurement of $D_s$, $\mu_e$ and $\rho$ yields the spin drag transresistivity $\rho_{\uparrow\downarrow}$ [64, 65].

To compare the measured $\rho_{\uparrow\downarrow}$ with the random phase approximation prediction, we consider the low-temperature static limit of the RPA formula for the spin drag resistivity [64, 65],

$$\rho_{\uparrow\downarrow} = \frac{\hbar^2\beta}{8\pi^2e^2n_\uparrow n_\downarrow}\int_0^\infty dqq^3|V(q)|^2\int_0^\infty d\omega\frac{\Im\{\chi_\uparrow(\omega,q,T)\}\Im\{\chi_\downarrow(\omega,q,T)\}}{\sinh^2(\tilde{\omega}/2)}, \tag{B.23}$$

where $n_\uparrow$ and $n_\downarrow$ are the concentration of spin up and down electrons, respectively. In the case $n_\uparrow = n_\downarrow$,

$$\begin{aligned}
&\Im\{\chi_\uparrow(\omega,\boldsymbol{q},T)\} = \Im\{\chi_\downarrow(\omega,\boldsymbol{q},T)\}\\
=&-\pi\sum_{\boldsymbol{k}}[f^0(\boldsymbol{k}+\boldsymbol{q}/2)-f^0(\boldsymbol{k}-\boldsymbol{q}/2)]\delta[\hbar\omega-E(\boldsymbol{k}+\boldsymbol{q}/2)+E(\boldsymbol{k}-\boldsymbol{q}/2)]\\
=&\frac{m}{2\pi\hbar^2}\sqrt{\frac{T}{T_F}}\frac{k_F}{q}[\mathfrak{F}_{-\frac{1}{2}}(\eta_-)-\mathfrak{F}_{-\frac{1}{2}}(\eta_+)].
\end{aligned} \tag{B.24}$$

In the degenerate limit, for small $\omega$ and $q$, the imaginary part of Lindhard susceptibility can be written,

$$\Im\{\chi_\uparrow(\omega,\boldsymbol{q},T)\} = \Im\{\chi_\downarrow(\omega,\boldsymbol{q},T)\} = \frac{m^2\omega}{2\pi\hbar^3qk_F}, \tag{B.25}$$

and the static Coulomb interaction is given by Eq. B.2. Substituting Eqs. B.2 and B.25 into Eq. B.24, we obtain,

$$\rho_{\uparrow\downarrow} = \frac{2\pi^2\hbar}{3e^2}\left(\frac{T}{T_F}\right)^2\frac{(1+\eta)\ln(1+\eta)-\eta}{\eta^2(1+\eta)}, \tag{B.26}$$

where $\eta \equiv 2k_F/q_{TF}$. The values of $\rho_{\uparrow\downarrow}(T)$ thus obtained, and shown in the inset of Fig. 6.1c and Fig. B.3, are in excellent agreement with the experimental data below the Fermi temperature of 80 K.

Figure B.3 shows the comparison of $\rho_{eh}$ and $\rho_{\uparrow\downarrow}$. $\rho_{\uparrow\downarrow}$ has $T^2$ dependence at low $T$, because there are two degenerate species.

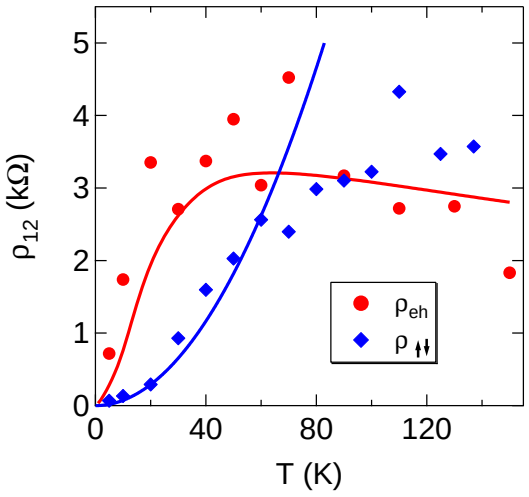


Figure B.3: The comparison of $\rho_{eh}$ and $\rho_{\uparrow\downarrow}$. The solid lines are the theoretical predictions using Eqs. B.17 and B.26, respectively.